TIME-RESOLVED ULTRAFAST PHOTOREACTION DYNAMICS OF SMALL MOLECULES IN THE VACUUM ULTRAVIOLET SPECTRAL RANGE

Dissertation

zur Erlangung des Doktorgrades
and der Fakultät für Mathematik, Informatik
und Naturwissenschaften
Fachbereich Physik
der Universität Hamburg

vorgelegt von

Arne Baumann

Hamburg

2018

Gutachter/in der Dissertation: Prof. Dr. Markus Drescher
JProf. Dr. Ulrike Frühling

Zusammensetzung der Prüfungskommision: Prof. Dr. Markus Drescher
JProf. Dr. Ulrike Frühling
Prof. Dr. Robin Santra
Prof. Dr. Michael Meyer
Priv. Doz. Dr. Tim Laarmann

Vorsitzende/r der Prüfungskommision: Prof. Dr. Robin Santra

Datum der Disputation: 06.08.2018

Vorsitzender des Fach-Promotionsausschusses Physik: Prof. Dr. Wolfgang Hansen

Leiter des Fachbereichs Physik: Prof. Dr. Michael Potthoff

Dekan der Fakultät für Mathematik, Informatik und Naturwissenschaften: Prof. Dr. Heinrich Graener

ABSTRACT

Photoreaction dynamics of small molecules have been studied with a single-shot pump-probe approach utilizing different combinations of few-femtosecond (vacuum) ultraviolet (VUV) pulses under perturbative conditions.

The single-shot scheme is based on wave-front splitting of intense Ti:Sa harmonic pulses centered at 161 nm and 268 nm in a colliding pulse geometry, mapping the temporal delay onto a spatial coordinate. This dramatically decreases acquisition time compared to traditional delay-scanning approaches, increasing the statistical precision of the measurement and allows to discern sub-10-fs dynamics by combining robust in-situ single-shot pulse metrology and pump-probe measurements.

Temporal characterization of the (V)UV pulses was performed by multiphoton ionization of Kr and Xe under perturbative, as well as strong field conditions. Superposition of a strong UV and a weak IR field allowed delay- and intensity-dependent imaging of multiple transient ionization pathways in the resonant ionization of Kr and reconstruction of the temporal profile of the UV pulse under strong-field conditions.

The VUV-induced dynamics of H_2O and its deuterated isotopologues in the first excited state ($\tilde{A}^1B_1$) was studied utilizing a VUV-pump VUV-probe scheme combined with ab-initio classical trajectory calculations. By combining a weak-field approach with precise determination of the instrument response function, dynamics in the 1+1 photon ionization window as fast as (6.7±1.8) fs were disclosed, without perturbing the system under study in contrast to multiphoton IR-probe schemes.

The all-reflective wave-front splitting design is applicable from the visible to the extreme ultraviolet spectral range and the spectrum of pump- and probe-pulse can be selected individually. The dissociation dynamics of iodomethane after Rydberg excitation at 161 nm and valence excitation at 268 nm was studied in a UV-pump VUV-probe experiment. Sub-30 fs wave packet dynamics upon excitation in the A-band by a UV pump pulse were disclosed, while following the population transfer from the 6p ($^2E_{3/2}$) Rydberg state to the 2 $^1A_1$ valence state leading to 100-fs dissociation dynamics after VUV excitation at the same time.

KURZFASSUNG

Die Photoreaktiondynamik von kleinen Molekülen wurde in einem Einzelschuss-Anregungs-Abfrage-Experiment untersucht. Dazu wurden verschiedene Kombinationen von (vakuum-)ultravioletten (VUV)-Pulsen mit einer Pulsdauer von wenigen Femtosekunden unter pertubativen Bedingungen eingesetzt.

Der Einzelschussansatz basiert auf der Wellenfrontteilung von intensiven Ti:Sa-Harmonischenpulsen mit einer Zentralwellenlänge von 161 nm und 268 nm in einer anti-parallelen Geometrie, wodurch die zeitliche Verzögerung auf eine räumliche Koordinate abgebildet wird. Im Vergleich zu traditionellen Aufbauten, in denen die Verzögerung schrittweise variiert werden muss, wird die Messzeit drastisch reduziert und die statistische Signifikanz der Messung erhöht. Somit können sub-10-Femtosekundendynamiken durch die Kombination von robuster In-situ-Einzelschuss-Pulsmetrologie und Anregungs-Abfrage-Spektroskopie aufgedeckt werden.

Die (V)UV-Pulse wurden durch Multiphotonenionisation von Kr und Xe sowohl unter perturbativen, als auch unter Stark-Feld-Bedingungen zeitlich charakterisiert. Die Überlagerung von starkem UV-Feld mit einem schwachen IR-Feld ermöglicht die verzögerungs- und intensitätsabhängige Abbildung einer Vielzahl von transienten Ionisationspfaden in der resonanten Ionisation von Kr, aus der das zeitliche Profil der UV-Pulse unter Stark-Feld-Bedingungen rekonstruiert wurde.

Die VUV-induzierte Dynamik von H_2O und seinen deuterierten Isotopologen im ersten angeregten Zustand $(\tilde{A}^1B_1)$ wurde in einem VUV-Anregungs-VUV-Abfrage-Experiment untersucht. Die Experimente wurden durch ab-initio klassische Trajektoriekalkulationen unterstützt. Durch die Kombination des pertubativen Ansatzes mit präziser Bestimmung der Instrumentenfunktion, wurden Dynamiken im 1+1-Photonen-Ionisationsfenster mit einer Dauer von bis zu $(6,7 \pm 1,8)$ fs aufgedeckt ohne das System in Kontrast zu Multiphotonen-Infrarot-Ansätzen stark zu stören.

Das vollreflektive Wellenfrontteilungsdesign ist vom sichtbaren bis in den extremultravioletten Spektralbereich einsetzbar und das Spektrum des Anregungs- und Abfragepulses kann unabhängig selektiert werden. Die Dissoziationsdynamik von Iodmethan nach Rydberganregung bei 161 nm und Valenzanregung bei 268 nm wurde in einem UV-Anregungs-VUV-Abfrage-Experiment untersucht. Wellenpaketdynamiken unter 30 Femtosekunden nach der Anregung in das A-Band durch einen UV-Puls wurden aufgeklärt, während zeitgleich der Populationstranfer aus dem 6p $(^2E_{3/2})$ Rydbergzustand zum $2\,^1A_1$ Valenzzustand, der nach VUV-Anregung zu einer 100-fs Dissoziationsdynamik führt, beobachtet wurde.

TABLE OF CONTENTS

1

INTRODUCTION

Imaging chemical reactions at their natural time scale and visualizing the inter- and intramolecular processes leading to the breaking of chemical bonds and the subsequent formation of new chemical compounds has long been the vision of molecular physicists and physical chemists [1]. With the advent of Femtochemistry pioneered by Zewail [2] in 1987 this vision has been fulfilled by utilizing ultrashort laser pulses with durations comparable to the intrinsic reaction dynamics to take snapshots of the evolving chemical reactions.

Typically these experiments involve photoexcitation of the system by one femtosecond light pulse (termed the pump pulse), and the interrogation of this process by a second ultrashort light pulse (the probe pulse) after a well-defined and variable time delay [3, 4]. By these means, a series of snapshots is retrieved, where one or more observables are tracked as a function of the delay between pump and probe pulse. For example changes to the probe pulse's spectrum (transient absorption spectroscopy) [5] are observed, or the delay-dependent ionization and photoelectron yield of photoreaction educts and products [6–9].

These reaction dynamics are often taking place on the potential energy surface of an excited electronic state and new reaction pathways may be explored by the molecule on the potential energy landscape compared to traditional ground state reaction dynamics. The possibilities offered by the complex interplay between intersecting potential energy surfaces, so called conical intersections, lead to the emergence of reaction coordinates, which efficiently guide the reaction pathways towards desired products or effectively disperse the deposited energy after photoexcitation by transferring the system back into its electronic ground state [10–12]. One important example for this is the ultrafast isomerization in the primary step in human vision [13] or the photo-resistivity of deoxyribonucleic acid.

In the field of Femtochemistry a rich tool set of detection techniques, such as laser-induced fluorescence detection [14–16], ion spectrometry [6], photoelectron spectroscopy [7, 8] and finally velocity map imaging [9], has been developed [1]. While laser-induced fluorescence is fundamentally different from the other techniques, it is derived consequently from the chemists' mindset, as it is also true for transient absorption spectroscopy [5]. Both techniques give insight into delay-dependent properties of the absorption and fluorescence spectrum of a molecule, which are directly linked to elucidating chemical dynamics, which is the heart of Femtochemistry.

The ongoing development of these techniques focused on retrieving more and more information from a single experiment. Where time-resolved ion spectrometry yields information about when certain species are created in a dynamical system, photoelectron spectroscopy adds information about the molecular states involved in the dynamics and velocity map imaging finally augments the latter with momentum-information. Of course these techniques can also be combined in coincidence experiments [17, 18], merging independent experiments and creating links between photoelectron spectrum and delay-dependent ion yields, further aiding the description of the molecular dynamics.

But not only detection techniques are of interest. The most advanced detection scheme can only access molecular dynamics, as long as it is combined with light pulses providing the necessary temporal resolution and spectrum to initiate and probe these dynamics. Transferring the pump-probe methodology into the vacuum ultraviolet (VUV) and XUV (extreme ultraviolet) spectral range enables linear transitions to highly excited states in the pump step giving access to different potential energy surfaces. Due to the higher energy transferred to the system new reaction pathways may open up, which lead to desired products, and are thermodynamically inaccessible from lower lying electronic states. A prerequisite to drive and interrogate such dynamics is the availability of sub-20-fs pulses with tunable intensity to effectively drive single or multiphoton transition in the pump step while limiting their field-strength at the same time. Only by these means, the system is not dressed and perturbed by strong-fields and the intrinsic dynamics of the system is accessible [19–21].

Combining VUV pulses fulfilling these requirements with femtosecond spectroscopy techniques to study reaction dynamics of small molecules is the main topic of this work. VUV pulses with a central wavelength of 268 nm and 161 nm are generated in the perturbative regime of low-order gas phase harmonic generation by loosely focusing an intense few-femtosecond infrared pulse from a Ti:Sa laser system into an Argon gas medium [22–25]. The generation conditions of the individual harmonics can be precisely tuned to reach pulse durations below 20 fs, while achieving pulse energies of up to 1.1 µJ in the VUV.

These pulses are then delivered to a single-shot pump-probe experiment, where the pump and probe pulses are spatially separated and then overlapped in an anti-parallel manner in the gas target of a pulsed valve. Since both pulses propagate in opposite directions and meet in a common focal plane, the delay between both pulses is mapped onto a spatial coordinate. Molecular dissociation dynamics initiated by the pump pulse can be studied by retrieving the spatial distribution of parent and fragment ions created by ionizing the transient reaction educt and products with the probe pulse with a species-selective imaging time-of-flight ion spectrometer (ion microscope) [26, 27]. By these means, a full data set in a delay range of ±500 fs can be retrieved with every single shot [28].

This methodology eliminates the need for time-consuming variation of the delay between pump and probe pulse with a delay stage typically used in femtosecond pump probe experiments, leading to significantly improved statistical accuracy with shorter acquisition times. Combined with in-situ pulse characterization by non-linear auto and cross correlation methods in the same apparatus reaction dynamics as fast as 5 femtoseconds can be robustly extracted from the transient ion yield. Furthermore, multi-dimensional studies, such as isotope-substitution, studying the effects of chemical modification on similar compounds, become feasible and may be carried out in few hours. Since the ion microscope records a lateral image of the common focus of both beams not only delay-dependent data is retrieved with each single shot, but also a complete intensity-scan over the transversal focus coordinate is included in every single shot image. This possibility is utilized in the presented work to enable temporal characterization of the 268-nm pulses under non-pertubative conditions, where a high field strength leads to the appearance of highly-charged noble gas ions and shifting of atomic potentials by thr AC stark effect.

Furthermore, the design of the apparatus allows to spectrally isolate individual harmonics of the harmonic pulse train and a variety of pump-probe experiments with different combinations of light fields may be realized. The capabilities of this methodology are demonstrated in several time-resolved experiments focusing on ultrafast dissociation dynamics of atmospherically relevant molecules, such as water and its deuterated isotopologues and iodomethane. Here, the early-stage reaction dynamics become accessible to the technique by utilizing weak-field VUV pulses to ionize the molecule and avoiding strong multiphoton infrared probe fields. In iodomethane a two-color scheme combining 268-nm and 161-nm pulses is used to initiate dissociation dynamics starting from low-lying valence and high-lying Rydberg states at the same time; in both cases the reaction dynamics are governed by conical intersections between the participating potential energy surfaces.

In Chapter 2 important principles will be introduced to provide the theoretical background of this thesis: First, a theoretical description of ultrashort pulses and their propagation will be laid out, before introducing auto and cross correlation methods for the temporal characterization of these pulses. The interaction between these pulses with atoms and molecules is important for initiating and probing reaction dynamics, as well as the conversion of infrared pulses into VUV and XUV pulses used in this work. The chapter is closing with an introduction on excited state molecular dynamics in the wave packet picture.

Chapter 3 will focus on the experimental realization of the harmonic generation and its diagnostics. Furthermore, the colliding-pulse single-shot pump-probe technique is explored in detail and applied to the temporal characterization of VUV pulses.

The conducted pump-probe experiments are discussed in detail in Chapter 4. First, the ultrafast dissociation dynamics of H_2O and its deuterated isotopologues after excitation at 161 nm are addressed. Before focusing on the competition between dissociation initiated by Rydberg and valence excitation in iodomethane with a combination of 268-nm and 161-nm pulses, the 268-nm pulses are characterized in the time-domain. For this measurement the intensity of the pulses has been tuned to operate not only in the weak-field regime, but also at high field strength, where the effects of the high intensity on the temporal characterization measurement are analyzed.

Finally, the presented results will be summarized and put into context, before possible future applications of the low-order harmonic source and single-shot apparatus will be discussed in Chapter 5.

2

THEORETICAL BACKGROUND

Studying photoinduced molecular reaction dynamics in the time-domain is only possible by utilizing methodology, which may access these dynamics on their natural femtosecond time scale. Ultrashort light pulses enable both the temporal measurement and the generation of radiation at wavelengths resonant to molecular and atomic transitions in the vacuum ultraviolet spectral range. In the following chapter, the fundamental principles describing ultrashort light pulses will be laid out.

Ultrashort vacuum ultraviolet pulses are generated by the interaction between an intense infrared laser pulse and an atomic medium in the gas phase. The nature of this interaction is determined by the intensity of the pulse and may range from perturbative photoexcitation and -ionization at low intensities to strong-field effects, such as tunneling ionization and high-order harmonic generation. The perturbative interactions are furthermore essential in the preparation of molecular states, which facilitate excited state reaction dynamics, and in the interrogation of these dynamics.

This chapter closes with an overview of processes, which follow the preparation of an excited state wave packet. These processes may lead to formation of reaction products or relaxation to the electronic ground state of the molecule.

2.1 ULTRASHORT LIGHT PULSES

An ultrashort light pulse is completely defined by its time-dependent electric field $\mathcal{E}(t)$. For the derivation of the pulse properties the spatial coordinates will be neglected in the beginning and the discussion follows References [29–31]. The electric field as a function of time is not easily experimentally accessible for femtosecond pulses and the frequency-dependent representation of the field is often more practical. From the real function $\mathcal{E}(t)$, representing the physical properties of the electric field, the spectral representation is given by its Fourier transform

$$\tilde{E}(\omega) = A(\omega)e^{i\varphi(\omega)}. \tag{2.1}$$

Here the superscript $\sim$ is used to denote complex quantities. $\tilde{E}(\omega)$ is the complex electric field in respect to the angular frequency ω, $A(\omega)$ is the real-valued spectral amplitude, while $\varphi(\omega)$ is the spectral phase of the pulse. An inverse Fourier transform of this function yields the complex time-domain representation of the electric field

$$\tilde{E}(t) = \frac{1}{2\pi} \int_{-\infty}^{\infty} \tilde{E}(\omega) e^{-i\omega t} d\omega. \tag{2.2}$$

For convenience the carrier frequency ω_0, corresponding to the central angular frequency of the pulse, is introduced in the resulting function:

$$\tilde{E}(t) = A(t) e^{i\phi(t)} e^{-i\omega_0 t}. \tag{2.3}$$

Similar to the representation in the spectral-domain the complex electric field $\tilde{E}(t)$ is described by a real-valued temporal amplitude $A(t)$ and a term for the temporal phase $\phi(t)$ distinct from the spectral phase $\varphi(\omega)$. When temporal amplitude and phase are known, the pulse shape and duration is fully described. The same is true for the spectral amplitude and phase terms, due to the Fourier transform relationship.

The phase terms are often represented as a Taylor expansion around the central angular frequency ω_0 for $\varphi(\omega)$ and the reference time t_0 for $\phi(t)$. For the spectral phase the resulting equation is:

$$\begin{aligned} \varphi(\omega) = \varphi_0 + \varphi_1(\omega - \omega_0) + \frac{1}{2}\varphi_2(\omega - \omega_0)^2 \\ + \frac{1}{6}\varphi_3(\omega - \omega_0)^3 + \ldots + \frac{1}{n!}\varphi_n(\omega - \omega_0)^n, \end{aligned} \tag{2.4}$$

with $\varphi_n = \partial^n \varphi(\omega_0)/\partial\omega^n$.

φ_0 refers to the carrier envelope phase, which corresponds to the phase between the envelope of the electric field and its carrier. For few-cycle pulses this term is important in the description of non-linear interactions, because the observed electric field and the resulting intensity may change strongly with the carrier envelope phase.

φ_1 is the group delay T_g, describing the arrival time of the pulse in respect to the reference time t_0.

φ_2 is termed group delay dispersion (GDD) or linear chirp and denotes the arrival time of each spectral component, which increases linearly with the frequency. This means the instantaneous frequency observed, when scanning through the pulse, is increasing linearly.

φ_3 is the third-order dispersion (TOD). The TOD leads to the formation of a series of post or pre-pulses in the time domain.

A similar description may be given for the temporal representation of the phase:

$$\begin{aligned} \phi(t) = \phi_0 + \phi_1(t - t_0) + \frac{1}{2}\phi_2(t - t_0)^2 \\ + \frac{1}{6}\phi_3(t - t_0)^3 + \ldots + \frac{1}{n!}\phi_n(t - t_0)^n, \end{aligned} \tag{2.5}$$

with $\phi_n = \partial^n \phi(t_0)/\partial t^n$. The respective quantities ϕ_n are directly linked to their counter-parts in the spectral representation. ϕ_1 is the phase between carrier and envelope, ϕ_1 is linked to the instantaneous frequency, and so on.

When the non-linear phase terms are zero, the phase is considered flat and the pulse is said to be Fourier limited, which means that the shortest pulse duration for a given spectral amplitude $A(\omega)$ is observed. As a Fourier pair, the minimal pulse duration for a given shape of the spectral amplitude has the following relation to the spectral bandwidth $\Delta\omega_\mathrm{P}$:

$$\frac{\Delta\omega_\mathrm{P}}{2\pi}\tau_\mathrm{P} = \Delta\nu_\mathrm{P}\tau_\mathrm{P} \geq \mathrm{TBP}. \tag{2.6}$$

.

TBP is the time-bandwidth product, which depends on the actual shape of the envelope of the pulse and $\Delta\nu_\mathrm{P}$ the frequency bandwidth of the pulse. Throughout this thesis Gaussian temporal pulse shapes will be used to describe the temporal envelope of the pulse:

$$A(t) = \mathcal{E}_0 \exp\left(\frac{-(t-t_0)^2}{2\sigma_\mathrm{P}^2}\right), \tag{2.7}$$

Where $\mathcal{E}_0$ is the peak electric field of the pulse and σ_P is the root-mean-square pulse duration, which is linked to the full width at half maximum (FWHM) pulse duration τ_P by

$$\tau_\mathrm{P} = 2\sqrt{2\ln 2}\,\sigma_\mathrm{P}.$$

The time-bandwidth product for a Gaussian pulse is 0.441. This and values for other widely used pulse shapes are tabulated in various text books, e. g. Ref. [29].

For now this section focused on the derivation of the temporal properties of ultrashort pulses. In an experiment these pulses are typically used in focused beams, resulting in a temporal and spatial intensity dependence. The spatial dependence is well described in the paraxial approximation, meaning that the transverse beam dimension changes slowly compared to typical travel distances along the direction of the beam [29]. If this is the case, the intensity of a Gaussian beam propagating in z direction may be described as a function of z and the radius r:

$$I(r,z) = I_0 \left(\frac{w_0}{w(z)}\right)^2 \exp\left(\frac{-2r^2}{w(z)}\right), \tag{2.8}$$

where I_0 is the peak intensity, w_0 the beam waist in the focal plane (measured as the radius at $1/e^2$ maximum), and $w(z)$ is the waist in respect to the propagation direction. For the ease of description, these quantities may be expressed in terms of the Rayleigh range z_R, the central wavelength of the pulse λ and the peak power P_0:

$$w(z) = w_0\sqrt{1+\frac{z}{z_R^2}}, \qquad z_R = \pi\frac{w_0^2}{\lambda}, \qquad I_0 = \frac{2P_0}{\pi w_0^2}. \tag{2.9}$$

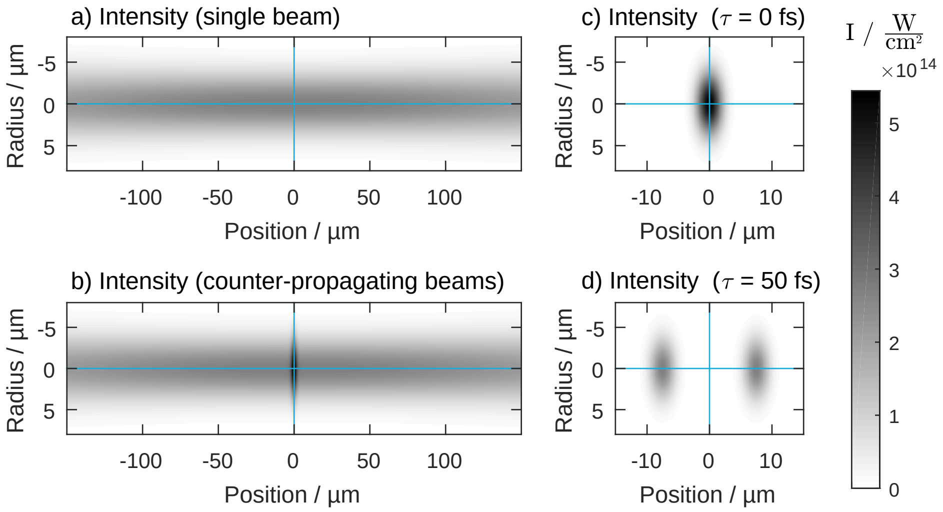

FIGURE 2.1– Spatio-temporal intensity distribution calculated by Gaussian beam propagation of isolated and counter-propagating ultrashort pulses. (a) Time-integrated spatial intensity distribution of an isolated pulse. (b) Time-integrated spatial intensity distribution of two counter-propagating pulses. (c-d) Spatial intensity distributions of two counter-propagating pulses for the delays τ of 0 fs and 50 s, respectively.

The Rayleigh range defines the distance z, where the beam radius is increased by a factor of $\sqrt{2}$ and $2z_R$ is called the confocal parameter and defines the depth-of-focus. In this description the the beam quality M^2 is omitted, as well as the influence of a medium. Light pulses created by optimized laser systems generally exhibit a beam quality close to $M^2 = 1$ and the the beam is propagating through vacuum most of the time.

Equation 2.8 can be combined with Equation 2.7, describing the temporal intensity of a Gaussian pulse. This results in an equation for the spatio-temporal intensity:

$$I(r,z,t) = I_0 \left(\frac{w_0}{w(z)}\right)^2 \exp\left(\frac{-2r^2}{w(z)}\right) \exp\left(\frac{-(t-t_0)^2}{2\sigma_t^2}\right). \tag{2.10}$$

In the presented work a single-shot pump-probe experiment has been utilized relying on a geometry, where two Gaussian beams are focused in a counter-propagating manner. The peak intensity in the focus of this optical system can be simulated by utilizing Equation 2.8 and may be derived from the energy of the pulse E_P and the pulse duration σ_P:

$$I_0 = \frac{E_\mathrm{P}}{\tau_\mathrm{P}}. \tag{2.11}$$

Figure 2.1 a shows the results of this calculation for a beam with a waist w_0 of 5 µm created by propagating a single pulse with an energy of 2.5 µJ, a FWHM pulse duration of 22 fs and a central wavelength of 268 nm. The intensity scale in W cm^{-2} is the same in all subfigures, as indicated by the colorbar.

Figure 2.1 a exhibits the typical spatial intensity distribution of a Gaussian beam. Under these conditions the Rayleigh range is 293 µm and the waist is changing slowly in relation to the propagation coordinate z.

For an accurate description of the experiment the counter-propagation of both beams must be considered. The spatio-temporal peak intensity for two identical pulses is shown in Figure 2.1 b, where both pulses are overlapped in space and time in the focal plane. In this simulation, an intense feature near the focal plane, with a Gaussian shape in both dimensions is observed. The radial component is due to the radial term of the Gaussian beam propagation, while the z dependence is created by the superposition of the intensity envelopes of the individual pulses.

The origin of this observation becomes obvious, when the spatial intensity distribution is visualized for a fixed time. It is convenient to denote these times not in an absolute time scale, but in a delay time scale, where the delay τ is the relative arrival time difference between both pulses for a position along the propagation dimension z. The spatial intensity distribution, when both pulses are superimposed in time ($\tau = 0$ fs) is visualized in Figure 2.1 c and a maximum intensity of ca. 5×10^{14} W cm^{-2} is reached, identical to the doubled peak intensity of an individual pulse.

Due to the symmetry of the counter-propagation there are two positions, where the individual pulses arrive with a delay of ± 50 fs. The spatial intensity dependence at the time these positions are reached is shown in Figure 2.1 d. Both pulses are separated in space and time and the observed intensity maximum is the peak intensity of a single pulse.

2.1.1 PULSE CHARACTERIZATION

The pulse duration of the ultrashort light pulses enabling the pump-probe experiments conducted in this work are on the order of few tens of femtoseconds. Electronic detectors, such as fast photodiodes or streak cameras, do not allow a direct measurement of temporal properties of these pulses in the time-domain, because their response time is on the order of many hundreds femtoseconds or picoseconds to nanoseconds [32, 33]. The signals acquired by these slow detectors are consequently time-integrated in respect to the time scale of the pulse. While spectrometers are able to measure the spectral intensity envelope of the pulse, only the Fourier-limited pulse duration can be deduced with Equation 2.6 and without knowledge of the spectral phase the pulse shape in the time-domain is not accessible.

These limitation can be overcome by measuring the non-linear response, for example second-harmonic generation in non-linear crystals, as a function of the delay between two pulses, which is determined by the second-order non-linear susceptibility $\chi^{(2)}$. When measuring the intensity of the second harmonic in respect to the delay the correlation function of these pulses is retrieved, which gives an estimation of the pulse duration. There are two distinct cases: the auto correlation, where the test pulse is measured in respect to a replica of itself, and the cross correlation, where the test pulse is measured in respect to a known reference pulse.

When the second-order non-linear response of a medium in respect to the delay between two identical collinear pulses is retrieved by a slow intensity detector, the signal is given by

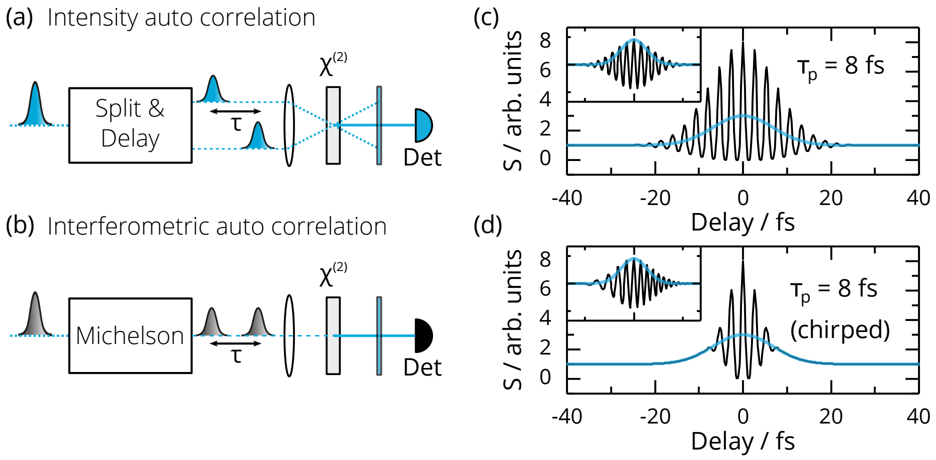

FIGURE 2.2– Schemes for (a) intensity auto correlation and (b) interferometric auto correlation of ultrashort pulses. (c) Auto correlation signal of a Fourier-transform limited pulse as measured by both techniques . (d) Auto correlation signal of a linearly chirped pulse as measured by both techniques. The electric field and temporal amplitude are depicted in the respective insets.

$$S(\tau) = \int_{-\infty}^{+\infty} \left| \left[\tilde{E}(t) + \tilde{E}(t-\tau) \right]^2 \right|^2 dt \tag{2.12}$$

$$= \int_{-\infty}^{+\infty} I^2(t) + I^2(t-\tau) dt \tag{2.12a}$$

$$+ 4 \int_{-\infty}^{+\infty} I(t) I(t-\tau) dt \tag{2.12b}$$

$$+ 2 \int_{-\infty}^{+\infty} \left[I(t) + I(t-\tau) \right] \tilde{E}(t) \tilde{E}^*(t-\tau) dt + c.c. \tag{2.12c}$$

$$+ 2 \int_{-\infty}^{+\infty} \tilde{E}^2(t) \tilde{E}^{*2}(t-\tau) dt + c.c. \tag{2.12d}$$

The Term 2.12a is due to the non-linear signal created by each individual pulse, Term 2.12b is the intensity auto correlation signal. The Terms 2.12c and 2.12d are oscillating with the frequencies ω and ω^2 and the sum of all terms constitutes the fringe-resolved auto correlation signal (FRIAC).

The intensity auto correlation signal is mathematical identical to the convolution of the temporal intensity envelope of both pulses (here test and reference pulse are identical):

$$S(\tau) = A^{(\mathrm{Ref})}(t) \otimes A^{(\mathrm{Test})}(t) = \int_{-\infty}^{+\infty} A^{(\mathrm{Ref})}(t) A^{(\mathrm{Test})}(t-\tau) d\tau \tag{2.13}$$

Depending on the experimental realization either the intensity auto correlation or the FRIAC signal is retrieved. Figure 2.2 shows the schemes for intensity auto correlation (a) and the interferometric auto correlation (b). In both cases the test pulse is split into to identical replicas, and one copy is delayed in respect to the other (Split & Delay). In the (background-free) intensity autocorrelation scheme, both pulses are focused non-collinearly into a non-linear medium ($\chi^{(2)}$). Due to momentum conservation the fraction of the second harmonic signal created by absorption of a photon from each pulse, is emitted on the bisecting axis of both wave vectors. This fraction is identical to Term 2.12b: the intensity autocorrelation. When both beams are focused collinearly into the medium and the delay is sampled with sub-cycle accuracy the FRIAC signal equivalent to the sum of all terms (Equation 2.12) is retrieved.

The auto correlation technique is an incomplete characterization method. Figure 2.2 c-d shows the FRIAC signal and the intensity autocorrelation (blue) obtained for a Fourier-transform limited pulse in comparison to a pulse with a quadratic spectral phase (a linearly chirped pulse) with the same pulse duration.

For a Gaussian pulse the FWHM of the intensity auto correlation is given by $\sqrt{2}\tau_{\mathrm{P}}$ and the contrast between auto correlation signal and background signal is 3:1. For both pulses the intensity autocorrelation is identical and no phase information can be retrieved. The observed auto correlation signal is ambiguous in regard to the intensity envelope and the temporal phase of the pulse. Only when the pulse shape is known and no non-linear phase terms are present, the pulse duration can be inferred from the intensity auto correlation measurement.

In the FRIAC trace, the contrast is 8:1 and the oscillating terms are visible in both signals. For the chirped pulse these oscillations are only visible in the central region of the FRIAC signal, which is due to a lower coherence time of the pulse. For longer delays red-shifted frequency components are superimposed with blue-shifted components leading to a vanishing interferometric contrast. Consequently, the interferometric measurements can discriminate between a Fourier-limited pulse and a pulse with a non-linear phase. The second-order auto correlation signal shown here is always symmetric, as can be seen in Equation 2.12. Thus, the sign of a the second-order phase term cannot be discerned in the measurement. Although, some information of the temporal phase is accessible in a FRIAC measurement, it is still ambiguous in regard to the pulse shape and higher-order phase terms.

An overview of pulse characterization techniques more advanced then auto or cross correlation techniques can be found in the reviews Ref. [33] and [30]. These techniques try to overcome the limitations described above by combining a delay-dependent measurement with self-referencing techniques and spectral measurements and retrieve the complete spectral phase by advanced mathematical algorithms. For the sake of completeness the frequency optical gating technique (FROG) established by the group of Trebino *et al.* [34], as well as the SPIDER method (spectral phase interferometry for direct electric-field reconstruction) [35] shall be named here, as they are widely used techniques for the self-referenced reconstruction of the temporal amplitude and phase of pulses in the infrared to near ultraviolet spectral range.

The pulses used in the pump-probe experiments described in the later chapters, are in the vacuum ultraviolet spectral range, where neither self-referencing techniques, nor non-linear crystals for second harmonic generation are available. For a pulse duration of sub-20 fs and wavelength below 270 nm transmission optics are not feasible, because the pulse experiences a strong group delay dispersion inside the material, stretching the pulse in time. Thus, auto correlation techniques were realized in an ultra high vacuum environment, which utilize for example the two-photon ionization of rare gases as a non-linear signal. The ionization yield is then measured as a function of the delay between both pulses. The delay variation may be realized by scanning with a motorized stage, or by spatially encoding the delay and imaging non-linear response spatially. Both techniques have been realized in the group of Prof. Dr. Markus Drescher: A fringe-resolved interferometric auto correlator [36], as well as a single-shot intensity autocorrelator [28].

2.2 INTERACTIONS BETWEEN LIGHT AND ATOMS OR MOLECULES

Nowadays, ultrashort light pulses with pulse energies ranging from few nanojoules to many millijoules on the few-femtosecond to attosecond time scale may be realized in a laser laboratory. Depending on the wavelength and intensity reached by focusing the corresponding beam into an atomic or molecular target different interactions between the light field and the interrogated system are dominant.

At low field strength, the light field is acting as a small perturbation on the intrinsic electronic properties of the atom or molecule and electronic transitions between molecular or atomic states may occur. For ultrashort pulses with high pulse energies this perturbative picture is not applicable anymore. The coupling between the light field and the atomic or molecular potential is strong enough to introduce AC-stark shifts, create light-induced states or strong-field ionization. Furthermore, higher harmonics of the driving light field may be generated under these conditions. [22, 37]

2.2.1 PHOTOEXCITATION

The reaction dynamics in the focus of the presented work are induced by promoting electrons from the electronic ground state of the system to an excited state. The dynamics of this excited state then lead to the desired reaction products and decomposition of the molecule or the formation of fragments, and is imaged by ionizing the individual species.

Before addressing the ionization step, this section will focus on the photoexcitation of atoms and molecules. For a spectroscopist or molecular physicist one important question is, which electronic transitions in an atom or molecule may occur and how probable this transition is. The derivation and discussion of concepts important to this is following Refs. [38–41].

The time-dependent interaction between a light field and an atom can be described in a semi-classical picture. The atom will be treated quantum-mechanically, while the light field is described classically.

The action of the light field on an atomic system with a single active electron is given as a time-dependent perturbation to the stationary atomic system $\hat{U}(\mathbf{r}, t)$, where $\mathbf{r}$ is the position vector of the electron relative to the nucleus. The perturbation operator is then given in the dipole approximation as

$$\hat{U}(\mathbf{r}, t) = \mathbf{r}e_0 \cdot \mathcal{E}(\mathbf{r}, t) = -\mathbf{D} \cdot \mathcal{E}(\mathbf{r}, t). \tag{2.14}$$

$-\mathbf{r}e_0$ is the effective dipole moment of the electron and is written as $\mathbf{D}$. $\mathcal{E}(\mathbf{r}, t)$ is the real electric light field. In general the wavelength λ of the light is exceeding the atomic radius significantly ($\lambda \gg r_{\text{atom}}$ and $\mathbf{kr} \ll 1$) and the formula for the electric field in the plane-wave approximation can be rewritten as

$$\mathcal{E}(\mathbf{r},t) = \mathcal{E}_0\mathbf{e}\cdot e^{i(\mathbf{kr}-\omega t)} \approx \mathcal{E}_0\mathbf{e}\cdot e^{-i\omega t}, \tag{2.15}$$

where $\mathcal{E}_0$ is the amplitude of the electric field, $\mathbf{e}$ the polarization unit vector of the field, $\mathbf{k}$ the wave number, and ω the angular frequency of the light field.

To describe a transition between an initial electronic state $|a\rangle$ and a final state $|b\rangle$, the time-dependent Schroedinger equation needs to be solved:

$$i\hbar\frac{\partial}{\partial t}\Psi(\mathbf{r},t) = \hat{H}\Psi(\mathbf{r},t), \tag{2.16}$$

where $\Psi(\mathbf{r},t)$ is the wave function of the quantum system and $\hat{H}$ the Hamilton operator characterizing total energy of the system.

In first-order perturbation theory the Hamilton operator of the atomic system under the influence of an external light field is described as

$$\hat{H} = \hat{H}_0 + \hat{U}(\mathbf{r},t). \tag{2.17}$$

Here, $\hat{H}_0$ is the Hamiltonian of the stationary atomic system used to retrieve the wave function of the atomic system in the absence of external perturbations and $\hat{U}(\mathbf{r},t)$ is the perturbation operator defined in Equation 2.14. For a solution of the Schroedinger equation in the stationary picture the reader is referred to the text books mentioned earlier.

An ansatz to solve the time-dependent Schroedinger equation in the first-order pertubation theory, where the perturbation is considered small, is

$$\Psi(\mathbf{r},t) \approx \psi_a(\mathbf{r})e^{-i\omega_a t} + \sum_{j\neq a} c_j(t)\psi_j(\mathbf{r})e^{-i\omega_j t} \tag{2.18}$$

and $\psi_a(\mathbf{r})$ is the wave function of the initial state with the probability amplitude $c_a = 1$. For all other states with the wave functions $\psi_j(\mathbf{r})$ $|c_j| \ll 1$, when $j \neq a$.

In the experiment one is interested in the transition rate w_{ba}, which is the given as

$$w_{ba} = \frac{p_{ba}(t)}{t} = \frac{|c_b(t)|^2}{t}, \tag{2.19}$$

where $p_{ba}(t)$ is the probability to find the atomic system in an excited state $|b\rangle$ at a time t. The derivation of $p_{ba}(t)$ is described in detail for example in the book of Hertel & Schulz [38] and is omitted here.

Although, transition rates may be calculated by solving the time-dependent Schroedinger equation for a given atomic system and light field, it is convenient for the experimentalist to express the transition rate in terms of an effective cross section σ_{ba}.

In the dipole approximation the transition operator $\hat{\mathcal{T}} = \mathbf{De}/e_0$ is introduced here. The transition rate for an electronic transition from state $|a\rangle$ to $|b\rangle$ is then depending only on the spectral intensity I of the light field and the cross section $\sigma_{ba}^{(1)}$.

$$w_{ba}^{(1)}(I) = \sigma_{ba}^{(1)}(\omega)\frac{I}{\hbar\omega}, \qquad\qquad \sigma_{ba}^{(1)} \propto \left|\left\langle b\middle|\hat{\mathcal{T}}_{ba}\middle|a\right\rangle\right|^2 \tag{2.20}$$

A transition is resonant, when the frequency of the light field is equal to the transition frequency ω_{ba} of the electronic transition, and only then the cross section is significantly high. Furthermore, the transition dipole moment $\langle b|\,\hat{\mathcal{T}}_{ba}\,|a\rangle$ is only different from zero, when $\langle b|\,\hat{\mathcal{T}}_{ba}\,|a\rangle$ has even symmetry. In conjunction with angular momentum conservation this leads to the well-known selection rules in electronic transitions, neglecting spin-orbit coupling:

$$\begin{aligned} &\Delta J = 0, \pm 1 (J = 0 \not\leftrightarrow 0) \qquad\qquad && \Delta L = \pm 1 \\ &\Delta S = 0 && \pi_{gu} \not\leftrightarrow \pi_{gu}, \pi_{gu} \leftrightarrow \pi_{ug} \end{aligned}$$

Here J is the total angular momentum quantum number, L the azimuthal quantum number, S the spin quantum number. The last selection rule is the parity selection rule. In an electric dipole transition the parity of the initial state needs to be different from the final state, since the dipole operator has odd parity.

The same reasoning can be extended to multi-photon transitions, where two-photons are absorbed simultaneously and the transition proceeds through a (virtual) intermediate state i. The two-photon transition rate and cross section are given by

$$w_{ba}^{(2)}(I) = \sigma_{ba}^{(2)}\left(\frac{I}{\hbar\omega}\right)^2, \qquad\qquad \sigma_{ba}^{(2)} \propto \left|\sum\!\!\!\!\!\!\!\int_i \frac{\langle b|\,\hat{\mathcal{T}}_{bi}\,|i\rangle\,\langle i|\,\hat{\mathcal{T}}_{ia}\,|a\rangle}{E_{ia}-\hbar\omega}\right|^2. \tag{2.21}$$

As can be seen, the transition rate is depending on the squared intensity. This intensity dependence can be generalized for all multi-photon processes and $w_{ba}^{(n)}(I) \propto I^n$. Measuring the intensity dependence of a signal induced by a multi-photon process is a widely used method to extract the non-linearity of the process.

The two-photon cross section $\sigma_{ba}^{(2)}$ is proportional to a transition moment, where all intermediate states need to be included in the integral, both finite and continuum states. In two-photon transitions the transition operator is applied two times and the selection rules are different in regard to the single-photon selection rules:

$$\begin{aligned} &\Delta J = 0, \pm 2 \qquad\qquad && \Delta L = 0, \pm 2 \\ &\Delta S = 0 && \pi_{gu} \not\leftrightarrow \pi_{ug}, \pi_{gu} \leftrightarrow \pi_{gu} \end{aligned}$$

Without spin-orbit coupling two-photon and single-photon transitions are orthogonal to each other. Thus two-photon transitions enables excitation of atomic states, which are spectroscopically dark.

The present work mostly focuses on disclosing reaction dynamics of molecules. In the previous derivation, we focused on atomic systems, with a single active electron and a nucleus. In molecules one has to consider not only the electron wave function, but also the wave function of all nuclei constituting the molecule [41]. Depending on the conformation of the molecule (the nuclear structure), the wave function of the electrons is different. Thus, the Schroedinger equation for a molecule, needs to consider both the electron coordinates $\mathbf{r}$, as well as the nuclear coordinates $\mathbf{R}$ and is written as

$$\hat{H}\Psi(\mathbf{r},\mathbf{R}) = E\Psi(\mathbf{r},\mathbf{R}). \tag{2.22}$$

In many cases, the nuclei and electrons can be treated independently in the Born-Oppenheimer approximation. The motion of nuclei and electrons is proceeding on time scales, which deviate by orders of magnitude. While electrons move on the attosecond time scale, the nuclei are considered frozen in time. The movement of nuclei is proceeding on the femtosecond time scale, and the electrons are considered as an effective electron density adiabatically following the nuclei. This leads to a product ansatz for an electronic wave function $\Psi_e(\mathbf{r},\mathbf{R})$ and a nuclear wave function $\Psi_N(\mathbf{R})$:

$$\Psi(\mathbf{r},\mathbf{R}) = \Psi_e(\mathbf{r},\mathbf{R})\Psi_N(\mathbf{R}). \tag{2.23}$$

Consequently, a Hamiltonian $\hat{H}_e$ for the electrons and another Hamiltonian for $\hat{H}_N$ for the nuclei is derived and the stationary Schroedinger equation is given as

$$\hat{H}_e\Psi_e(\mathbf{r},\mathbf{R}) = E_e(\mathbf{R})\Psi_e(\mathbf{r},\mathbf{R}) \tag{2.24}$$

$$(\hat{H}_N + E_e(\mathbf{R}))\Psi_N(\mathbf{R}) = E\Psi_N(\mathbf{R}). \tag{2.25}$$

The eigenvalues for the electron energy $E_e(\mathbf{R})$ are depending only on the molecular conformation and constitute the potential energy surface. The total energy of the nuclei is described, by $\hat{H}_N$ (the kinetic energy of the nuclei) in the potential of the electrons. Consequently, the nuclei are moving in the effective potential of the electrons.

Transitions between electronic states of molecules may also be described in first-order perturbation theory. The Franck-Condon principle states, that these dipol transitions are always vertical, which means that the molecular geometry is unchanged during a transition.

The effective transition rate is derived in the same way as for an atomic system (Equation 2.20), but the effective cross section of the process is not only depending on the transition dipole moment. Figure 2.3 shows vertical electronic transitions for two diatomic molecules, where the electronic potential can be described as a Morse potential. For the Morse potential the static Schroedinger equation can be solved analytically, leading to a sequence of vibrational states ν_i for the electronic states $|a\rangle$ and $|b\rangle$. The nuclear probability density for each state is indicated in the figure.

For such a system the effective excitation cross section is given by

$$\sigma^{(1)}_{b\acute{\nu}|a\nu} \propto \left|\langle b|\, \hat{\mathcal{T}}_{ba}\, |a\rangle\right|^2 \left|\langle b\acute{\nu}|a\nu\rangle\right|^2, \tag{2.26}$$

where $|\langle b\acute{\nu}|a\nu\rangle|^2$ is the Franck-Condon factor for an electronic transition from $|a\rangle$ in the vibrational state ν to $|b\rangle$ in the vibrational state $\acute{\nu}$. The Franck-Condon factor is given by the

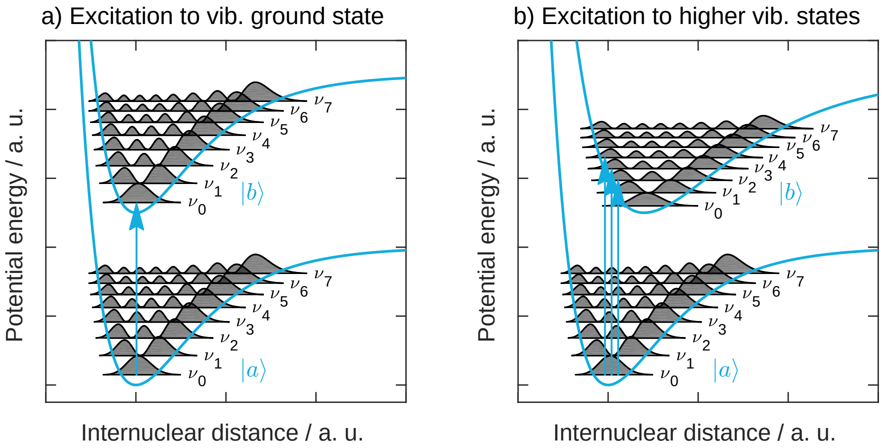

FIGURE 2.3– Vertical photoexcitation in molecules including vibrational energy levels in a Morse potential. (a) Electronic transition from vibrational ground state to vibrational ground state. (b) Electronic transition from vibrational ground state to vibrationally excited states.

overlap between the contributing vibrational wave functions. This is emphasized in the comparison between Fig. 2.3 a and b. In the first case, the Franck-Condon factors favor a transition from the vibrational ground state of the initial electronic state to the vibrational ground state of the excited state. When the equilibrium distance of the electronic potential of state $|b\rangle$ is shifted in comparison to the equilibrium distance of the electronic ground state, several higher vibrational states are populated.

The interplay between the dipole transition selection rules and the effect of the molecular geometry govern the observed absorption and emission spectrum of a molecule. In this thesis, the excitation to high-lying electronic states, as well as vibrational excitation will be used to trigger molecular reaction dynamics. The shape of the potential energy surfaces of individual electronic states and the coupling between them determine the fate after excitation, which will be discussed in a later section.

It is important to remember, that all derivations stated here are only valid, when the light field is considered a small perturbation to the atomic or molecular potential. This means, that the intrinsic dynamics are only accessible at small field strengths. For a stronger field strength, the action of the light field on the atomic or molecular system may change the potential energy landscape, e. g. shift energy levels in an atom, or create light-induced molecular states. [19–21, 42] In an experiment this leads to a trade-off between signal strength (typically increasing with intensity) and access to intrinsic properties. The question is, whether one wants to study nature or see where the light-field interaction is driving the scrutinized system, as in coherent control [43, 44].

2.2.2 PHOTOIONIZATION

When the energy of the photon exceeds the binding energy of the electron, absorption of a photon promotes the electron to a continuum state, and leaves the molecule or atom in a positively

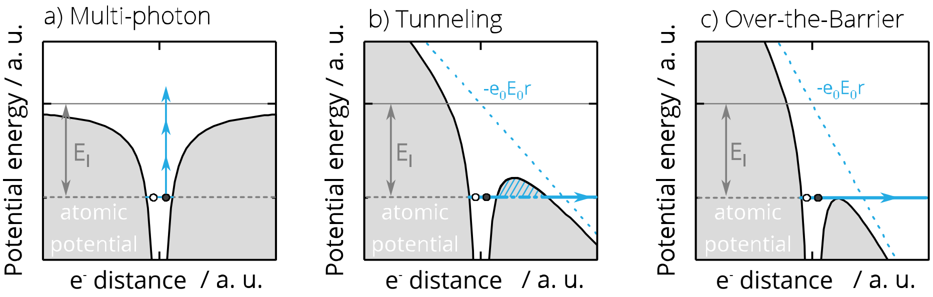

FIGURE 2.4– Photoionization processes for different light field strengths. (a) Multi-photon ionization under perturbative conditions. (b) Tunneling ionization. (c) Over-the barrier ionization.

charged state. Depending on to the intensity of the light field inducing this ionization process, the interaction can be perturbative, or non-perturbative.

In the perturbative case, single or multi photon ionization can be described by an approach similar to photoexcitation, where the final state is described by a continuum of states for the escaping electron and another state for the (molecular) ion. With increasing intensity and wavelength, the ionization process is different, and is more accurately described by the interaction between the light field and the atomic or molecular potential, in which the electrons are confined.

Figure 2.4 depicts different ionization processes for a single active electron trapped in a Coulomb potential. The binding energy E_I of the electron in the stationary ground state is shown in all panels. In the semi-classical approximation the atomic potential is perturbed by the oscillating field of the light pulse

$$V(r,t) = -\frac{Ze_0^2}{4\pi\epsilon_0 r} - e_0\mathcal{E}(t)\cdot r, \tag{2.27}$$

where $V(r,t)$ is the effective potential, Z the charge number of the system, e_0 the electron's charge and ϵ_0 the vacuum permittivity. For the sake of simplicity the light field is polarized along the r coordinate for the distance between the electron and the core [38].

When the effect of the electric field is negligible the photoionization can be treated in n-th order pertubation theory as a multi-photon process (Fig 2.4 a). Depending on the field strength, the effective potential may lead to the observation of strong-field effects. One of them is tunneling ionization, where the atomic potential is deformed such, that the electron may tunnel through the barrier into the continuum (Fig 2.4 b). In a more extreme case, this barrier becomes so small, that the barrier suppression exceeds the binding energy of the electron and the latter may escape freely from the nucleus (Fig 2.4 c). This is called over-the-barrier ionization.

Which mechanism is dominant, depends not only on the field strength (or intensity) of the light field, but also on the wavelength. For longer wavelengths, the field is oscillating slower, and the electron has more time to escape the potential; either by tunneling or over-the-barrier ionization. This is reflected in the adiabaticity parameter γ introduced by Keldysh [45], where

$$\gamma = \sqrt{\frac{E_I}{2U_P}}. \tag{2.28}$$

γ is proportional to the ratio between the binding energy E_I of the electron and the ponderomotive potential

$$U_P = \frac{e_0^2 I}{2c\epsilon_0 m_e \omega^2}, \tag{2.29}$$

where I is the instantaneous intensity of the light pulse, c the speed of light, m_e the electron mass and ω the angular frequency of the light field. As a rule-of-thumb the ionization process is proceeding by multi-photon ionization for $\gamma \gg 1$ and by tunneling or over-the-barrier ionization for $\gamma \ll 1$.

In the regime, where $\gamma \approx 1$ strong-field effects need to be considered also in multi-photon ionization, since all intermediate state in such a scheme must be considered for the ionization cross section, as has been shown in Eqn. 2.21 for multi-photon excitation. In the non-resonant case, where the frequency of the light field is not equal to any transition frequency of the system, the potential energy shift of (highly) excited states is approximated by an up-shift due to the ponderomotive energy of the light field

$$E_i(I) = E_i(I=0) + \Delta E(I) \approx E_i(I=0) + U_P(I). \tag{2.30}$$

This is essentially the dynamic quadratic Stark shift (or AC Stark shift).

As already discussed for the photoexcitation, also the multi-photon ionization rate w_{MPI} can be described in terms of an effective photo ionization cross section σ_n and is proportional to the intensity raised to the power of n:

$$w_{\text{MPI}}(I) = \sigma_n(I)\left[\frac{I}{E_{\text{ph}}}\right]^n. \tag{2.31}$$

To also consider the effects of an AC stark shift $\sigma_n(I)$ is represented as a function of the intensity here, because both intermediate states and the ionic ground state may be shifted upward in energy. Consequently, the cross section is changing, or the degree of non-linearity might increase for high intensities.

When the ionization process is pertubative and the ionization energy exceeds the photon energy, non-linear photoionization may be used for the temporal characterization of ultrashort pulses. It was shown in Section 2.1.1 that auto correlation techniques rely on a signal, which is depending non-linearily on the intensity I, which is the case in multi-photon ionization. For radiation in the vacuum-ultraviolet spectral range, where transmission optics are not feasible due to high dispersion and low transmission, multi-photon ionization is an ideal method to extend auto correlation techniques into this spectral range.

In the tunneling regime, the ionization can be described in the Ammosov-Delone-Krainow (ADK) model [46–48]:

$$w_{\mathrm{ADK}}(I) = |C_{n^*0}|^2 \, \frac{E_I}{\hbar} R^{2n^*-1}(I) \exp\left(-\frac{R(I)}{3}\right), \tag{2.32}$$

where the quantities $R(I)$, C_{n^*0} and the effective principal quantum number n^* are defined as

$$R(I) = \frac{4E_I^{3/2}}{\hbar e}\sqrt{\frac{\epsilon_0 c m_e}{I}}, \tag{2.33a}$$

$$|C_{n^*0}|^2 = \frac{2^{2n^*}}{n^*\Gamma(n^*+1)\Gamma(n^*)}, \tag{2.33b}$$

$$n^* = Z\sqrt{\frac{E_I^H}{E_I}}. \tag{2.33c}$$

E_I^H is the ionization potential of the hydrogen atom, Z the charge state of the resulting ion and $\Gamma(z)$ the gamma function. For a detailed derivation the reader is referred to the above mentioned references.

In the extreme case of over-the-barrier ionization, ionization is certain in a simple threshold model, when the barrier suppression exceeds the binding energy of the electron. This over-the-barrier ionization intensity is given by

$$I_{\mathrm{OBI}} = \frac{c}{128\pi}\left(\frac{4\pi\epsilon_0}{e_0^2}\right)^3 \frac{E_I^4}{Z^2} \tag{2.34}$$

and can be calculated in the classical model from Equation 2.27.

This list of strong-field and multi-photon interactions is by far not complete, but gives an overview of the interaction schemes responsible for the creation of ions in the experiments, which will discussed in Chapter 4. While above-threshold ionization (ATI) does not need to be considered, when only ions are observed not electrons, rescattering of the electron emitted by strong-field ionization is a pivotal process in generating radiation in the vacuum and extreme ultraviolet regime.

2.2.3 High-order Harmonic Generation

When an ultrashort laser pulse with an intensity in the tunneling or over-the-barrier ionization regime is focused into a noble gas target, odd harmonics of the light pulse frequency may be created. McPherson *et al.* [37] and Ferray *et al.* [22] observed this process with UV radiation with intensities above 10^{15} W cm^{-2} and infrared radiation ($I > 10^{13}$ W cm^{-2}), respectively. The single atom response responsible for this process is explained semi-classically in the three-step model [49].

This model is illustrated in Figure 2.5 a. First the atomic potential is perturbed by the strong light field (1), as was laid out in the previous section, and an electron is emitted either by tunneling or over-the-barrier ionization. Electron and ion are not immediately separated and a rescattering process may occur. In the next step, the electron is first accelerated away from the nucleus by the ponderomotive potential induced by the oscillating light field (2). When the amplitude of the field

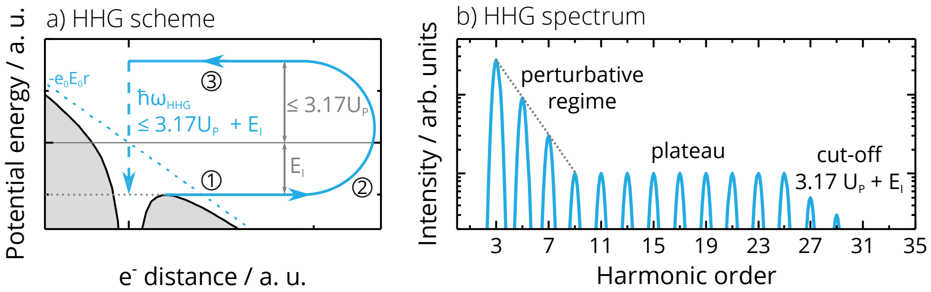

FIGURE 2.5– High-order harmonic generation (HHG) scheme and spectrum. (a) Three-step model of HHG: (1) strong-field ionization, (2) acceleration and deceleration in the electric field, (3) recombination (adapted from Ref. [38]). (b) HHG spectrum.

changes sign, also the ponderomotive force changes direction and the electron is first decelerated and then moves back in direction of the nucleus. In the final step, the electron is recaptured by the nucleus, and light with an energy

$$\hbar\omega = E_I + W_{\text{kin}} \leq E_I + 3.17 \cdot U_P \tag{2.35}$$

is emitted, where W_{kin} is the kinetic energy the electron gained due to acceleration in the ponderomotive potential (3). The upper limit of the photon energy emitted, the so called energy cut-off, is due to the maximum of kinetic energy the electron gains, when it is emitted at an phase angle of the light field of 17° [49].

Of course, the three-step model does only include the interaction between the classical light field and a single electron, and the interaction between the created ion and the electron is neglected. A quantum-mechanical analysis of the processes in the strong-field approximation was presented, for example by Lewenstein *et al.* [50]. At the time of preparation of this work, theoretical analysis of the high-harmonic generation (HHG) process is still in the focus of many published articles in the literature, because HHG is not only a method to create radiation in the XUV spectral region with pulse durations as short as 43 as [51], but also a tool in spectroscopy [52–54]. For these means, both atoms and molecules are considered in these studies [55].

When high-order harmonics are created in noble gases, a typical HHG spectrum as shown in Fig. 2.5 can be divided into three areas: The perturbative low-order harmonic regime, where the conversion efficiency is the highest and is steadily decreasing; the plateau region, where the conversion efficiency is constant; and the energy cut-off determined by Equation 2.35, where the harmonic output is vanishing rapidly. As presented in Fig. 2.5 only odd harmonics are emitted, when a centro-symmetric medium, such as a noble gas atom, is used, due to symmetry reasons.

The conversion efficiency is of course not only determined by the single atom response, as described by the three-step model. When the generating fundamental pulse is passing through the gaseous medium, an intense harmonic output is only achieved, when the single atom emission is occurring in phase [56]. The phase-matching of the fundamental pulse and the harmonic pulses is experimentally achieved by controlling different parameters, for example the nature and density of the gas medium, the focusing conditions (focal position and Rayleigh length) of the driving pulse, as well as the spectral phase of the fundamental pulse. The theoretical considerations for phase-matching conditions aimed at high conversion efficiencies in the lower or higher-order harmonics have been discussed previously in References [57–59].

In this work, an Argon gas cell inspired by the design of Takahashi *et al.* [23] and implemented by T. Gebert and D. Rompotis [25] was used to create the third and fifth harmonic of the Ti:Sapphire laser with a respective wavelength of 268 nm and 161 nm. While the experimental details will be discussed in Section 3.1, the rationale of creating UV radiation from an Argon gas target will be explained here.

A combination of the third and fifth harmonic may be used to initiate photoreactions in a variety of molecules with atmospheric importance, such as water, oxygen or iodomethane by single or two photon absorption. The time scale of these photoreactions may be as short as a few femtoseconds [60, 61]. While 268-nm radiation can be easily prepared by third harmonic generation in non-linear crystals with high conversion efficiency, the same is not true for 161-nm radiation. Additionally the pulse duration of pulses created in crystal is often comparable to the driving fundamental pulse duration, due to dispersion in the non-linear crystal, when the introduced dispersion is not compensated.

Creating both, the third and fifth harmonic, by low-order harmonic generation in Argon counteracts this dispersion problem. Since low-order harmonic generation can be treated as a perturbative process, the pulse duration of the generated harmonics is given by

$$\tau_n = \frac{1}{\sqrt{n}}\tau_{\mathrm{IR}}, \tag{2.36}$$

where n is the harmonic order. Thus, the pulse duration is intrinsically reduced by this process. Additionally, both harmonics are created from the same source, and are consequently synchronized in time. The conversion efficiency in the perturbative regime (see Fig. 2.5) is also high enough to drive linear and non-linear transitions in atoms and molecules. Even strong-field effects may be invoked by tightly focusing the third harmonic, as will be shown later. Finally, by controlling the phase-matching parameters, the harmonic intensity can be tuned in a wide range allowing to operate in a weak-field regime, where the intrinsic dynamics of the interrogated molecule are accessible, or in a strong-field regime, where the interaction between the light field and the system governs the observed experimental signal.

2.3 EXCITED STATE DYNAMICS OF MOLECULES

In the previous section the fundamentals describing the interaction between light pulses and atoms and molecules were described, which lie at the heart of pump-probe experiments. The preparation of VUV radiation necessary for initiating photoreaction dynamics and interrogating the evolving reaction was discussed, as well as the excitation of electronic states in molecules (pump step) and ionization (probe step). This section focuses on the dynamics of a molecular system after excitation and how to describe them.

2.3.1 NUCLEAR WAVE PACKETS

Section 2.2.1 considered only transitions between single states; for example an excitation from the lowest vibrational state of the electronic ground state to any single vibrational state of an

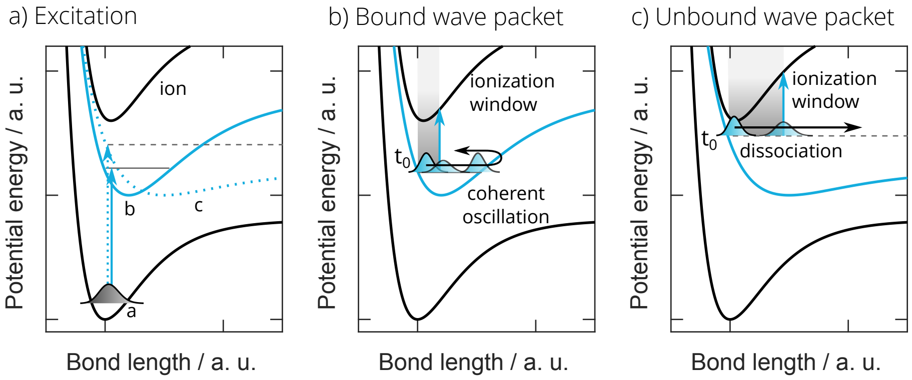

FIGURE 2.6– Nuclear wave packet dynamics in a bound and unbound state and detection in an ionization window. (a) Creation of two different wave packets from the electronic bound state. (b) Coherent oscillation of a wave packet in a bound potential. (c) Temporal evolution of the wave packet during dissociation.

excited electronic state (see Fig. 2.3 for an example of such a transition). But the bandwidth of a few-femtosecond pulse is in general large enough to drive a transition to several vibrational states in the same electronic excited state. The superposition of vibrational wave functions can be described as a molecular vibrational wave packet. The evolution of the wave packet is determined by the potential energy landscape of the excited electronic state and its coupling to other states of the molecule.

When a delta pulse is considered, which drives the system from an initial state $|a\rangle$ to a manifold of vibrationally excited states of an electronically excited state $|b\rangle$ at time $t = 0$, the resulting coherent state or wave packet can be written as superposition of vibrational eigenstates of the system [31]

$$|\psi_w\rangle = \sum_i^n c_i \, |b_i\rangle \, e^{-i\omega_i t}, \tag{2.37}$$

where the coefficients c_i depend on the transition dipole moment and the Franck-Condon factors, as was discussed in Sec. 2.2.1. For a real pulse also the temporal and spectral properties of the ultrashort pulse need to be considered. The spectrum determines, which states are accessible and the temporal phase and envelope of the pulse defines the temporal properties of the wave packet. Consequently, one may control the shape of the wave packet by tailoring the spectral and temporal properties of the light field used to coherently create the wave packet in the excited state. By these means, a reaction may be steered along a trajectory, which leads to the desired products. Thus, coherent control of reactions has evolved over the last twenty years into an important field of research [43, 44]. But before taking control, one has to first visualize and understand, what is happening to a system without strong external perturbations.

Figure 2.6 shows two examples of wave packet dynamics, which may be observed after excitation. All states are represented by one dimensional Morse potentials. In Fig. 2.6 a the initial excitation from the ground state is depicted. Here, the wave packet is either created in the bound state b or the the dissociative state c, where dissociative means, that the photon energy exceeds the binding energy of the excited state potential and the wave packet is formed by a superposition of continuum states.

In the first case (Fig. 2.6 b) the wave packet is confined to the excited state potential. When no coupling between the populated vibrational states and other states exists, the wave packet will evolve only in these states. This leads to a coherent oscillation, where the wave packet is reflected at the walls of the potential well and the approximate classical vibration frequency of the bond is observed. Depending on the detection scheme of a time-resolved experiment, this coherent oscillation may be visible in the pump-probe trace. In the experiments presented later, ionization from the excited state for example to the ionic ground state is used as a probe. When ionization is only possible for molecular geometries near the Franck-Condon zone (shown as the ionization window in Fig. 2.6 b) of the initial excitation, the coherent oscillation of the wave packet leads to an oscillation of the observed ion yield, a so called revival.

In this simple example, the wave packet will live forever and the coherent oscillation persists. In a real system even for an uncoupled electronic state, relaxation to the vibrational ground state and finally to the electronic ground state by fluorescence must be considered. Of course, these processes (on the picosecond or nanosecond time scale) are slow compared to the nuclear vibrational period (typically few tens of femtoseconds).

But excitation is also possible to an unbound state, which leads to dissociation of the molecule, as depicted in Fig. 2.6 c. Here, the wave packet is formed by a superposition of continuum states and the wave packet experiences a repulsive potential. This dissociation can then be tracked in a time-resolved experiment with an ion detection scheme. Because there are no revivals, the molecular ion yield will decay over time. The time constant of this decay is determined by the wave packet dynamics, which are governed by the excited state potential energy surface, and the final ionic state potential, since ionization is only possible, when the photon energy exceeds the ionization energy inside the ionization window. In these simple examples of isolated excited states, where either a coherent oscillation or a dissociation is proceeding on a few femtosecond time scale, the point in time, where the molecular geometry is distorted such, that ionization is not possible by a single probe photon can be clocked precisely in a time-resolved experiment.

In complex molecules, the crossing from one excited state to another can not only be facilitated by emitting photons. The coupling between individual vibrational modes may for example lead to a vanishing of a coherent oscillation. When more than two vibrational degrees of freedom exist, crossings between electronic states are also possible, where the adiabatic picture of the Born-Oppenheimer approximation is not accurate anymore, and the potential energy surface become degenerate. Transitions at these conical intersections proceed ultrafast compared to the time constant of deactivation via a dipole transition and are responsible for a multitude of ultrafast relaxation phenomena in nature [10–12].

2.3.2 NON-ADIABATIC DYNAMICS

A system of two electronic potential curves, represented as Morse potentials in Figure 2.7 a, is considered. In a diatomic system with one singular degree of freedom, both potentials may not intersect, when they possess identical symmetry, due to the no-crossing rule [62]. The result of this is the emergence of an avoided crossing, which leads to the formation of two separated potential energy curves. At the point, where the crossing is avoided, the Born-Oppenheimer approximation breaks down and the non-adiabatic coupling between the initial states is strong.

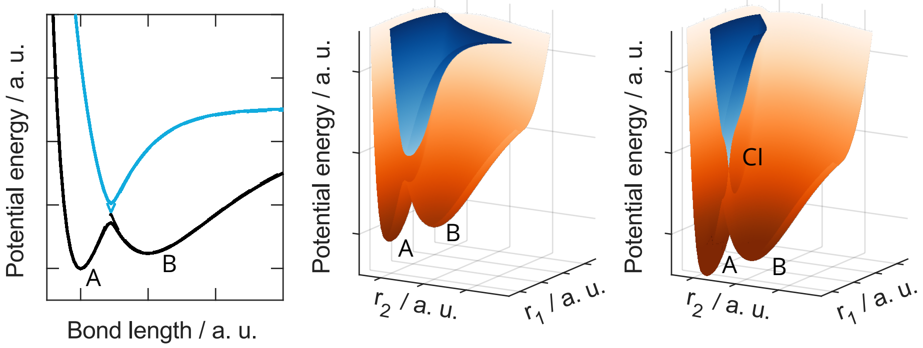

FIGURE 2.7– Non adiabatic dynamics in one and two dimensions. (a) Avoided crossing due to the no-crossing rule. (b) Avoided crossing in the two-dimensional representation. (c) Branching space of a conical intersection between excited and ground state.

As can be seen in Fig. 2.7 b, the electronic state does possess two minima, and a chemical reaction may be considered, where two molecular geometries (A, B) are stable in the ground state. When the molecule is excited to the excited state, which results from the avoided crossing, a non-radiative transition back to the ground state is impossible. Thus, a photoreaction, where the molecular geometry is confined to the potential well B, can only be realized by a dielectric transition and depending on the excited state wave packet dynamics both geometries A and B maybe formed.

Strictly, the no-crossing rule states, that two electronic potential surfaces may not intersect in more than $N-2$ degrees of freedom. For a non-linear triatomic molecule (three vibrational degrees of freedom) the non-adiabatic coupling may lead to the formation of a conical intersection. In the so called branching space, the conical intersection can be visualized as a funnel (Fig 2.7 c). In all other dimensions, the conical intersection forms a seam, where both potential energy surfaces are degenerate.

When the molecule is excited to the upper potential energy surface, the evolving wave packet is steered in the direction of the conical intersection, because the potential gradient is steepest in its direction. Thus, a conical intersection provides an efficient means to transfer population back to the electronic ground state. This transfer is proceeding on the same time scale as the wave packet dynamics, and thus may be completed in few tens of femtoseconds. Competing reaction pathways, such as relaxation by fluorescence, are effectively suppressed, because their time scale is orders of magnitude slower.

Conical intersection are responsible for many excited state dynamics, such as intersystem crossing or internal conversion, which open up photoreaction path ways. An important example is human vision [13]. After photoexcitation the rhodopsin protein in the human eye undergoes a rapid (E)-(Z) isomerization. This first step in a chain of biochemical reactions is facilitated by a conical intersection.

This chapter presented an overview of the theoretical background necessary to understand several aspects of a time-resolved experiment focusing on molecular dynamics. First, a description of ultrashort light pulses was given, focusing on their temporal and spectral representation, as well as their spatial properties in the paraxial approximation. Additionally, information on auto and cross correlation methods for the temporal characterization of these pulses was provided. The experiments presented in the following chapters rely on the generation of ultra short pulses in the vacuum ultraviolet spectral range and their use to initiate and interrogate photoreaction dynamics. Consequently, the underlying theory for the interaction between light and atoms or molecules was presented in detail, where the light field was treated as a perturbation to the atomic and molecular potential, as well as interactions involving stronger fields, such as strong-field ionization and high-order harmonic generation. The chapter was concluded with the introduction of the wave packet picture, for the description of excited state dynamics in small molecules, which are later used to interpret time-resolved experiments in small molecules.

The next chapter will lay out the experimental considerations for the generation of ultrashort pulses in the vacuum ultraviolet spectral range. Thus, the harmonic generation apparatus and the diagnostic means for energy and spectral measurements will be introduced. Finally, the counter-propagating single-shot autocorrelation experiment, which is the key element to realize the time-resolved molecular dynamics experiments, is presented in detail.

3

ULTRASHORT HARMONIC PULSES

Creating ultrashort light pulses and manipulating their temporal and spectral properties is the initial step to enable the study of molecular reaction dynamics. The pioneering work of Ahmed Zewail and coworkers started the field of *Femtochemistry* and introduced the pump-probe technique. Here, two laser pulses with sub-picosecond duration are used to initiate a photoreaction by absorption of a pump photon and subsequently probing this reaction by absorbing another photon from the delayed probe pulse. Fluorescence, photoelectron or ion yields are then interpreted as a delay-dependent observable [1, 63]. With the evolution of the field and the advent of new technologies and methods nowadays experimentalists are able to create intense and short pulses also in the vacuum ultraviolet (VUV) spectral range. By these means the dynamics of highly excited states of diatomic molecules or small organic molecules can be studied with unprecedented temporal resolution.

This chapter focuses on the experimental methodology to create harmonic pulses in the (V)UV regime with intensities on the μJ level and pulse durations below 25 fs, as well as their characterization. For this a detailed description of the harmonic generation experiment starting from the Ti:Sapphire driving laser is given, followed by the characterization of the spectrum and intensity of the harmonic pulses. Furthermore, the experimental design of the colliding-pulse single-shot auto correlation experiment [28], which is the key element of this work, is presented with an additional focus on the improvements to the processing and evaluation of raw experimental data.

3.1 GENERATION OF INTENSE VACUUM-ULTRAVIOLET PULSES

Over the past years a variety of methods to extend harmonic generation into the 5–10 eV photon energy range have been proposed and implemented by different groups. While conventional non-linear crystals such as KBBF ($KBe_2BO_3F_2$) suffer from strong dispersion of the VUV pulses and low transmission [64], harmonic generation in noble gases or random quasi-phase matched SBO (SrB_4O_7) [65] can be applied to create VUV radiation with a sufficiently high conversion efficiency and sub 100-fs pulse duration.

When a noble gas is used as a medium to create VUV pulses, one can distinguish between different generation schemes: Non-resonant multi-photon harmonic generation [25, 66] in the perturbative regime of high-order harmonic generation, and off-resonance and near-resonance four-wave-difference-frequency-mixing (FWDFM) schemes in collinear or non-collinear geometry [67–73]. While the conversion efficiency is higher for the FWDFM approach, the multi-photon approach benefits from the intrinsic shortening of the pulse duration compared to the driving laser pulse. In the perturbative regime, the expected duration is shorter by a factor of $\sqrt{n}$, where n is the creation process's order of non-linearity.

In this work a tunable-length gas cell was used to create the third and fifth harmonic of the Ti:Sapphire laser (268 nm, 161 nm) by multi-photon harmonic generation in argon. A brief explanation of the creation of ultrashort near-infrared laser pulses in a commercial Ti:Sapphire laser system will be presented, followed by a detailed description of the harmonic generation and its characterization.

3.1.1 Femtosecond Laser System

A commercial femtosecond laser system (Amplitude Technologies Pulsar) was used to create ultrashort near infrared pulses in a chirped pulse amplification scheme utilizing Ti:Sapphire crystals as a gain medium. In a CPA scheme < 10 fs broadband pulses delivered by a self-mode-locked Ti:Sapphire oscillator are temporally stretched (chirped) by a factor of 1000–10000 to safely amplify the pulses in solid materials in a regenerative and multi-pass amplifier, before the pulses are recompressed to < 40 fs.

In this implementation a Femtolasers Synergy Pro oscillator delivers < 10 fs pulses with an output energy of 4.1 nJ, a central wavelength of 772 nm, and a bandwidth of 90 nm at a repetition rate of 75 MHz [74]. The pulses are then stretched to 10–100 ps in an aberration-free Öffner-triplet single-grating stretcher [75]. Before the first amplification stage the repetition rate is reduced to 1 kHz by a combination of Pockel's cell and polarizer acting as a pulse picker. In the regenerative amplification stage the pulses are amplified to around 0.8 mJ by passing multiple times through a Ti:Sapphire crystal pumped by a diode-pumped laser operating at 527 nm (Photonics Industries DM30). The cavity of the regenerative amplifier ensures a high-quality beam profile and is equipped with an acousto-optic programmable gain control filter (AOPGCF, Fastlite Mazzler), which counteracts gain-narrowing effects and increases the achievable amplified bandwidth to 90 nm.

After the pulses exit the regenerative amplifier cavity every fortieth pulse is picked from the kHz pulse train and redirected. This results in two individual pulse trains with a respective repetition rate of 25 Hz and 1 kHz, which are both amplified a second time in separate multipass amplification stages. The 1-kHz multipass amplifier is pumped by the same laser as the regenerative amplifier, while the gain in the 25-Hz multipass amplifier is created by a flashlamp-driven 532-nm Nd:YAG laser (Big Sky Laser CFR-200). In these last amplification stages the pulses are amplified to 4.8 mJ in the 1-kHz branch and 22 mJ in the 25-Hz branch. Afterwards the pulses are compressed to a duration of < 40 fs in a double-grating compressor. Due to transmission losses in the compressor, the resulting output power is reduced to 3 mJ and 15 mJ in the 1-kHz and 25-Hz branch respectively. Furthermore, the spectral phase of the output pulses can be manipulated for both output branches individually with an acousto-optic programmable dispersive filter (AOPDF, Fastlite Dazzler) located between the stretcher unit and the regenerative amplifier. By these means higher-order dispersion terms can be compensated to achieve a final pulse duration close to the Fourier-transform limit given by the spectral bandwidth of the pulse.

TABLE 3.1– Operation parameters of the Amplitude PULSAR laser system. Columns marked by † refer to parameters, when the AOPGCF was operated. Uncertainties given represent the day-to-day fluctuations during the time the laser system was operated for this work.

	Pulse energy (mJ)	Central wavelength (nm)	Bandwidth FWHM (nm)	Pulse duration (fs)
25 Hz	14 ± 1	805 ± 2	29 ± 1	37 ± 2
25 Hz†	14 ± 1	805 ± 2	69 ± 1	24 ± 1
1 kHz	2.9 ± 0.1	805 ± 2	29 ± 1	37 ± 3

For this work the 25-Hz branch of the laser system has been utilized exclusively. Typically an optimized output pulse energy of 13–15 mJ has been achieved with a measured shot-to-shot energy fluctuation of ±2%, and a pulse duration of 35–39 fs, since the AOPGCF was not operated on a daily basis. Table 3.1 gives an overview of the laser system's key characteristics for both branches. The pulse duration has been measured by a commercial pulse diagnostic device (APE SPIDER), which utilizes SPIDER, a self-referencing technique relying on spectral-shearing interferometry [35]. The spectral phase retrieved by SPIDER is used to optimize the compression of the pulses by a feedback algorithm programming the AOPDF.

3.1.2 HARMONIC GENERATION SCHEME

To efficiently generate harmonic radiation from intense few-fs pulses delivered by the Ti:Sapphire laser system a high beam quality is pivotal. Non-linear effects occurring upon propagation of intense pulses through a medium or material dispersion spoiling the beam quality need to be avoided. This is achieved by propagating the beam through high vacuum (HV) as soon as possible and avoiding the use of transmission optics if feasible. Furthermore, means of controlling the experimental parameters for the driving laser and the non-linear medium, which determine the

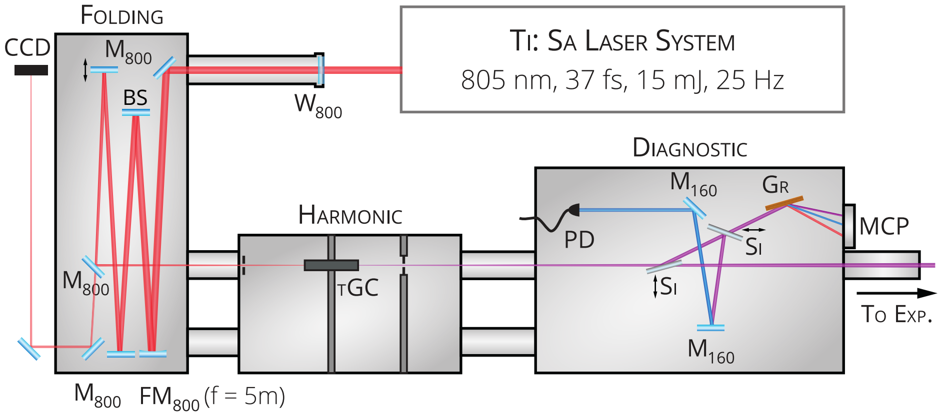

FIGURE 3.1– Schematic overview of the experimental setup.

harmonic pulses' properties, are necessary.

The fundamental pulse intensity can be tuned by inserting a $\lambda/2$ retardation plate into the beam path before the pulse enters the grating compressor. Due to the polarization-selective efficiency of the compressor gratings, a change of the pulse intensity is achieved by rotating the polarization axis of the infrared pulse.

After exiting the compressor box, the beam propagates 10 cm through air before it is coupled into the HV system, which is depicted in Fig. 3.1. An anti-reflection coated CaF_2 window (1.5 mm thickness, CVI Melles-Griot) is chosen as the air-vacuum interface (W_{800}), due to its low non-linear refractive index. The chosen thickness is close to the minimal safety thickness resulting from the pressure difference between air and the vacuum system ($<1 \times 10^{-3}$ mbar in the FOLDING chamber).

The harmonic generation scheme applied in this work is based on loose-focusing [24, 76] with a spherical dielectric mirror and a focal length of 5.0 m (HR800, 0° AOI, Laser Components). With a measured initial beam radius of 7.5 mm at $1/e^2$, the diffraction limited focal spot size is 342 µm and the Rayleigh length is 11.4 cm. Intensities of up to 4×10^{14} W cm^{-2} can be reached at typical operation parameters (see Table 3.1).

Since the laser laboratory is limited in space the convergent infrared beam is reflected – *folded* – multiple times in the FOLDING chamber. The laser beam is first redirected by a dielectric mirror optimized for high-reflectivity at (800 ± 40) nm (HR800) and an angle-of-incidence (AOI) of 45° (Laser Components). As depicted in Fig. 3.1 one of the plane folding mirrors can be moved on a translation stage to optimize the position of the focus for the harmonic generation. Plane dielectic mirrors (M_{800}) from multiple vendors (Laser Components, Layertec, CVI Melles-Griot, Eksma Optics) have been tested for folding the beam after the focusing mirror FM_{800}. The damage threshold of dielectric mirrors, often specified only for nanosecond pulses at ambient pressure, is reduced due to the vacuum conditions and the femtosecond pulse duration. This leads to emerging damages on the optical surfaces with increasing negative effects on the beam quality, which remains an unsolved problem. Typically 93 % of the intensity of the infrared pulse is transmitted through the FOLDING chamber.

To insure a high beam-pointing stability for the experimental end stations reached after a total beam propagation distance of up to 18 m, a beam stabilization system has been implemented together with Oliver Schepp in this work. One mirror (BS) in Fig. 3.1 is equipped with two Picomotor actuators (New Focus), enabling the control of the horizontal and vertical beam pointing. The leakage of the 45° redirecting mirror at the exit of the FOLDING chamber is coupled out of the vacuum system and imaged onto a CCD camera (IDS), acting as a far-field monitor for the replica of the focus in the harmonic generation source (Fig. 3.1). By implementing a LabView routine for calibrating the picomotor actuators, fluctuations in the position of the center-of-mass of the beam profile can be compensated with less than three iterations even for large deviations. The center-of-mass of the beam-profile is extracted at 25 Hz repetition rate and a moving average filter is used to ignore shot-to-shot fluctuations, which are hard to compensate at low repetition rates. Instead a slow stabilization is utilized, which eliminates the effects of beam drifts during measurement campaigns.

The harmonic source is located directly after the FOLDING chamber. A gas cell, which length is tunable between 5 and 15 cm, is filled with argon gas at a controlled backing pressure (TGC in the HARMONIC chamber). The gas is used as non-linear medium to create odd harmonics of the

TABLE 3.2– Reflectivity of the pulse energy diagnostics apparatus for 266 nm and 160 nm radiation. Reflectivity for Si is simulated with the XOP IMDB software, the reflectivities of the dielectric multilayer mirrors (R_{ML}) are taken from the measurement protocol supplied by the vendor.

Wavelength (nm)	$R_{Si}(75°)$	$R_{Si}(30°)$	R_{ML}	T_{Total}
266	0.48	0.69	0.99	**0.32**
160	0.67	0.60	0.91	**0.33**

fundamental laser light, by the harmonic generation process outlined in Section 2.2.3. To achieve a high target density the entrance and exit aperture of the cell is drilled by the laser pulse itself and a three-stage differential pumping scheme is realized with a Pfeiffer Splitflow turbopump.

Section 2.2.3 focused on the theoretical description of the high-order harmonic generation process, and described the dependency between the generation efficiency and the fundamental pulse characteristics, such as the spectral and temporal phase. In the experimental realization, this transfer is not straightforward. Thus, an iterative optimization of the harmonic source performance using reliable pulse diagnostics is advantageous.

The presented design allows the experimentalist to control a multitude of parameters for optimizing the output of the harmonic source for different requirements: The focus position in the gas cell can be adjusted, as well as the cell length. The generation medium can be chosen and its density can be controlled with an adjustable gas inlet valve. Furthermore the intensity, as well as the spectrum and spectral phase of the fundamental radiation can be manipulated with the methods outlined in the previous section.

3.1.3 PULSE DIAGNOSTICS

An optimization of the harmonic generation conditions can only be performed with the means to measure important pulse parameters, such as the intensity, spectrum and temporal characteristics.

The means to analyze the pulse energy and spectrum are located in the DIAGNOSTIC chamber (Fig. 3.1). In this chamber Si plane mirrors can be moved into the beam path to redirect the beam towards different diagnostic systems or to the experimental end stations (the first experimental end station is omitted here).

The pulse energy of the third and fifth harmonic is measured with a type-calibrated photodiode (Opto Diode, AXUV100G) optimized for the detection of photons with an energy above 6.5 eV. The beam is reflected by the first Si mirror at an AOI of 75°, which is Brewster's angle for s-polarized 800 nm radiation, leading to a suppression of the fundamental intensity by a factor of 10^{-5}. An additional reflection on a Si mirror redirects the beam over two dielectric mirrors onto the photodiode. To spectrally purify the pulse and isolate a single harmonic from the HHG pulse train, two sets of dielectric mirrors (Layertec GmbH), optimized for high reflectivity at 160 nm and 266 nm, respectively, are used.

The pulse energy, E, at the source is calculated from the signal of the photodiode, measured with an oscilloscope, by the following formula [77]:

TABLE 3.3– Properties of the harmonic radiation used throughout this project. Wavelength and photon energy are specified including the FWHM bandwidth of the pulse. The values for pulse energy and duration are the optimum values.

Wavelength (nm)	Photon energy (eV)	Pulse energy (µJ)	Pulse duration (fs)
268.4 ± 4.4	4.62 ± 0.05	17.6 ± 0.2	22 ± 1
161.0 ± 2.1	7.70 ± 0.08	1.1[a]	16 ± 1

---

[a] The uncertainty of this measurement is not available (see References [25, 57, 58]).

$$E(Harmonic) = \frac{1}{T}\frac{A}{50\Omega}\frac{q_{e^-}}{QE(\lambda)}\frac{\hbar\omega}{q_{e^-}}, \tag{3.1}$$

taking into account the transmission T of the diagnostic unit (see Table. 3.2), the time-integrated photo voltage A measured in nVs with a LeCroy oscilloscope and an impedance of 50 Ω. $QE(\lambda)$ is the wavelength-dependent quantum efficiency of the photodiode, $\hbar\omega$ the photon energy in eV and q_{e^-} is the electron charge.

The background signal of residual infrared radiation is measured independently and subtracted to extract the energy of the harmonic pulse. Under optimized conditions an output of 1.1 µJ was achieved for the fifth harmonic at 161 nm [25].

In addition to the energy measurement the harmonic beam can be redirected to a custom-built VUV spectrometer. The spectrometer consists of two exchangeable gratings (Al-coated grating, 600 lines/mm; Au-coated grating, 1200 lines/mm) optimized for lower- and higher-order harmonics respectively and a micro channel plate (MCP) + phosphor screen detector.

Table 3.3 gives an overview of typically achieved parameters, when the harmonic source is optimized for the third or fifth harmonic. The central wavelength and the spectrum of the fifth harmonic has been determined by fringe-resolved interferometric auto correlation [36] (FRIAC) and the third harmonic spectrum is calculated from this measurement. The pulse energy is measured with the AXUV100G photodiode and stated with its statistical error. The pulse duration of the fifth harmonic has been determined by FRIAC and the single-shot auto correlation method [28] applied in this work and presented in the next chapter. The pulse duration of the third harmonic is measured with the single-shot autocorrelator.

Both, the third and the fifth harmonic are generated in the so-called perturbative regime of high-order harmonic generation (see Section 2.2.3), where the pulse energy is dependent on the fundamental pulse intensity to the power of the degree of non-linearity. This can be shown, by measuring the output pulse energy as a function of the infrared pulse intensity, which is respresented as a double logarithmic plot in Fig. 3.2.

Here the infrared intensity is varied, while all other parameters, such as a cell length of 5.5 cm, the argon backing pressure and the temporal phase, are kept at their optimized values. The degree of non-linearity can be directly extracted from the graphs by linear regression and is in good agreement with the expectation of a third- and fifth-order process, respectively. Furthermore, it is obvious that the third-order process exhibits a higher efficiency and reaches saturation, while the

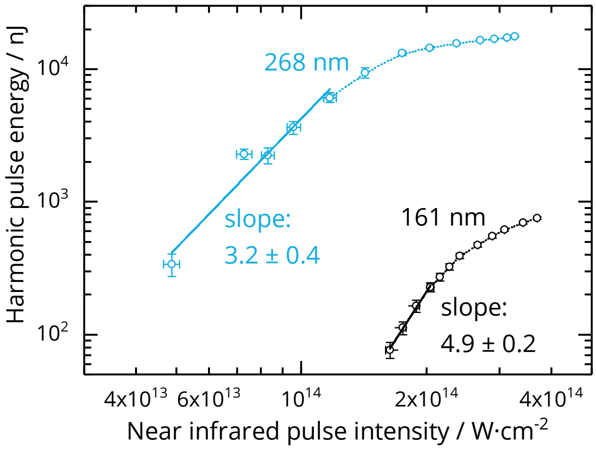

FIGURE 3.2– Intensity dependence of the harmonic radiation generated in the tunable length gas cell for different near-infrared driving laser intensities. Measurements have been performed with an optimized cell length of 5.5 cm in argon. Data set for 161 nm is taken from Ref. [25].

fifth harmonic pulse energy is still growing as a function of I^5. Hence, the ratio between third and fifth harmonic can not be tuned arbitrarily at the origin and has to carefully optimized later at the experimental end station.

3.2 COUNTER-PROPAGATING SINGLE-SHOT AUTO CORRELATION

Measurements in the spectral domain or the determination of the pulse energy can be carried out with electronic detectors, which respond on a nanosecond time scale, such as MCP detectors or photodiodes. As a result, the temporal characteristics of the VUV pulses are lost in these measurements. In the field of ultrafast laser science, a great number of methods have been developed in the UV/vis spectral range to overcome these limitations, which emerged from the auto- or cross correlation techniques, described in Section 2.1.1. The educational paper by Monmayrant *et al.* [30] gives a good overview of various methods, such as FROG [78], SPIDER [35] and their variants.

Most of these techniques rely on measuring the non-linear response created by superimposing two pulses with varying delay in a crystal. Realizing these methods for visible radiation is already a challenging task; transferring them into the VUV spectral range is further complicated by the peculiarities introduced in the beginning of this chapter (p. 37). Again, also the temporal diagnostics need to be implemented in an all-reflective manner and non-linear crystals are not feasible as a medium for auto correlation techniques, instead multi-photon ionization of noble gases is used to create a non-linear response.

In the group of Prof. Markus Drescher two experimental techniques were established, which address different aspects of temporal pulse diagnostics: One is a Michelson-type all-reflective fringe-resolved autocorrelator (FRIAC), implemented by Gebert *et al.* [36] and improved by Oliver Schepp, accessing the intensity envelope and the temporal phase by scanning and averaging many pulses; the other is the counter-propagating single-shot autocorrelator, realized by Rompotis *et al.* [28], which has been further developed in this work.

The experimental setup for the latter consists of two subsections (see Fig. 3.3): the optical setup, realizing the counter-propagating geometry, and the charged particle imaging apparatus – called *ion microscope*. A detailed explanation will follow in the next sections. But in brief, the wave-front

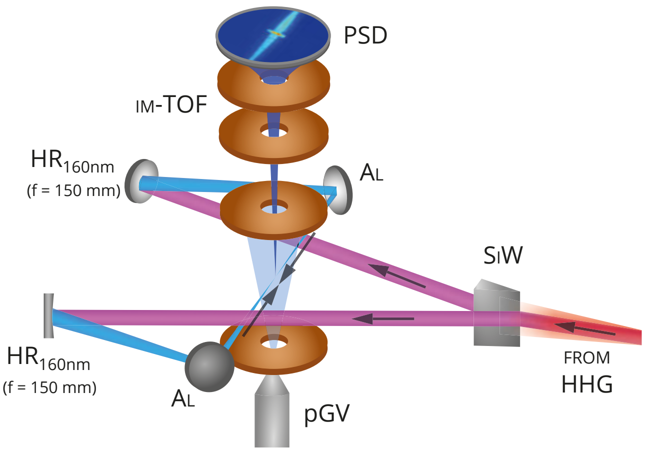

Figure 3.3– Schematic overview of the counter-propagating single-shot auto correlation experiment.

of the harmonic pulse is split by a Si wedge reflector cut at Brewster's angle for 800 nm radiation, suppressing the fundamental laser radiation and creating a pair of spatially separated VUV pulses. Each pulse follows a symmetric beam path and is spectrally purified by interchangeable dielectric focusing mirrors optimized either for the fifth or third harmonic of the Ti:Sapphire laser. Both beams are then redirected by Al-coated plane mirrors, bringing the two focused beams in a counter-propagating geometry. A pulsed gas valve provides a gaseous target in the common focal region, where the non-linear target is excited and further ionized. The photoionization products are then imaged with a time-of-flight ion microscope onto a position-sensitive detector.

Both the FRIAC and the single-shot technique complement each other. The FRIAC method benefits from the intrinsic calibration of its temporal delay axis, because the spacing between individual fringes is directly related to the central wavelength of the harmonic pulse. Furthermore, information about the temporal phase can be extracted, as has been outlined in Sec. 2.1.1. This information is lost in the counter-propagating geometry, which yields only the intensity auto correlation.

The counter-propagating technique benefits instead from its single-shot capabilities, which allows measurements addressing the shot-to-shot stability of the radiation source. Also measurements with unstable sources, such as FELs can be made feasible, since the complete delay-dependent information is encoded in each individual data set. This also dramatically reduces the acquisition time, compared to delay-stage based approaches, and higher statistical accuracy of the measurement can be achieved in shorter time, furthermore relaxing the need for long-term stability of all experimental conditions. At last, the geometry, consisting of two individual beam paths, makes it possible to change between different schemes for pump-probe experiments. Different harmonic orders generated in the harmonic source can be selected by exchanging mirrors or introducing filters in the individual branches of the experiment, enabling two-color pump-probe experiments.

3.2.1 Optical Setup

The optical geometry of the single-shot autocorrelator, see Fig. 3.4 a, is designed to adapt to the necessities of different experiments using radiation from the visible to the deep ultraviolet spectral range, provided by harmonic sources or even free-electron lasers. In combination with

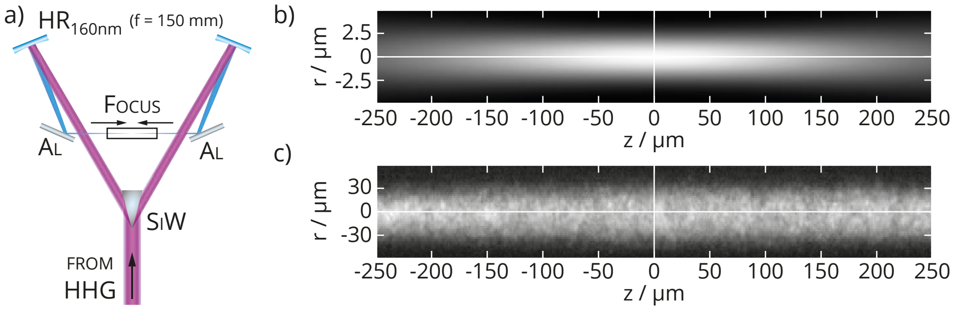

FIGURE 3.4– (a) Vertical view of the optical counter-propagating single-shot auto correlation setup. (b) Simulated spatial intensity distribution in the field-of-view of the imaging ion time-of-flight microscope for a single optical branch. (c) Microscope image of Kr$^+$ ions created by two-photon ionization from a single optical branch (300 shot average).

the harmonic source, described in Sec. 3.1.2, the Si wedge reflector (SiW) serves two purposes: Suppressing the fundamental NIR radiation by a factor of 10^{-5} (reflection in Brewster's angle), and splitting the wave-front of the incoming harmonic pulse. The thickness of the edge facing the beam is minimized by the manufacturer Pilz-Optics to assure a high quality of the individual beam halves.

Both beams follow symmetric beam paths, where they are spectrally purified. For the pump-probe experiments with the third and fifth harmonic, the first mirror is a dieletric focusing mirror (Layertec GmbH) with a focal length of 150 mm, hit at an angle-of-incidence of 2° to minimize astigmatism. The mirrors optimized for the third harmonic provide a GGD of < 20 fsec^2 and a reflectivity of 0.995 at 266 nm and 0.18 at 800 nm. The fifth harmonic mirrors provide a GGD of < 20 fsec^2 and reflect $> 92\%$ at 160 nm and less than 10% of the third harmonic and the fundamental. The reflectivity for higher harmonics is not specified. These mirrors can be easily exchanged to realize different single-color or mixed-color pump-probe schemes. Furthermore, the design allows to use broadband reflecting mirrors, such as B_4C or Mo coated optics, in combination with thin metallic filters, e. g. In or Sn, to extend the capabilities into the DUV range.

After near-normal incidence reflection each beam is redirected by VUV-enhanced Al-coated mirrors (Layertec GmbH) to create the anti-parallel geometry of both beams. The mirrors exhibit a respective reflectivity for the third and fifth harmonic of $> 80\%$ and $> 70\%$ at 45° AOI.

To achieve the goal of performing time-resolved measurements of the pulse properties and molecular reaction dynamics, matching the position of the focal planes of the pulse replicas in space and time and superimposing their wave vectors in an anti-parallel manner is necessary. A high precision is required to realize this inside the depth-of-focus of the ion microscope, which results in the alignment of eight degrees-of-freedom for the optical setup. For this purpose both focusing mirrors and one Al mirror are equipped with picomotor actuators to manipulate both angles and are placed on a motorized Gothic arch stage to achieve the temporal and spatial overlap of the foci. Furthermore, each branch of the setup is equipped with movable apertures to manipulate the intensity of each pulse to optimize the pump-probe signal, while the experiment is carried out.

Figure 3.4 shows a simulation (b) of the spatial intensity distribution of a single optical branch of the single-shot autocorrelator in comparison to an ion microscope image (c) of Kr$^+$ ions created

Figure 3.5– Schematic overview of the ion image apparatus. The apparatus is divided into three parts: (a) The ion optics part comprising the electrostatic lenses. (b) The field-free region, where ion are separated depending on mass-to-charge ratio. (c) The position sensitive detection, where the MCP/phosphor screen detector can be imaged by a CCD camera in two imaging geometries.

by two-photon ionization. Ref. [57] includes a detailed analysis of the influence of astigmatism induced by the focusing mirrors' non-zero angle-of-incidence as well as the wavefront splitting. ZEMAX simulations have been carried out for radiation of different wavelengths. For 160-nm radiation the physical optics propagation simulation exhibits a small astigmatism, but the simulated focal spot dimensions are comparable to the results of a Gaussian beam approximation, assuming half the initial beam diameter. For the simulation presented, half of the initial radius ($1/e^2$) of 4.6 mm for the full fifth harmonic beam is therefore used as an initial Gaussian beam waist. It was calculated from the estimated source size of 180 µm, the divergence of 0.45 mrad and a propagation distance of ca. 11.7 m between source and experiment [57, 58].

The result of this calculation is shown in Fig. 3.4 b. The spot size of the focus is 3.4 µm (radius at $1/e^2$) and the associated Rayleigh range is ca. 220 µm, assuming $M^2 = 1$.

The image of the ion distribution shown in the same Fig. 3.4 c, is obtained by blocking one branch of the optical setup completely and using Kr as a gas target to create Kr^+ ions by non-resonant two-photon ionization with the fifth harmonic. The lateral shape of the ion distribution is in good agreement with the assumption of a perfect Gaussian beam shape, but the radius of the ion distribution in the focal plane is larger by a factor of 10 under typical experimental conditions, where a pulsed valve is used to achieve high target densities. The broadening is reduced to a factor of 3, when the gas is supplied by a leak valve, resulting in lower target densities [57].

This indicates that the enlargement of the ion distribution is strongly affected by the target density and the stronger repulsion between the charged particles and only in part related to the quality of the harmonic beam's focus. This effect is known under the term »space charge« and is a common problem in charged particle optics. The consequences of these charged particle imaging aberrations on the temporal-spatial mapping used to acquire the delay-dependent signal from individual ion images will be discussed in Section 3.2.3.

3.2.2 Position-sensitive Detection of Charged Particles

An imaging time-of-flight ion spectrometer (*short:* ion microscope) has been designed and implemented by Dimitrios Rompotis [57] in his PhD thesis to map the distribution of charged particles created by the harmonic beam halves. The design is similar to the one of Schultze *et al.* [26].

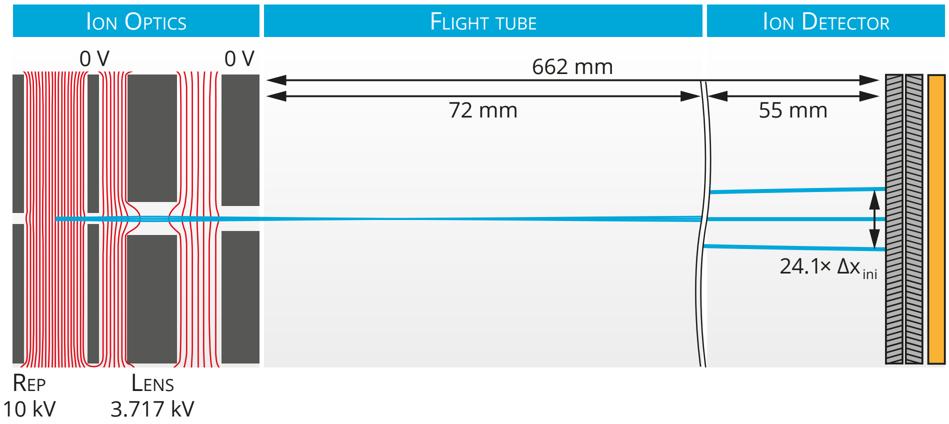

FIGURE 3.6– Simulated electrical field of the ion optics system and charged particle trajectories for Kr$^+$ ions (SIMION). Isopotential lines are spaced by 500 V. The initial lateral distance Δx_{ini} between the points of origin for the ion trajectories is ±250 µm. On the detector this distance is magnified by a factor of 24.1.

Figure 3.5 shows the design of the ion microscope, which can be divided into three sections: The ion optics, a field-free drift region and the position-sensitive detection unit. Charged particles are created from a gas target supplied by a pulsed valve (Parker Series 9 solenoid valve) and the target density is depending on the opening time of the valve, set by a Parker IOTA One valve driver. These charged particles are then guided by a set of ion optics to the detector. The first repeller electrode (REP) accelerates the ions towards the detector, while the other three electrodes form an Einzel lens assembly used to steer the charged particle trajectory achieving the time-of-flight and spatial resolution capabilites of the microscope. For this purpose a positive high voltage is applied to the repeller and the middle electrode of the Einzel lens assembly (LENS), while the two other lenses of the assembly are grounded. Afterwards the ions travel through a field-free region towards the ion detector.

The position-sensitive detection section consists of an ion detection unit and an optical imaging system. The ion detector unit is a home-built double microchannel plate (MCP) detector in a chevron geometry and an Al-coated Ce:YAG phosphor screen, which converts the charge created by ions hitting the MCP into visible light. Since the MCP is an area detector a spatial image of the ion hit positions is created. The screen is then directly imaged by an Allied Vision PIKE CCD camera equipped with a Voigtländer NOKTON 25 mm F 0.95 photography objective lens (PL_2). There are two imaging assemblies: Setup 1 uses additional close-up lenses to reduce the working distance of the objective and directly image the phosphor screen with a demagnification of 0.48, while Setup 2 employs two identical objectives in a relay imaging configuration for 1:1 imaging. The first setup provides a higher field-of-view in comparison to the 1:1 imaging option, and less imaging distortions. In the latter setup a 20:80 beam splitter (BS) is placed between both objective lenses, which redirects 20% of the light towards a photomultiplier tube recording the ion time-of-flight spectrum optically. The time-of-flight spectrum can also be acquired with the direct imaging setup by electronically decoupling high-frequency signals from the Al electrode of the phosphor screen by a passive RC high-pass filter.

FIGURE 3.7– Cut through the position-sensitive ion detector. The electron avalanche created by the impact of an ion and the spatial broadening due to the spacing between the MCPs and phosphor screen is indicated by the shaded region.

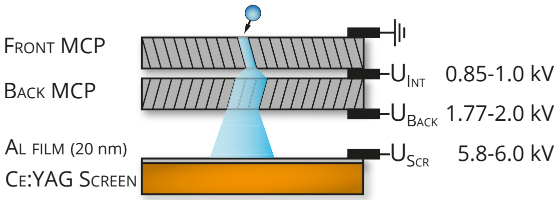

The ion imaging system has been simulated and optimized with the SIMION software originally developed by David Dahl [79]. A SIMION simulation using the actual geometry of the ion optics, flight tube and detector is shown in Figure 3.6. An optimized spatial resolution is achieved for a voltage ratio between repeller and central lens electrode of 1:0.3717. The figure shows the isopotential lines (red) with a spacing of 500 V for the typical operation voltages of $U_{REP} = 10$ kV and $U_{LENS} = 3.717$ kV, which are supplied by two high voltage power supplies (iseg Spezialelektronik GmbH), which can supply up to 20 and 10 kV, respectively.

To illustrate the magnification of the microscope the mean result of a trajectory simulation for three ensembles of 200 ions each is shown. Each ensemble is represented by a cylindrical distribution of ion origin positions, where the axis of the cylinder is in the focal plane of the ion optics and is oriented normal to the figure plane. Each cylindrical distribution has a radius of 10 μm and their axes have a lateral distance of 0 and ±250 μm relative to the central axis of the ion optics. For the simulation an initial kinetic energy of 10 meV with random orientation has been specified. For these conditions the initial lateral distance leads to a spacing of ±6025 μm on the ion detector, which corresponds to a magnification of 24.1×.

Figure 3.7 shows a scheme of the home-built position-sensitive ion detector. The microchannel plate detectors operate as an array of microscopic secondary-electron multiplier channels, achieving an amplification of 10^4 per electron created by the impact of a charged particle or high energy photon. The plates used are supplied by Photonis USA, Inc. The diameter of the active surface is 25 mm, where channels with a pore size of 10 μm, a center-to-center spacing of 12 μm and a bias angle of 8° are exposed.

To eliminate deviations of the ion trajectories near the detector the front face of the MCP stack is grounded with a ring electrode. High voltage power supplies provide stable voltages at an intermediate 100 μm thick gold-plated ring electrode (U_{INT}) between both MCP detectors, as well as at the back surface of the second MCP (U_{BACK}) connected with another ring electrode. The MCPs are typically operated with a gain voltage of 850 V per plate, achieving a total amplification of 10^7 in the chevron geometry, and an detection efficiency of ≈60% for ion impact energies of 6 keV [80]. While the chevron geometry provides a significantly higher gain compared to a single MCP, it compromises the spatial resolution of the detector. Due to the small distance between both MCPs the electron packet may spread to neighboring pores, as can be seen in Figure 3.7.

To convert created secondary electrons to light, which can be detected by the imaging system, a 500 μm thick Ce:YAG phosphor screen distanced ca. 500 μm from the MCPs is used. The screen is coated with a 20 nm thin Al film, which serves as an electrode operated at 5.8-6.0 kV, to accelerate the electrons towards the screen and minimize the spread of individual ion hit events. The Ce:YAG phosphor has been chosen for its fast luminescence decay time of 68 ns [81], rendering it possible to retrieve the time-of-flight spectrum with the photomultiplier tube of the 1:1 imaging setup.

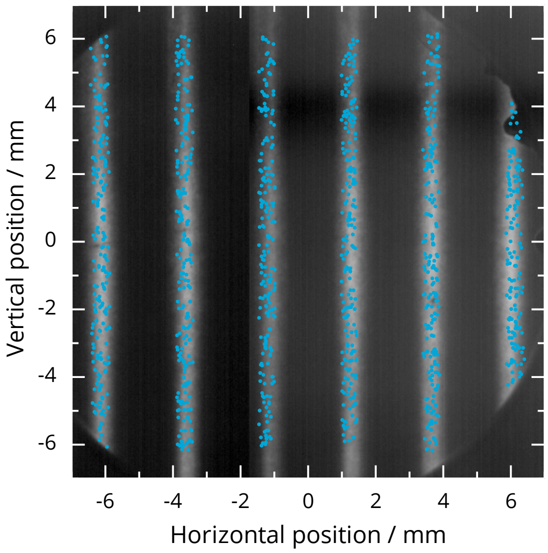

FIGURE 3.8– Simulated impact positions (blue) of ions created from evenly spaced cylinders (100 µm spacing) in comparison to a stitched camera image of a single optical branch, where the microscope is translated in 100 µm steps. Demagnification and horizontal offset of the optical imaging system is corrected in the stitched camera image.

In a typical experiment multiple species of ions are created by the VUV radiation and are imaged onto the detector. To retrieve a species-selective image the back MCP detector can be operated in a time-gated mode, where a short high-voltage is applied by a commercial MCP gating module (Photek Ltd.). The module applies a 0.5 kV pulse with a minimum pulse width of 9 ns [82], which acts as a temporal gate for the MCP gain. By these means only ion events caused by the selected species are amplified and visible on the phosphor screen.

In addition to the SIMION simulations, the magnification and imaging capabilities of the microscope can be assessed experimentally: The microscope is mounted to a XYZ manipulator for 5 µm precise positioning. By imaging the ion distribution for a single arm and translating the microscope perpendicular to the beam axis the magnification can be measured directly.

Figure 3.8 shows the result of one of these *magnification scans*, where the microscope is translated in 100 µm steps, while imaging one single optical branch. The figure uses the real length scale of the position sensitive detector, where the demagnification of the optical imaging system is corrected. The results of a SIMION simulation with the same parameters for the individual cylinders as before are superimposed onto the ion microscope image (300 shots averaged per position). Only small deviations between the simulations are visible: The horizontal offset is mainly caused by the accuracy of the manipulator, while the small curvature of the individual images stems from the combined abberations of the optical and charged particle imaging system.

The average spacing between the individual beam waists on the detector is (2.43 ± 0.18) mm, taking into account a ± 5 µm position accuracy of the manipulator and the statistical error of the measurement. The extracted magnification of $(24.3 \pm 1.8)\times$ is in good agreement to the SIMION simulation of the microscope, which yields an magnification of $24.1\times$.

The experimental verification of the magnification is carried out on a routine basis before each measurement run, since small deviations from the optimal parameters of the microscope, e. g. vertical positioning and correct voltage settings, tend to influence the imaging quality.

The vertical positioning of the microscope can be optimized by measuring the ion time-of-flight spectrum and vary the vertical position until the measured spectrum converges with the SIMION

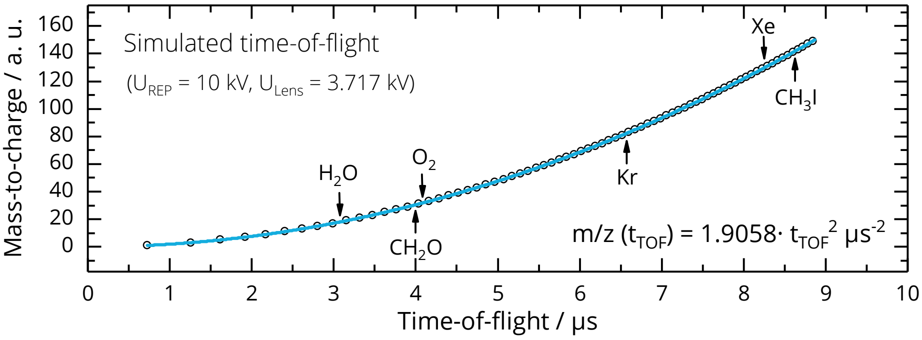

FIGURE 3.9– Simulated time-of-flight for positively charged ions. Some singly charged molecules and atoms, which have been in the focus of this work are indicated.

simulation for the time-of-flight spectrum. For this simulation an ensemble of ions originating from a sphere (10 μm diameter) centered in the intersection between focal plane and the symmetry axis of the ion microscope is used. Again, an initial kinetic energy of 10 meV with random orientation is assumed. Figure 3.9 shows the mean time-of-flight for ions with m/z 1 to 150. The species, which have been studied in various pump-probe experiments throughout this project have been highlighted.

By applying this methodology the optimal parameters for the operation of the ion microscope can be established. Afterwards the optical setup can be precisely aligned in-vacuum to achieve the spatial and temporal superposition of both pulse replicas.

To further enhance the spatial resolution of the position-sensitive detector and partly compensate the loss of resolution caused by signal broadening in the detection unit, a centroid-finding algorithm has been developed. It was implemented in conjunction with a single-shot analysis tool in the MATLAB programming environment. An introduction to image processing with MATLAB and morphological operations with images can be found in the Training Course Notebook *Image Processing with MATLAB* [83]. The algorithm is optimized to deal with noisy image data from the CCD camera and overlapping ion signals, which occur frequently due to the high count rates

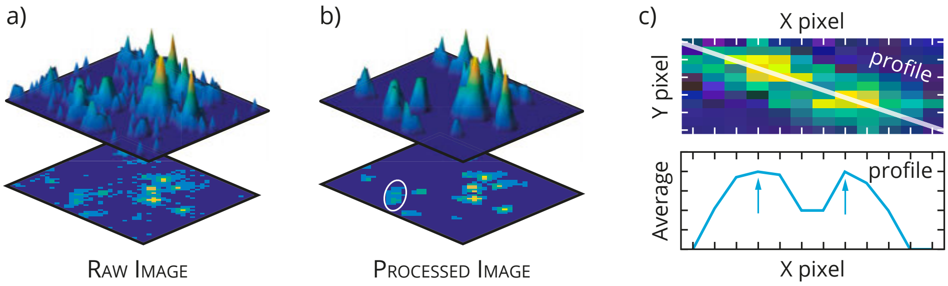

FIGURE 3.10– Ion hit positions are retrieved by a centroid finding algorithm. (a) The raw CCD image is noisy and peaks are broadened and overlapping. (b) In the processed image noise is removed. The center-of-mass of separated peaks is used to retrieve the ion hit position. (c) For non-separated peaks the profile along the white ellipsis containing one connected compound is used to separate two or more peaks.

necessary for single-shot measurements. Optimizing the spatial resolution, directly improves the temporal resolution in this experiment due to the spatio-temporal mapping performed in the colliding pulse geometry.

To illustrate the algorithm, Figure. 3.10 shows the tranformation of a raw input image (a) to a processed image (b), where individual signals are segmented and the centroid of an ion hit event is retrieved. For complicated cases, where two signals can not be distinguished by two-dimensional image operations (c), e. g. the signals highlighted by the white ellipsis, the peaks of the profile along the long axis of the connected compound are used to determine the position.

The algorithm consists of the following steps, starting from an 8 bit monochrome image of the CCD camera:

1. Remove low-intensity ($I < 1$) background signal by replacing these pixels with zero
2. Perform a morphological opening using a circle with a 1 px radius as a structuring element to remove single pixel noise signals
3. Rescale the intensity of the image to maximum range ($I \in [0, 256)$) and compute the complement of the image
4. Perform a morphological erosion using a circle with a 2 px radius as a structuring element to improve the segmentation of overlapping signals
5. Apply a watershed transformation to the image to compute a segmented binary image and find the connected components (connectivity = 8) in the image

At this point a set of statistical quantities of all connected components is calculated to further classify them and distinguish between components, which belong to a single ion signal and others, which are caused by overlapping signals. Most important for this classification is the area A_i of one connected component i and its shape, specified by the ratio between the horizontal and vertical dimension l_i^x / l_i^y:

$$a_i \equiv [A_i < (\mu_A + \sigma_A)] \wedge \left(\frac{2}{3} < \frac{l_i^x}{l_i^y} < \frac{3}{2} \right) . \tag{3.2}$$

Equation 3.2 is true, when the area A_i of the signal is smaller than the mean area of all components plus its standard deviation, and when the ratio between l_i^x / l_i^y of the component is between 2:3 and 3:2. The component is then classified as a single ion event, in the other case the component most likely consists still of two or more ion signals:

$$a_i \rightarrow \text{Single ion event} \tag{3.3}$$

$$\overline{a_i} \rightarrow \text{Overlapping events} \tag{3.4}$$

For a single ion event the central position is retrieved by calculating the center-of-mass from the part of the original image, which is comprised by the connected component. In the other case a peak-finding routine is applied to the profile of the connected component, which follows the

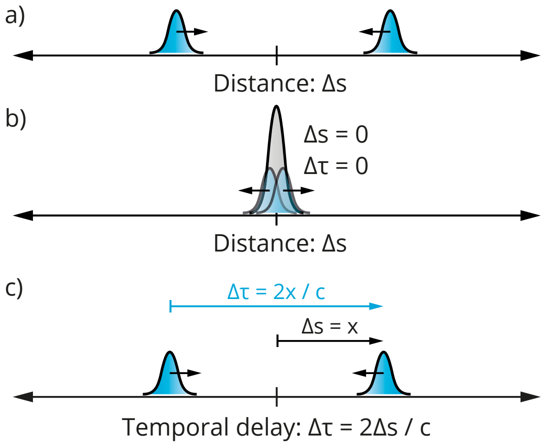

FIGURE 3.11– Delay encoding principle. (a) Two pulses are counter-propagating along an axis s. (b) The meeting point in time and space ($\Delta s = \Delta\tau = 0$) defines the temporal overlap at zero delay. (c) For a given distance Δs from the temporal overlap the optical path length difference between both pulses is double this distance.

major axis of an elliptical approximation of the component. The centroids of the individual signals are then given by the x and y position of the retrieved peaks.

In the design and test phase of this algorithm great care was taken to adapt to different experimental conditions, which influence the shape, intensity and spacing of individual signals in the CCD image. Using the statistical quantities extracted from a single image or a series of images from the same experimental run, strongly improves the robustness and reliability of the centroid retrieval. Still, for new experimental conditions, for example changes in the optical imaging system, the algorithm needs to be tested and the structuring elements of the morphological operations need to be optimized.

As an additional effect, deterioration of the charged particle detection is counteracted. Throughout their lifetime the conversion efficiency of MCP detectors is decreasing, when a detector pore has been exposed over a long period of time to radiation or charged particles. Consequently, the detection efficiency is not constant over the surface of the detector anymore and the intensity profile becomes distorted. Thus, the use of centroid retrieval improves not only spatial resolution and temporal resolution of the pump-probe experiment, but also relaxes the quality demands towards the detection unit.

3.2.3 TEMPORAL CHARACTERIZATION OF ULTRAFAST PULSES

In a single-shot experiment the transformation from the spatial domain to the temporal domain is the key point in extracting delay-dependent data from a single image, in this case the retrieved ion images. In the counter-propagating geometry the delay encoding is straight-forward: Both pulses are propagating at the vacuum speed of light on the same axis in an anti-parallel direction, as depicted in Figure 3.11 a. At any given point in time the distance between each pulse and the origin is given by $|\Delta s|$. The origin of the axis is the meeting point of both pulses in space in time: the point of zero delay (b), where the auto correlation signal (shown in gray) of both pulses emerges. Here $\Delta s = \Delta\tau = 0$, where $\Delta\tau(\Delta s)$ is the delay between both pulses as a function of the spatial distance from the origin. Since both pulses are traveling at the speed of light c for any distance Δs the temporal delay is given by

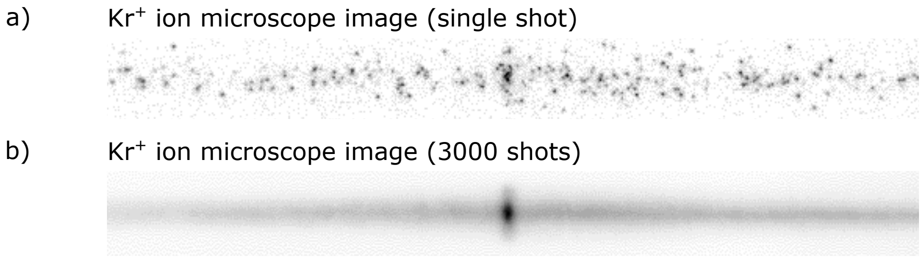

FIGURE 3.12– Microscope images of Kr$^+$ ions created from two-photon ionization by counter-propagating pulses. (a) Ion image from a single laser shot. (b) Averaged ion images from 3000 shots.

$$\Delta\tau = 2\frac{\Delta s}{c}. \tag{3.5}$$

In Figure. 3.11 c this relation is apparent: For a displacement of $\Delta s = x$ for one pulse replica, the other one is displaced by $\Delta s = -x$ and the optical path length difference thus is $\Delta\tau = 2x/c$.

Of course this relation only holds for propagation in vacuum and a perfect anti-parallel orientation of both beams. When this is not the case, the linear refractive index of the medium and the angle between both pulse fronts needs to be considered.

To directly perform the transformation into the time domain from the ion microscope images Equation 3.5 needs to be extended by the magnification factor of the microscope, the demagnification of the optical image system and the specifications of the CCD sensor:

$$\Delta s = \frac{\Delta x \cdot d_{\text{px}} \cdot F_{\text{bin}}}{M_{\text{IM}} \cdot M_{\text{opt}}}. \tag{3.6}$$

Here Δx is the distance in pixels from the point of zero delay, d_{px} the CCD pixel size of 7.4 µm, F_{bin} the binning factor used for the camera acquisition, signifying the amount of CCD pixels, which are combined into one image pixel. M_{IM} and M_{opt} are the respective magnification of the ion microscope and optical imaging setup.

In the experiment the ion microscope is used as an alignment tool to achieve the anti-parallel superposition of both wave vectors, so the temporal properties of the fifth harmonic pulses can be extracted by the means of single-shot auto correlation. For this purpose noble gases, such as krypton or xenon are used as a non-linear target, since their respective ionization energies ($\text{IE}_{\text{Kr}} = 14.00$ eV, $\text{IE}_{\text{Xe}} = 12.13$ eV) are exceeded by the simultaneous absorption of two photons with a photon energy of 7.70 eV. For 7.70-eV radiation no intermediate resonances, such as long-lived Rydberg states, exist and the resulting delay-dependent signal is related only to the temporal properties of the VUV pulses.

Figure 3.12 a shows an exemplary Kr$^+$ single-shot ion microscope image, as retrieved from the CCD camera. Individual ion signals are visible, which are distributed along the horizontal propagation axis of the overlapping beams. The region in the center of the image, with an increased signal density, signifies the temporal overlap between both beams. The auto correlation trace of the pulse can be extracted from this single-shot image, but the accuracy is increased by averaging

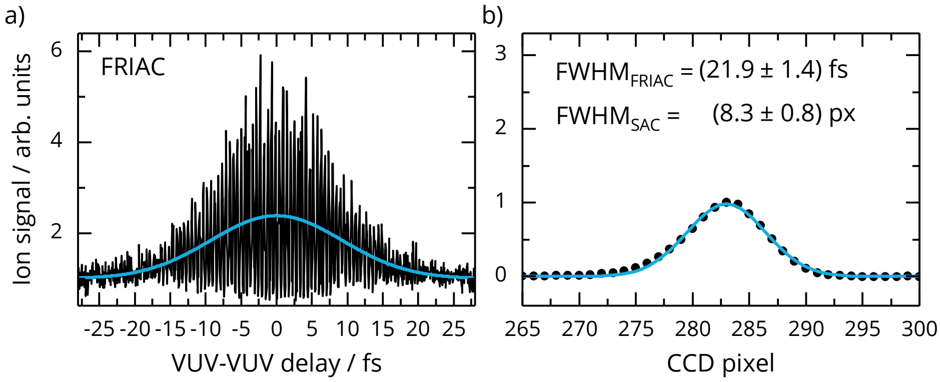

FIGURE 3.13– Delay-dependent two-photon ionization of Kr measured with the fringe-resolved auto correlation technique and the single-shot autocorrelator in direct sequence. (a) The interferometric signal is shown in black, and the Gaussian fit on the low-pass filtered data in blue. (b) The single-shot data points are shown in black and the corresponding Gaussian fit in blue.

multiple images. Such an averaged image is shown in Figure 3.12 b. Here both the lateral profile of the common focus and the delay-dependent feature in the center are clearly visible.

Under ideal conditions Equation 3.6 can now be used to transform the horizontal image coordinate into the temporal domain. But one has to remember that the image used to retrieve delay-dependent information stems from charged particles and not photons. The repulsion between these particles introduces additional challenges for spatial imaging, which have already been implied in the previous section.

Rompotis [57] demonstrated in his PhD thesis, that the ion microscope suffers from imaging aberrations, caused partly by space charge effects (see the comparison between the simulated and imaged beam waist in Fig. 3.4) and furthermore by intrinsic aberrations of the apparatus. A discrepancy between the global magnification of the ion microscope, which has been simulated and validated experimentally, and the magnification factor used for the delay encoding was revealed. For a given optical imaging setup, CCD binning and post-evaluation (centroid-finding) these parameters do not dependent on the target gas species, charge state and charged particle density.

Consequently, the magnification mismatch can be treated by applying a calibration factor and the validity of the measurements is not compromised. For these means, a cross-reference benchmark measurement is conducted, measuring the auto correlation of the fifth harmonic pulses, generated by the tuneable-length harmonic sources, both in the single-shot autocorrelator, as well as the fringe-resolved experiment, which is described in detail in References [36] and [58]. Both experiments utilize the same radiation, but independent measurement principles, to acquire the same quantity – the pulse duration.

In the chapter »Theoretical Background« section 2.1.1 lays out the basic principle of fringe-resolved intensity auto correlation (FRIAC). The cross-reference measurement benefits from the intrinsic calibration of the FRIAC method, where the fringe spacing can be ascribed to the known carrier wave frequency ω of the pulse.

Figure 3.13 shows a comparison between a FRIAC measurement and a measurement with the single-shot autocorrelator in direct sequence, with Kr as a non-linear ionization target. From

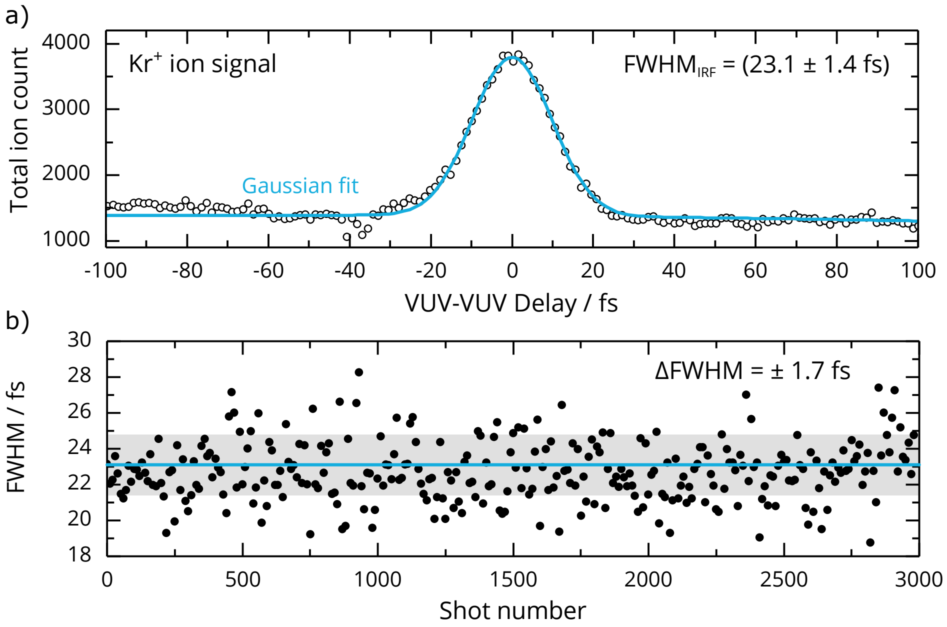

FIGURE 3.14– (a) Delay-dependent Kr^+ ion yield extracted by the centroid-finding algorithm from the single-shot images of Fig. 3.12. (b) FWHM of the Gaussian instrument response function for groups of 10 shots. The blue line depicts the average FWHM and the gray box refers to the root mean square deviation.

the FRIAC experiment (a) a FWHM of the intensity auto correlation function of (21.9 ± 1.4) fs, which is extracted by low-pass filtering the interferometric auto correlation trace. This result is then used as a reference to calculate the conversion factor from CCD pixel to delay scale in the single-shot experiment. The FWHM of (8.3 ± 0.8) px is referenced to the FWHM of the intensity auto correlation function. With Equations 3.5 and 3.6 this results in an calibration factor of 2.8 for this measurement run. Consequently, the associated delay range covered in the image is approximately ±500 fs, with a distance between adjacent data points of 1.3 fs without CCD camera binning. This calibration measurement is repeated, when the imaging conditions are varied and can also be validated by measuring well-known ionization dynamics of molecules, such as molecular oxygen [60].

As soon as the delay scale calibration is established, the single-shot autocorrelator can complement the FRIAC technique in multiple ways. While both techniques can be used to measure the intensity auto correlation function of the pulse, which is shown in Fig. 3.14 (a), the single-shot approach enables access to the stability of the pulse duration and intensity of the harmonic pulses.

The shown trace is derived from the average Kr^+ ion images shown in Fig. 3.12 (b). When a Gaussian pulse shape is assumed an intensity auto correlation with a FWHM of (23.1 ± 1.4) fs can be fitted to the experimental data set, where the error is mainly ascribed to the accuracy of the space-time-mapping. In a pump-probe experiment this is equal to the instrument response function (IRF), which is the determining factor limiting the temporal delay resolution.

A precise measurement of the average IRF and its shot-to-shot fluctuations is the key to elucidate molecular dynamics, which take place on the same time scale as the duration of the pulses. In this case a pulse duration of (16.3 ± 1.0) fs is extracted by deconvolution from the IRF for a Gaussian pulse with a deconvolution factor of $\sqrt{2}$ (see Sec. 2.1.1).

When the full data set is analyzed shot per shot, an IRF for each shot can be retrieved. Figure 3.14 b shows the results of this analysis. The chosen measurement conditions were already adapted to a pump-probe measurement in the same run, requiring lower ion count rates. To minimize the errors introduced in the fit procedure, ten shots were averaged beforehand, as a compromise between fitting robustly and averaging the minimum amount of data sets.

The data is shown as a scatter plot with ascending shot number. The horizontal line in the image shows the average FWHM of the IRF, with the root mean square deviation of ± 1.7 fs as a gray box. In the time of the measurement run no drift of the FWHM is observed, confirming the long-term stability of the pulse duration. The calculated root mean square deviation is comparable to the statistical accuracy of the FWHM of the IRF, calculated from the averaged ion image (Fig. 3.14 a). This signifies also a high shot-to-shot stability.

The data set used to perform this analysis has been acquired in 3000 shots at a laser repetition rate of 25 Hz, which results in a total measurement time of only two minutes. Compared to conventional pump-probe spectroscopy, which relies on a delay stage to introduce a temporal delay between pump and probe pulse, a high statistical accuracy is reached in a small amount of time, without reducing the temporal delay range. On the one hand, this relaxes the long-term stability demands of an experiment: Pulse energy, beam pointing, target density and temperature need to be in a steady state only for minutes and not for hours of measuring time. On the other hand, the saved time contingent can be reinvested: A multivariate study, e. g. a parametric study depending on pulse energy and target density, or a comparative study between a homologous series of chemical compounds, can be conducted in a feasible amount of time.

In this chapter the experimental prerequisites to perform pump-probe experiments in the vacuum ultraviolet regime and record the data in a single-shot based approach with few-fs temporal resolution have been presented. Intense 7.70-eV (161-nm) and 4.62-eV (268-nm) radiation is obtained by harmonic generation in a argon gas target, benefiting from the intrinsic shortening of the pulse duration compared to the fundamental pulse in the perturbative regime of high-order harmonic generation. The main apparatus, a single-shot auto correlation and pump-probe experiment, has been introduced with a focus on the spatial delay encoding, facilitated by an imaging ion time-of-flight spectrometer, and the evaluation of the retrieved ion microscope images. The capabilities of the apparatus have been demonstrated by extracting the intensity auto correlation of 7.70-eV pulses from the delay-dependent measurement. The temporal stability of VUV pulses supplied by the harmonic source could be discerned by single-shot pulse metrology utilizing two-photon ionization of krypton.

4

PUMP-PROBE EXPERIMENTS

The following chapter presents how the ultrashort and intense (V)UV pulses are used in pump-probe experiments, which focus on different advantages available to a single-shot technique relying on imaging of a spatial ion distribution.

First the sub-10-fs dissociation dynamics of water and its isotopologues after excitation in the VUV will be discussed. The dissociation of the ubiquitous water molecule in its first absorption state proves as a perfect prototype to illustrate the temporal-resolution of the single-shot technique and address fundamental questions on how to treat the early stage of rapid dissociation dynamics in pump-probe experiments [61]. Next, experiments with the ultrashort third harmonic pulses are presented. These deal with the temporal characterization of these pulses by auto correlation in noble gases and cross correlation with the VUV pulses. With pulses energy of up to 20 µJ intensity-dependent studies are realized with krypton and xenon atoms, utilizing the spatial information of the ion microscope to full extent. The chapter will close with applications of two-color experiments utilizing both harmonic pulses as exchangeable pump and probe pulses in a simultaneous experiment. The competition between low-lying valence excitations and high-lying Rydberg states as initiator for reaction dynamics of iodomethane is discussed.

4.1 VUV PHOTODISSOCIATION OF WATER AND ITS ISOTOPOLOGUES

The VUV-induced photodissociation reaction of water via the first excited state ($\tilde{A}\,^1B_1$) has been the subject of an abundance of theoretical and experimental studies, as a prototype for a repulsive, barrierless, adiabatic dissociation reaction. The contents of this section have been published previously in the journal *Physical Review A* [61].

The potential energy surface [84, 85] of the first excited state has been calculated with high precision by Staemmler & Palma [84]. This is a widely utilized calculation and has been further improved by different groups [86–88]. Based on these calculations previous theoretical studies focused on the interpretation of the $\tilde{A}\,^1B_1$ absorption spectrum [89–92], as well as on the rotational fine-structure of the dissociation products [93]. These calculations are supported by a multitude

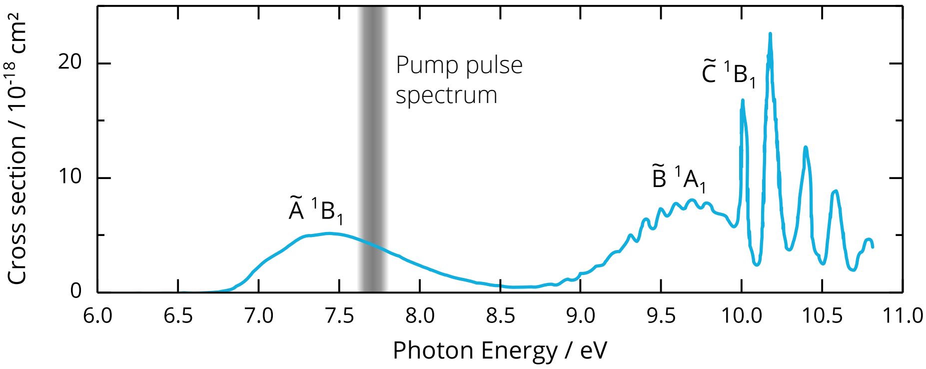

FIGURE 4.1– Photo-absorption spectrum of H_2O in the vacuum ultraviolet range. The pump pulse excites the molecule into the first excited electronic state $\tilde{A}\,^1B_1$. Reproduced from Ref. [94].

of experiments, such as high precision absorption spectroscopy [94], Rydberg-tagging experiments [95, 96], photoemission spectroscopy [97] or studies of isotope effects on the dissociation dynamics [89, 98–102].

The photodissociation dynamics of H_2O and its deuterated isotopologues in the first excited state are an excellent opportunity to demonstrate the capabilities of the single-shot VUV pump/probe approach. It is possible to disclose sub-10-fs photodissociation dynamics, while greatly reducing acquisition time by collecting complete pump-probe data sets at the repetition rate of the laser system, resulting in exceptional statistic accuracy compared to typical delay-stage based pump-probe experiments.

The VUV pump/probe approach complements previous studies relying on multi-photon ionization in the probe step, where a sufficiently high infrared field strength is needed. These strong fields may influence the molecular potentials [103] and affect the intrinsic molecular dynamics. In a weak-field approach these effects, as well as the influence of intermediate states, which might be accessed resonantly in the probe step, are excluded, allowing a simplified theoretical description of the experimental observables for the molecular dynamics.

4.1.1 BACKGROUND

The absorption spectrum of water below 11.0 eV (Fig. 4.1) consists of three valence excitations: The broad, nearly featureless absorption band between 6.5–9.0 eV belonging to the $\tilde{A}\,^1B_1$ excitation, another broad feature with vibrational structure, the $\tilde{B}\,^1A_1$ state between 8.5–10.0 eV, as well as a relatively small feature from the $\tilde{C}\,^1B_1$ state, which is superimposed by a series of sharp Rydberg peaks [94, 104]. Both the $\tilde{A}$ and $\tilde{B}$ absorption states are dissociative along the asymmetric HO−H stretch vibration, resulting in a broad absorption spectrum.

The fifth harmonic radiation used in the experiment resonantly excites the $\tilde{A}\,^1B_1$ state, which then undergoes a rapid dissociation:

$$\mathrm{H_2O}\ (\tilde{X}\,^1A_1)\ \xrightarrow[161\ \mathrm{nm}]{\hbar\omega}\ \mathrm{H_2O^*}\ (\tilde{A}\,^1A_1)\ \longrightarrow\ \mathrm{H}\ (^2S)\ +\ \mathrm{OH}\ (^2\Pi, \nu = n).$$

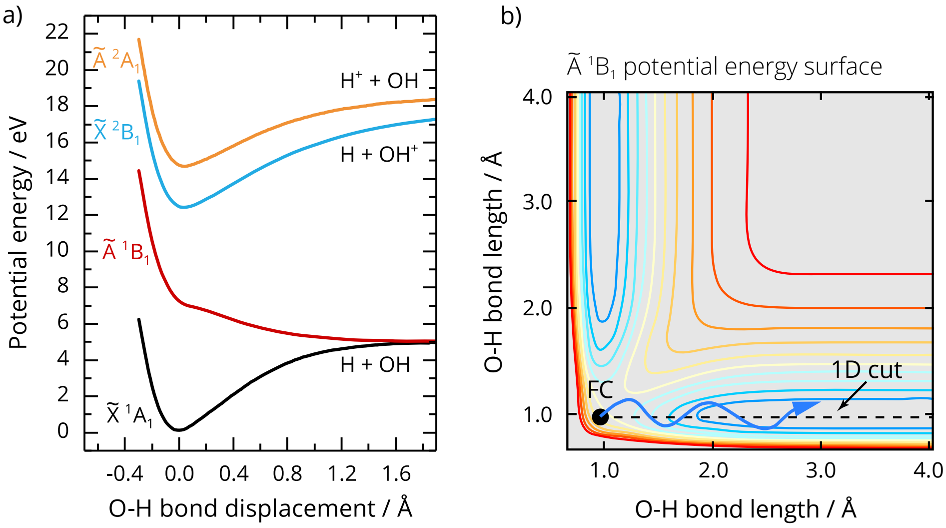

FIGURE 4.2– Potential energy curves of the first molecular and ionic states of water along the HO−H bond axis (a) and two-dimensional representation of the molecular $\tilde{A}\ ^1B_1$ excited state (b, reproduced from Ref. [92]). In b the one trajectory for a wave packet launched in the Franck-Condon zone (FC) is indicated.

Since no other states are coupled non-adiabatically to this state, this is a rare example for an adiabatic, barrierless dissociation reaction and the effects of the dissociation dynamics on the absorption spectrum has been studied by different theory groups [85, 90–92]. It has to be highlighted here, that the faint modulation visible in the first absorption band is not due to the vibrational progression in the $\tilde{A}\ ^1B_1$ state. In the Franck-Condon region an excitation of the vibrational ground state is dominant [85]. The structure is closely linked to the correlation function $\langle\phi_i|\phi_i(\tau)\rangle$, where ϕ_i is the initial wave function of a wave packet after excitation and $\phi_i(\tau)$ is the same wave function after a delay τ. This correlation function shows small recurrences, where a fraction of the wave packet is returning to the Franck-Condon region, caused by oscillation in the symmetric stretch vibration, while the molecule is dissociating [90]. The finite 'life time' of the symmetric stretch vibration of approximately 8 fs is directly linked to the delay-dependent signal observed in a pump-probe experiment.

Figure 4.2 presents an overview of the molecular and ionic states relevant in the pump-probe experiment. The key reaction coordinate is the asymmetric stretch vibration and a cut along this coordinate is shown in Fig. 4.2 a. After an initial excitation from the $\tilde{X}\ ^1A_1$ ground state to the $\tilde{A}\ ^1B_1$ excited state, the molecule will be interrogated by delay-dependent ionization. For the ionization probe the shape of the ionic ground ($\tilde{X}\ ^2B_1$) and first electronic excited state $\tilde{A}\ ^2A_1$ will be considered later.

As discussed for the absorption spectrum, oscillation of the symmetric stretch vibration must not be neglected in the analysis of the dynamics. Rydberg-tagging experiments [95] show a vibrational state distribution for the OH product, where vibrational states up to $\nu = 4$ are observed. In Fig. 4.2 b an exemplary trajectory is depicted, emphasizing the contributions of the symmetric stretch vibration after the molecule leaves the Franck-Condon region. Since the potential gradient is steepest for elongation of both OH bonds the wave packet starts moving in the direction of the symmetric stretch vibration first, before it follows the potential gradient along one of the equivalent HO−H bond coordinates. Consequently, not only the elongation of a single OH bond needs to be considered, in the analysis of the pump-probe experiment.

Previous experiments either were unable to fully resolve the early reaction dynamics and only reported an upper limit of 20 fs [105, 106], or reported a very short time constant, defining the time the molecular wave-packet needs to exit the Franck-Condon region (1.8 fs) [107]. The first group used a similar single-color VUV pump-probe approach, while the latter relied on multi-photon ionization for probing the reaction dynamics involving strong fields. In addition to these experimental studies Imre & Zhang [91], as well as Henriksen *et al.* [90] deduced the time a wave packet created by vertical excitation of the $\tilde{A}\,^1B_1$ state needs to leave the Franck-Condon region is 5 fs. To address the discrepancy between these results, a weak-field single-color approach with a time-resolution discerning sub-10-fs dissociation dynamics is an ideal tool.

4.1.2 EXPERIMENT

The experimental setup has been discussed in detail in the previous chapter. Here fifth harmonic pulses at 161.0 nm (7.7 eV) are used as pump and probe pulse in both arms of the colliding-pulse setup. The dissociation dynamics of the isotopologue series H_2O, HDO and D_2O are studied to further enhance the significance of the results by using the kinetic isotope shift as an indicator.

Non resonant two-photon ionization of Kr was used for single-shot intensity auto correlation measurements in order to experimentally determine the instrument response function, as presented in Sec. 3.2.3. H_2O and D_2O were supplied from the heated vapor of pure liquids, while HDO was supplied from the vapor of a mixture of both. By applying a backing pressure of less than 200 mbar the formation of water dimers or clusters could be excluded, verified by ion time-of-flight spectrometry.

Single-shot data has been evaluated with the centroid-retrieval algorithm presented in the previous chapter. The background created by two-photon ionization by the pump or probe pulse alone, which is a broad Gaussian in the Rayleigh range of the common focus, has been approximated by a spline and subtracted.

The data presented here is exemplary for a series of more than 100 individual measurements consisting of 1000-5000 full pump-probe data sets each, which have been acquired in the course of six months (see Appendix A.1.1).

4.1.3 COMPUTATION

The interpretation of the delay-dependent dynamics of the water isotopologues is supported by a mixed quantum-classical approach to calculate not only the molecular trajectories in the dissociative $\tilde{A}\,^1B_1$ state, but also investigate the influence of different final electronic states, accessible by photoionization with a single probe photon, on the observed delay-dependent ion yield. Vertical excitation energies and photoionization cross sections along the reaction coordinate have been calculated by Sophia Bazzi and Daria Gorelova from the groups of Oriol Vendrell and Robin Santra. These result in the delay-dependence of the vertical ionization energy from the $\tilde{A}\,^1B_1$ state to the electronic ground and first excited states of the ion for an evolving wave-packet, which is pivotal in the interpretation of the pump-probe experiment.

The nuclear motions were treated classically by Newton's equations of motion and the electrons were described quantum mechanically. Since the molecules are sufficiently cold in the experiment, the nuclear coordinates and momenta were sampled from the harmonic Wigner distribution [108] for the ground vibrational level of the $\tilde{X}\ ^1A_1$ electronic ground state, in which the zero-point vibrational energy is given to each normal mode. It is also assumed that all water molecules are initially in the rotational ground state. In this way initial conditions for 20 classical trajectories on the $\tilde{A}\ ^1B_1$ potential energy surface were obtained. The trajectories were then divided into two subsets of ten trajectories. Similar temporal evolution of the two subsets confirmed sufficiently good statistics. For each trajectory 0.1 fs time steps were used for the numerical integration of Newton's equations using the velocity Verlet algorithm [109]. Supplementing classical trajectory simulations on the two-dimensional potential energy surface shown in Fig. 4.2 b have been performed by the author yielding comparable results. The simulation results are presented in appendix A.1.2.

On-the-fly ab-initio calculations of the electronic structure, including the gradients, were done with the complete active space self-consistent field method using six active electrons in four active orbitals, CASSCF(6,4), and the augmented double-ζ basis set, aug-cc-pVDZ [110, 111] utilizing the MOLCAS program package [112]. The energies were reevaluated with single point calculations at the multi-reference single and doubles configuration-interaction level with eight correlated electrons and seven active orbitals, MR-CISD (8,7), and the aug-cc-pVDZ basis set. Both CASSCF and MR-CISD were employed because only CASSCF allows one to compute gradients analytically within MOLCAS, which is optimal for calculating chemical trajectories, whereas MR-CISD provides higher accuracy for ionization energies.

The time windows in which the neutral molecule can be ionized to the electronic ground and first excited states of the cation with a single photon of 7.7 eV energy are obtained by averaging over 20 trajectories. Outside these time windows, the geometry is so far distorted in comparison to the equilibrium geometry that the cation could no longer be created with a single photon of 7.7 eV energy.

Photoionization cross sections $\sigma(\tilde{X}\ ^2B_1)$ and $\sigma(\tilde{A}\ ^2A_1)$ were calculated for 7.7-eV photon energy as a function of the molecular geometry, applying the orthogonalized plane-wave approximation to the photoelectron wave function [113]. At each molecular geometry the MR-CISD(8,7) wave function for the $\tilde{A}\ ^1B_1$ state and the MR-CISD(7,7) wave functions for the $\tilde{X}\ ^2B_1$ and $\tilde{A}\ ^2A_1$ states were used for these calculations. Additional details about the calculation are stated in Ref. [61].

4.1.4 RESULTS & DISCUSSION

The delay-dependent ion yield for H_2O and its isotopologues is determined by the internal dynamics of the molecule convoluted with the instrument response function of the experiment. The instrument response function has been measured using two-photon ionization of krypton resulting in the auto correlation of the VUV pulse. The resulting function is a Gaussian with a FWHM of (23.1 ± 1.4) fs (details are presented in Sec. 3.2.3).

Figure 4.3 shows an one-dimensional cut through the potential energy surfaces, which are relevant for this pump-probe experiment. The potential energy surfaces have been calculated by Sophia Bazzi at MR-CISD(8,7) and MR-CISD(7,7) level for H_2O and H_2O^+, respectively. In the

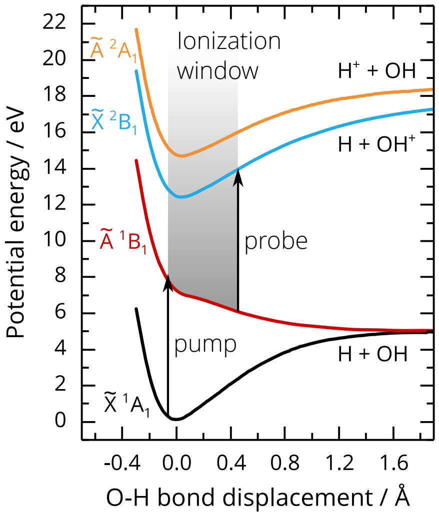

FIGURE 4.3– Excitation scheme of the VUV pump-probe experiment for H_2O. Both energetically accessible final ionic states are shown and the ground state ionization window is highlighted.

excitation scheme employed in this pump-probe experiment the first VUV photon (7.7 eV) excites the molecule from its electronic ground state (black) into the $\tilde{A}\,^1B_1$ state (red). Since this state is unbound in the direction of the asymmetric stretch vibration, the molecule starts to dissociate. Not only the bond distance of the dissociating bond shown in Fig. 4.3 is changing during this dissociation reaction, but also the HOH angle and the second O-H bond distance are changing and have been taking into account in the calculation. Due to the increasing energy difference between the excited $\tilde{A}\,^1B_1$ state and the electronic ground state of the H_2O^+ ion (blue), as well as the first excited state (orange), the observation of the dissociation dynamics is confined to a limited time range. Thus, the time when the molecular structure is distorted such that a single VUV probe photon cannot ionize the molecule anymore [114] (depicted as the gray ionization window in Fig. 4.3) is clocked precisely.

The duration of the ionization window can be extracted from the trajectory calculations for each isotopologue. Hence, the vertical excitation energies for the transition from the molecular $\tilde{A}\,^1B_1$ state to the electronic ground state and to the first excited state of the ion are calculated for the evolving molecular coordinates after each time step. Figure 4.4 shows the time evolution of the vertical excitation energies for (a) H_2O, (b) HDO and (c) D_2O, as well as the photon energy of the probe pulse as a reference. As soon as the excitation energy for each transition exceeds the probe photon energy, the ionization window for the respective excitation scheme closes. The shortest window for ionization to the ground cationic state τ_X corresponds to H_2O and is 6.4 fs, increasing to 8.2 fs for HDO, due to the higher mass of the fragment. D_2O exhibits the longest time window of 9.4 fs.

The corresponding ionization window for a probe transition to the first electronically excited state of H_2O^+ and its deuterated derivatives is much shorter than the time window for ionization to their ground electronic state. Depending on the ratio between their respective photoionization cross sections, both probe transitions may contribute to the experimentally observed ionization window. The longest ionization window is observed, if the photoionization cross section σ for the $\tilde{X}\,^2B_1$ channel is much larger than $\sigma(\tilde{A}\,^2A_1)$. On the other hand, the apparent ionization window

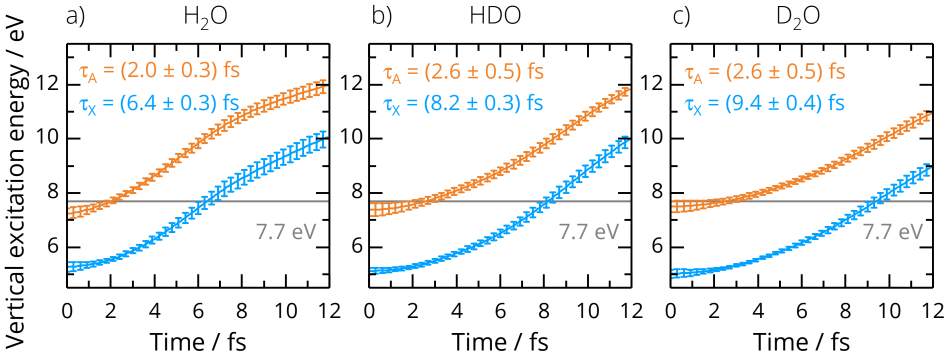

FIGURE 4.4– Calculated time evolution of the vertical excitation energy from the Ã ^{1}B$_1$ state to the X̃ ^{2}B$_1$ state (blue) and from the Ã ^{1}B$_1$ state to the Ã ^{2}A$_1$ state (orange) during the dissociation for (a) H_2O, (b) HDO, and (c) D_2O and the corresponding time windows in which ionization from Ã ^{1}B$_1$ to X̃ ^{2}B$_1$ (τ_X) and Ã ^{2}A$_1$ (τ_A) with a single photon of 7.7 eV energy (gray line) is possible. The error bars represent the root mean square width of the energy distribution for a given time.

gets shorter as the ratio $\sigma(\tilde{A}\ ^2A_1)/\sigma(\tilde{X}\ ^2B_1)$ increases. It should be noted that, even at distances where ionization is still possible, σ is not necessarily constant.

According to the calculations, $\sigma(\tilde{A}\ ^2A_1)$ is negligible in comparison to $\sigma(\tilde{X}\ ^2B_1)$ at all molecular geometries where ionization to both states is possible. Thus, the photoionization time windows are determined exclusively by the vertical excitation energy from the $\tilde{A}\ ^1B_1$ to the $\tilde{X}\ ^2B_1$ potential energy surface in the employed single-photon probe scheme. For a given pump photon energy the time evolution shown in Fig. 4.3 is universal and the $\tilde{A}\ ^2A_1$ state of the ion will be relevant for a multi-photon probe scheme.

An overview of averaged ion images retrieved for Kr, as well as the water isotopologue series are presented in Fig. 4.5. The total delay range accessible in the single-shot experiment is indicated, although the pump-probe signal is very sharp and limited to a delay range of ±40 fs. Already in the images broadening of the pump-probe signal compared to the non-resonant two-photon signal in krypton is visible. Also, the FWHM of the signal is increased for a higher degree of deuterization.

The experimentally obtained pump-probe signal for H_2O and its deuterated derivatives is equal to the distribution of ion signals along the propagation axis of the beams after conversion from space to delay. It is similar to the vertical binning of the ion images shown and determined by the convolution of the instrument response function and the dynamics of the respective molecule.

To deconvolve the dynamics from the experimental data sets, where the instrument response function is on the same time scale as the expected ionization window, an appropriate fit function needs to be applied. As has been shown in the trajectory simulations, the first trajectories start leaving the ionization window after more than 5 fs and up until this time the population in the ionization window stays constant. This behavior can be modeled by a rectangular function, where the duration of the ionization window is given by its half-width. The convolution of this function and the instrument response function, fitted with a Gaussian, is given by

$$I(\Delta t) = a \cdot \left[\operatorname{erf}\left(\frac{\tau_{1/2} - \Delta t}{\sqrt{2}\sigma_p} \right) + \operatorname{erf}\left(\frac{\tau_{1/2} + \Delta t}{\sqrt{2}\sigma_p} \right) \right]. \tag{4.1}$$

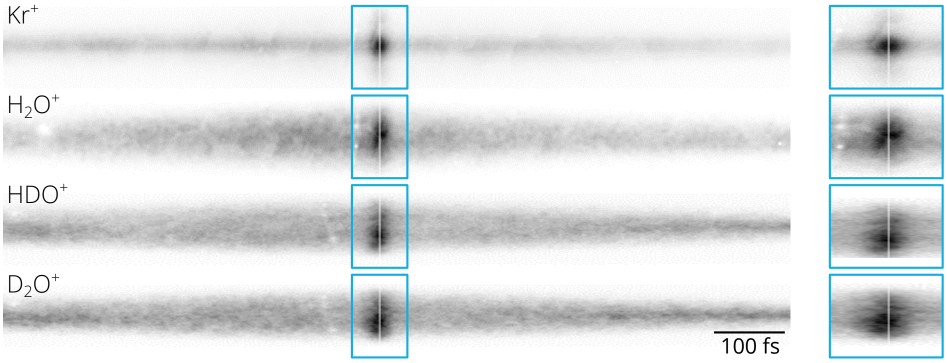

FIGURE 4.5– Averaged ion microscope images of Kr⁺ and the series of water isotopologues. A white line indicates the point of zero delay in each image. The region containing the delay-dependent feature is magnified by each image to emphasize the increasing broadening from top to bottom.

Here Δt is the delay between pump and probe pulse and σ_p is the standard deviation of the instrument response function ($\sigma_p = \mathrm{FWHM}/(2\sqrt{2\ln 2})$), while $\tau_{1/2}$, the half-width of the rectangular function, and the scaling factor a are the free fit parameters.

For H_2O, with a corresponding FWHM of (22.3 ± 1.3) fs for the instrument response function, the fit yields $\tau_{1/2} = (6.7 \pm 1.8)$ fs (Fig. 4.6). For HDO a slightly narrower instrument FWHM of (21.4 ± 1.3) fs for the instrument response function, results in $\tau_{1/2} = (7.5 \pm 1.7)$ fs. The internal dynamics in D_2O are proceeding slower, which leads to a stronger deviation from the intensity

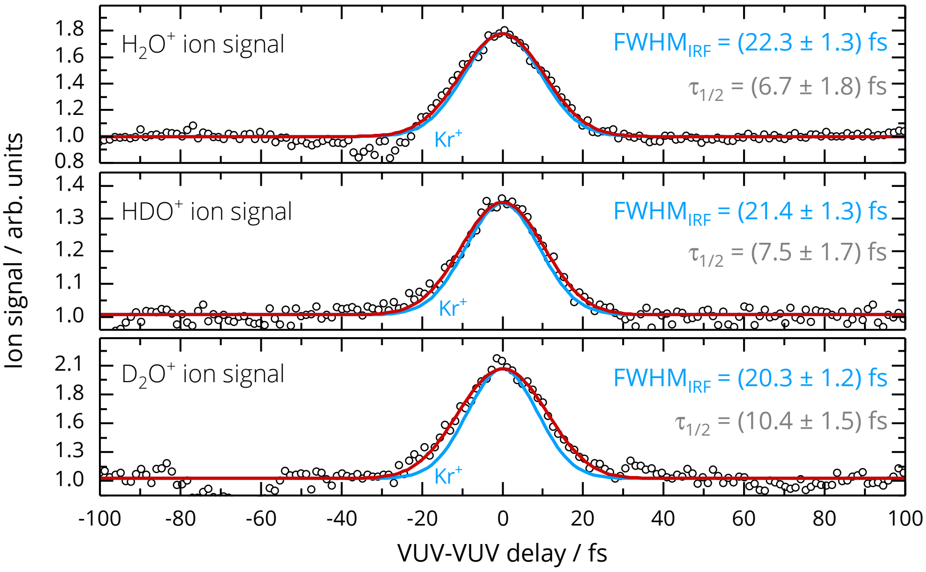

FIGURE 4.6– Delay-dependent ion signals for H_2O, HDO, and D_2O. The delay-dependent ion signal of each isotopologue is shown in comparison to the instrument response function (blue) recorded in the corresponding measurement series and fitted with a Gaussian function (red).

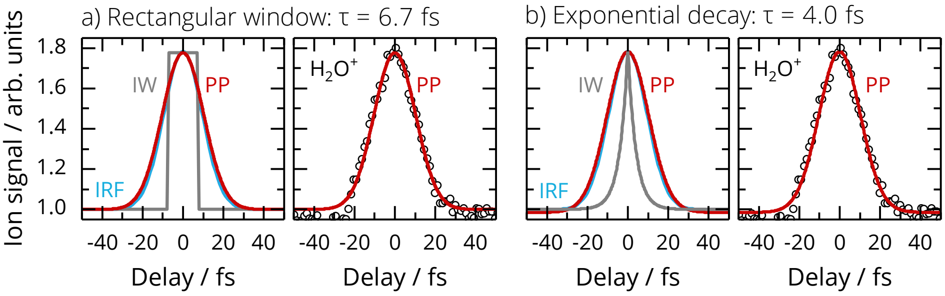

FIGURE 4.7– Comparison between different models for the ionization window, where the convolution between IRF and ionization window function (IW) is used to model the pump-probe signal (PP). For a rectangular window (a), a time constant of 6.7 fs is extracted by fitting the pump-probe function to the data. When an exponential decay (b) is assumed, a shorter time constant of 4.0 fs is retrieved.

auto correlation with a FWHM of (20.3 ± 1.2) fs. $\tau_{1/2}$ is (10.4 ± 1.5) fs in this case, which is consistent with a primary kinetic isotope effect of $\sqrt{2}$ from doubling the fragment mass. When an exponential decay function is used to deconvolve the duration of the ionization window, its duration is underestimated, because the delayed decrease of population in the ionization window is not considered. Slight differences of the instrument response function in the individual pump-probe experiments are attributed to the daily optimization of the laser system. By obtaining consecutive measurements it was ensured that the pulse duration was stable over the time the pump-probe measurement was performed.

For all isotopologues an excellent agreement between the duration of the ionization window deconvolved from the delay-dependent ion yield and the duration of the ground state ionization window derived from the mixed quantum-classical calculation was achieved, showing that ionization to the ionic ground state is the only significant probe transition contributing to the delay-dependent parent ion yield.

These results can be compared to existing multi-photon probe studies, to discuss the effect of the strong-field probe on the intrinsic dynamics. Trushin *et al.* [107] extracted a time constant of 3.5 fs for H_2O from an exponential decay model for the dynamics in the 1+5 photon ionization window, which is comparable to the window in the present study. The derivation of time constants from experimental pump-probe data sets is strongly influenced by the respective model used (exponential decay model compared to a rectangular window in the present study). If the exponential decay is used to evaluate the present delay-dependent data, a time constant of (4.0 ± 2.2) fs is extracted for H_2O, which agrees with the multi-photon probe result to within 15%. Due to the precision of the measurement a systematic effect of strong-field ionization in respect to the presented weak-field approach can not be excluded. When compared to the theoretical calculations for the lifetime of symmetric stretch vibration or the time the wave packet leaves the Franck-Condon region [90, 91], which are calculated to be 8 fs and 5 fs, respectively, a good agreement is reached.

Another key result of this joint experimental and theoretical study is, that the interpretation of pump-probe data even for a ‘simple’ dissociation reaction in the sub-10-fs regime is not trivial. Even when the instrument response function can be determined precisely, the choice of an appropriate model for the delay-dependence of the observable is necessary – in this case the ionization window duration. Assuming an exponential decay rate for the observable, as it is valid for most reactions studied on the few-hundred-femtosecond or picosecond time scale, leads in this case to an underestimation of the duration of the ionization window, while the deconvolved duration of a rectangular window coincides well with our mixed quantum-classical trajectory calculation.

This is demonstrated in Figure 4.7, where the fit results, assuming a rectangular ionization window and an exponential decay window are shown. Both models can be fitted to the data sets with high accuracy, emphasizing the need for sophisticated calculations, when ultrafast dissociation dynamics are analyzed.

In summary, the photodissociation dynamics of H_2O and its isotopologues in the $\tilde{A}\ ^1B_1$ state have been studied in a combined single-shot auto correlation and pump-probe experiment relying on a VUV-pump–VUV-probe scheme at 7.7-eV photon energy. This constitutes the first measurement with sufficient time-resolution and a single-color approach, which does not perturb the system under study, in contrast to multi-photon IR probe schemes. The experiments were accompanied by ab-initio calculations and allowed the identification of the relevant probe transition scheme. From two possible transitions, the excitation to the ionic ground state is the relevant probe transition. The expected duration of the 1+1 photon ionization window was predicted by calculating the time-dependent vertical excitation energies for an evolving wave-packet in the $\tilde{A}\ ^1B_1$ state. The experimentally deduced time of 6.7 fs the H_2O molecule takes to leave the single-photon ionization window while dissociating, as well the influence of hydrogen substitution (7.5 fs for HDO and 9.4 fs for D_2O), are consistent with the trajectory calculations using the ground-state ionization window.

4.2 IONIZATION WITH INTENSE UV PULSES

In the previous section 161-nm pulses where used as a perturbative probe to study intrinsic molecular dynamics without disturbing the potential energy landscape of the molecule. In Section 3.1.3 the generation of intense radiation at 268-nm was discussed: pulse energies of approximately (17.6 ± 0.2) μJ were realized. In the single-shot auto correlation setup the 268-nm beam will be focused down to ca. 4.3 μm, taking into account the focal length of 150 mm, and half of the initial beam diameter of 5.9 mm after propagation from the source to Si wedge at the entrance of the experimental end station. Considering the transmission of the experimental setup ($T_{UV} = 0.39$) intensities of $1.0 \times 10^{15}\ \mathrm{W\,cm^{-2}}$ are achieved when both 22-fs pulses are overlapped spatially and temporally. Consequently, experiments utilizing the high UV intensity available can not be regarded as perturbative, and strong-field effects need to be taken into account.

This section deals with the ionization of xenon and krypton with high-intensity ultraviolet pulses. This non-linear process was used earlier to determine the instrument response function and the pulse duration of the 161-nm pulses, considering it a non-resonant multiphoton ionization. With the higher intensities accessible with the UV pulses, this interpretation needs to be evaluated carefully. Hence, numerical calculations for the multiphoton and strong-field ionization processes are utilized to simulate the final spatial distribution of single and multiply charged ions in the common focus of both beams.

For these experiments both multilayer mirrors in the experimental setup (Fig. 3.3) are replaced for dielectric mirrors selecting the third harmonic at 268 nm exclusively. The other experimental

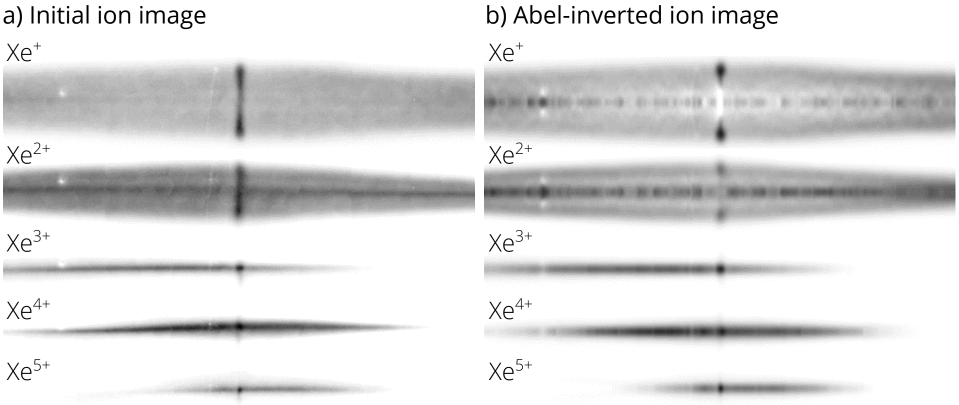

FIGURE 4.8– Ion microscope images retrieved at different intensities for Xe^{+}–Xe^{5+} ions. a) Initial ion images. b) Abel-inverted images after mirroring the initial images along their symmetry axis.

conditions are unchanged compared to the pulse duration measurements presented in Sec. 2.1.1. The ion microscope technique is applied to study the intensity-dependent and delay-dependent effects simultaneously by analyzing both dimensions of the ion image. By laterally imaging the Gaussian focus the direction perpendicular to the propagation coordinate of the beams can be used to extract intensity-dependent data. In combination with the simulation results the capabilities and limitations of the counter-propagating single-shot experiment for pulse metrology at high-intensities are evaluated, as well as possible applications in strong-field atomic physics.

4.2.1 STRONG-FIELD IONIZATION OF XENON

In the multiphoton picture xenon can be ionized by simultaneous absorption of three 4.62-eV photons, which exceeds the atom's ionization energy of 12.13 eV. This three-photon process is not resonant to any excited states of the atom, when no strong electric fields are present [115]. Similar to the two-photon ionization in krypton at a wavelength of 161 nm the non-linear ionization response may be used to determine the pulse duration by intensity auto correlation. As discussed above, intensities of up to 1.0×10^{15} W cm^{-2} can be realized in the third harmonic focus and a strong perturbation is expected, which acts also on the experimentally retrieved delay-dependent non-linear response.

Utilizing Eqn. 2.28 the adiabaticity parameter (Keldysh parameter) for the photon ionization of xenon at these intensities is 0.937, which indicates that strong-field effects, such as tunneling ionization may not be excluded [45]. With increasing intensity also higher ionization states of xenon become accessible. Figure 4.8 presents an overview of ion images retrieved at different UV intensities for xenon charge states up to Xe^{5+}. In this series, the intensity of the UV pulses has been reduced by moving apertures into the beam, which hinders a direct estimation of the intensity in the focus.

The spatial ion distributions in the images retrieved directly from the ion microscope (Fig. 4.8 a) cannot be compared quantitatively to each other, because they were retrieved at different UV intensities. In a qualitative analysis the geometric features can be examined in a comparative way, ignoring detector imperfections, as well as the hexagonal structure imprinted onto the image by the microchannel plate pore structure. The distributions for Xe^{+} and Xe^{2+} exhibit a strong broadening of the focal region, which corresponds to a diameter of ≈ 50 µm, exceeding the beam waist by a factor of 10. This broadening is attributed to the high charge density produced in the present experiment. For Xe^{+} more than 2000 singly charged xenon cations are detected per shot, resulting in an average charged particle density of more than 2×10^{11} particles per m^2, taking into account a beam diameter of 5 µm and a length of the channel of ca. 500 µm. Near the delay-time origin the density is more than doubled due to the superposition of both pulses. Higher charged states and ionization of residual gasses are not included in the calculation.

All species exhibit a pronounced region of intensity in the center of the image, which is perpendicular to the propagation coordinate of both beams and marks the temporal overlap region, where both pulses are superimposed in space and time. The width of this delay-dependent feature is in contrast to the diameter of the distribution only slightly broadened for Xe^{+} and Xe^{2+} compared to the higher charge states, which is in accordance to the previous analysis of particle density-dependent broadening effects [28]. Consequently, averaging along the lateral coordinate may again be utilized to retrieve a delay-dependent ion yield. Using the information contained in all five images, this may lead to a more precise analysis of the temporal properties of the UV pulses.

Furthermore, the lateral coordinate of the Xe^{+} and Xe^{2+} images exhibit additional structure, which deviate from a completely Gaussian intensity dependence: In the Xe^{+} image the width of the delay-dependent feature is increasing with the distance to the propagation axis. The Xe^{2+} image instead shows a region of pronounced intensity along the propagation axis.

Since the ion microscope retrieves a two-dimensional lateral projection of the three-dimensional ion distribution created by the UV pulses, the spatial distribution must be retrieved from the ion image to analyze the radius-dependent information. The cylindrical symmetry of the common Gaussian focus of the ideally aligned UV beams is transferred to the spatial ion distribution and the inverse Abel transformation can be used to retrieve the distribution from the ion image [116].

The inverse Abel transformation for a radius-dependent function $f(r)$ is retrieved from the function $F(y)$ depending on the projected coordinate y:

$$f(r) = -\frac{1}{\pi} \int_r^{\infty} \frac{dF}{dy} \frac{dy}{\sqrt{y^2 - r^2}}. \tag{4.2}$$

A freely available MATLAB function[*] implementing the method of Pretzler [117] for the inverse Abel transformation is applied here after mirroring the individual images along their axis of symmetry. In this method the radial distribution is expanded in a series similar to a Fourier-series:

$$f(r) = \sum_{n=1}^{n=\omega_u} A_n f_n(r), \qquad f_n(r) = 1 - (-1)^n \cdot \cos \frac{n\pi r}{R}, \qquad f_0(r) = 1 \tag{4.3}$$

A_n is the initially unknown amplitude of the cosine function $f_n(r)$, R is the radius of the distribution and ω_u is the upper frequency limit of the series. The resulting inverted images, using $\omega_u = 25$, are presented in Figure 4.8 b.

---

[*] Abel Inversion Algorithm (by Carsten Killer): http://www.mathworks.com/matlabcentral/fileexchange/43639-abel-inversion-algorithm

For Xe^{3+} – Xe^{5+} the Abel-inverted images are very similar to the project ion images, indicating a simple Gaussian-shaped radial intensity dependence of the ion signal, which is in accordance with the expectation of the focus of a Gaussian beam. For Xe^{+} the inversion reveals a shell-like structure, which is pronounced near the temporal overlap. This bleaching of the Xe^{+} ion yield for higher intensities near the propagation axis is evidence for a sequential ionization process, leading to a transfer of Xe^{+} ion yield towards higher charge states. Xe^{2+} shows a comparable structure, showing outer lobes, but also a higher ion yield along the propagation axis. This feature is also present to a lesser extent in the singly charged species. Yield fluctuations in the horizontal dimension are attributed to artifacts induced by the hexagonal MCP pore structure. Because the mass-to-charge ratio of Xe^{2+} does not coincide with singly charged atmospheric gases or other targets used in the experiment (see Fig. 3.9 for comparison), overlapping signals can be excluded. Its appearance in both lower charge states further substantiates the proposed sequential ionization process, because the Xe^{2+} ion yield must be proportional to the (transient) Xe^{+} yield.

To further investigate the ionization dynamics induced by the UV pulses a set of calculations have been performed in the MATLAB programming environment. The strong field ionization code from Wessels *et al.* [118] has been extended with the capability to deal with multiple pulses delayed in respect to each other (pump-probe) and sequential ionization dynamics in a simple rate equation approach.

For each time step Δt of the simulation the resulting population of each xenon species P_{t+1} is calculated from the current population P_t:

$$P_{t+1} = P_t + \Delta t \cdot \boldsymbol{\Omega} \cdot P_t \tag{4.4}$$

$\boldsymbol{\Omega}$ is the rate equation for sequential ionization in matrix form, allowing only sequential ionization:

$$\boldsymbol{\Omega} = \begin{array}{c} \begin{array}{cccccc} \text{Xe} & \text{Xe}^{+} & & \cdots & & \text{Xe}^{5+} \end{array} \\ \begin{pmatrix} 0 & 0 & 0 & 0 & +\omega_{\text{ADK}}^{4\to5} & 0 \\ 0 & 0 & 0 & +\omega_{\text{ADK}}^{3\to4} & -\omega_{\text{ADK}}^{4\to5} & 0 \\ 0 & 0 & +\omega_{\text{ADK}}^{2\to3} & -\omega_{\text{ADK}}^{3\to4} & 0 & 0 \\ 0 & +\omega_{\text{ADK}}^{1\to2} & -\omega_{\text{ADK}}^{2\to3} & 0 & 0 & 0 \\ +\omega_{\text{MPI}}^{0\to1} & -\omega_{\text{ADK}}^{1\to2} & 0 & 0 & 0 & 0 \\ -\omega_{\text{MPI}}^{0\to1} & 0 & 0 & 0 & 0 & 0 \end{pmatrix} \end{array} \tag{4.5}$$

The sum over all matrix elements is zero, guaranteeing that for an initial population expressed as the row vector

$$P_0^{\text{T}} = \begin{pmatrix} [\text{Xe}] & [\text{Xe}^{+}] & \cdots & [\text{Xe}^{5+}] \end{pmatrix} = \begin{pmatrix} 1 & 0 & 0 & 0 & 0 & 0 \end{pmatrix} \tag{4.6}$$

the total population is always equal to unity.

The individual rates are calculated by the equations stated in Section 2.2.2: For the three-photon ionization of Xe atoms to Xe^{+} ions the multiphoton ionization rate (Eqn. 2.31) was used. The

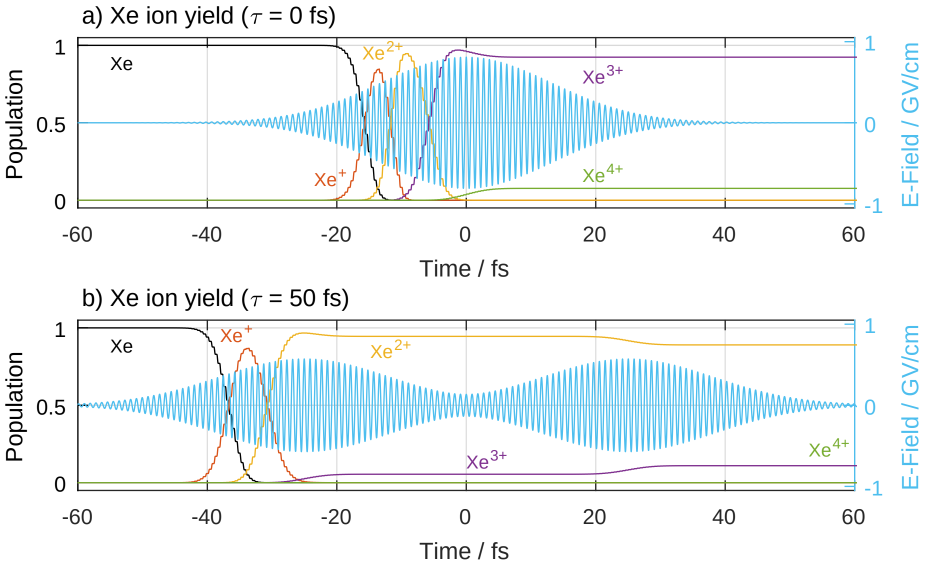

FIGURE 4.9– Simulated Xe charge species distribution after ionization by a UV pulse pair with 4 µJ energy per pulse (5.8×10^{14} W cm^{-2}) for a delay $\tau = 0$ fs (a) and $\tau = 50$ fs (b).

ionization cross section at 266 nm was determined experimentally [119] to be 1.1×10^{-82} cm^6/s^2. While for the higher charge states the ADK tunneling ionization rate (Eqn. 2.32) was applied.

The focus of the beams is described by equations for Gaussian beams (Eqn. 2.8–2.11) and the instantaneous intensity

$$I(r, z, t) = \frac{c\epsilon_0}{2}\mathcal{E}^2(r, z, t) \tag{4.7}$$

is used in the calculation. The common parameters for all calculations in this section are $w_0 = 5.0$ µm, $\tau_P = 22$ fs, $\lambda = 268$ nm for the individual pulses, while the pulse energy is varied.

The final spatial distribution of the ion yield is then calculated for each point of a two-dimensional grid (z, r). In the colliding pulse geometry the delay between the VUV pulses is mapped onto the z coordinate $\Delta\tau(z) = 2z/c$ (Eqn. 3.5), when both pulses overlap exactly in the focal plane. For each position (z, r) an integration over the temporal envelope of the pulse pair is performed with a time step of 20 as.

Figure 4.9 shows the time-dependent ion species distribution for a pulse energy $E_P = 4.0$ µJ per pulse calculated at $(z, r) = (0, 0)$ and the time-dependent electrical field at this position. When both pulses arrive at the same time, $\tau = 0$ (Fig. 4.9 a), a peak intensity of 5.8×10^{14} W cm^{-2} is reached. This high intensity leads to a sequential ionization on the rising edge of the pulse. When the maximum intensity is reached, the neutral population is long depleted and the majority of the population is ionized to Xe^{3+} and a small fraction of Xe^{4+}. Approximately 5 fs after the peak intensity is reached, the population is hardly changed. The step-like progression of the ionization visible in the figure is not an artifact of the figure, but indeed related to the instantaneous intensity, which oscillates at the carrier wave frequency and is maximal, when the field strength is high, but cannot be resolved with the available magnification of the microscope.

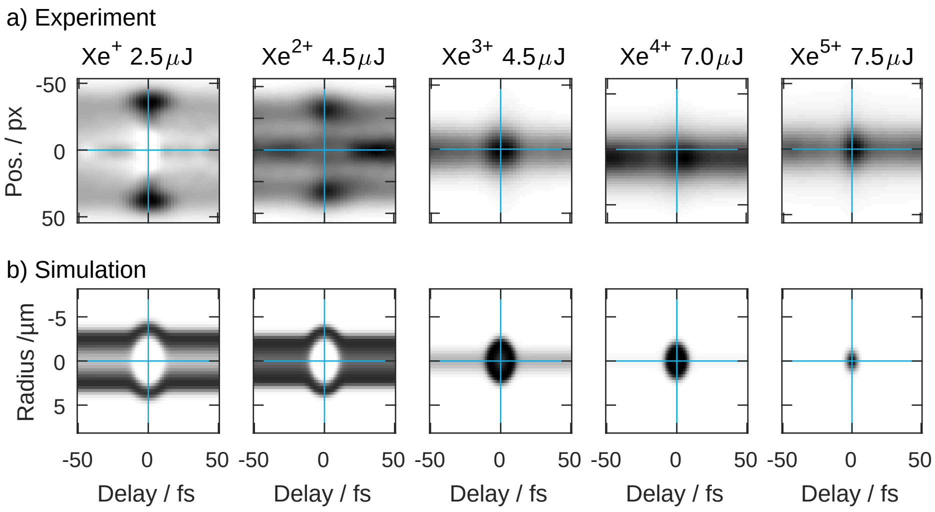

FIGURE 4.10– Comparison between experimentally retrieved Abel-inverted ion images (a) and simulated radius- and delay-dependent charge species distributions (b). The single pulse energies used in the simulation best matching the experimental result for the respective ion species are shown.

When the pulses are separated in time, in Fig. 4.9 b a delay of $\tau = 50$ fs is chosen, the maximum instantaneous intensity is reduced by a factor of two. Consequently, the ionization process is processing less rapidly. The first pulse still depletes the neutral population, but only a small fraction is triply ionized, while the majority of the population is made up by Xe^{2+} ions. After the delayed pulse replica arrives, the Xe^{3+} population is doubled, but Xe^{2+} ions form 80 % of the final population. As expected for a non-linear ionization process a delay-dependence of the final ion yield is observed, which can be used to determine the pulse duration of the UV pulses used in the experiment, although the deconvolution of the pulse duration from the width of the delay-dependence is less straight-forward.

To evaluate the retrieved ion images for the different Xe species (Fig. 4.8) the simulation is expanded. Simulations on a 2D spatial grid with r in the range of 0–8 µm (25 steps), and z in the range of 0–9.88 µm (39 steps, equivalent a delay range of 0–150 fs in 2.6 fs steps, which is the temporal step size of the position-sensitive detection unit in the experiment) have been performed. The intensity has been varied between 0.5 and 8.0 µJ in 0.5 µJ steps. For each position the final species population has been calculated with a 20 as time step.

The results for the intensities with the best agreement to the experimental ion images for the individual species are shown in Figure 4.10. Both, in the experiment (a) and the simulation (b) higher charge states are reached for higher pulse energies. The simulation for Xe^{+} and Xe^{2+} is able to reproduce the shell-like structure observed in the Abel-inverted images, while the higher charged species only show a pronounced region of intensity on the propagation axis. Hence, these effects can be attributed to the delay- and radius-dependent intensity envelope, which is described by a Gaussian for the radial component reaching zero outside of the focus, and a second Gaussian describing the delay-dependence, where the maximal intensity is doubled at the temporal overlap (See also Fig. 2.1 for comparison). The combination of both effects leads to a bleaching of the Xe^{+}

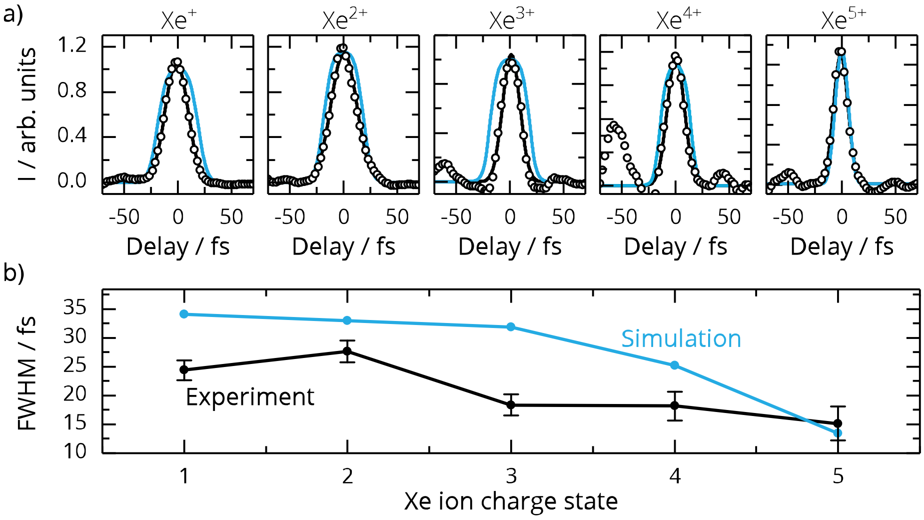

FIGURE 4.11– (a) Delay-dependent ion yield extracted from the experiment compared to the simulated delay-dependent species population (blue). Lineouts obtained by averaging along the radial coordinate near the maximum signal intensity. (b) FWHM of the respective signals with increasing charge.

population near the propagation axis, which is intensified near the temporal overlap in the first image.

Other features, such as the contrast between the delay-dependent feature and the ion yield for longer delays, are not well reproduced in the simulation. Although for a given radius (e. g. ±4 µm for Xe^{+}) a strong contrast is visible in the simulation, the contrast averaged over all radii is low. Instead of a peak signal, as in the experiment, a curve-like structure is observed in the simulation, where the yield is redistributed to higher radii with lower intensity. The simulation overestimates the saturation effects for higher delays.

Furthermore, the features in the simulation are sharper than the experimental result. Here it has to be noted, that the simulation does not entail any effects caused by the charge-particle imaging optics and repulsion between these particles. These space-charge effects lead to the considerable broadening along the radial coordinate, while the features in the delay axis are mostly preserved.

However, the most important question in the scope of this thesis is whether it is possible to extract the pulse duration of the third harmonic from the experimental data sets. From the pulse duration the instrument response function can be deduced and applied to the analysis of pump-probe experiments involving a UV pump-probe approach.

Figure 4.11 a shows an overview of the delay-dependent ion yield extracted from the Abel-inverted ion images averaged over the radii containing the delay-dependent intensity peak. A Gaussian fit (black) to the respective data set, as well as a line-out of the corresponding simulation result (blue) is shown.

Table 4.1 summarizes the FWHM of the delay-dependent features obtained from the individual data sets in Figure 4.11 a. With increasing charge, also visualized in Figure 4.11 b, the FWHM is decreasing both in the simulation and the experimental data sets, although the latter show deviations from a strictly decreasing behaviour.

TABLE 4.1– FWHM of the delay-dependent signal for the respective ion species extracted from the Abel-inverted ion images (experimental) and the simulated species population in femtoseconds.

	Xe^{+}	Xe^{2+}	Xe^{3+}	Xe^{4+}	Xe^{5+}
Experiment	24.4 ± 1.7	27.7 ± 1.9	18.4 ± 1.8	18.2 ± 2.5	15.2 ± 2.9
Simulation	34.0	33.0	31.8	25.2	13.4

In the multi-photon ionization picture Xe^{+} is produced by three-photon ionization. The expected pulse duration of the third harmonic is 22 fs, calculated in perturbation theory for a fundamental infrared pulse with a duration of 38 fs. Consequently, the FWHM, σ_{AC}, of third-order non-linear response in an auto correlation experiment is given by

$$\sigma_{\mathrm{AC}} = \sqrt{\frac{\tau_{\mathrm{P}}^2}{n} + \frac{\tau_{\mathrm{P}}^2}{m}} = \sqrt{\frac{n+m}{nm}}\tau_P = \sqrt{\frac{3}{2}}\tau_{\mathrm{P}}. \tag{4.8}$$

Where τ_{P} is the pulse duration and n and m are the number of photons absorbed by each pulse, in this case 1 and 2. With the pulse duration of 22 fs a FWHM of 26.9 fs is expected for the third-order auto correlation signal, which is in agreement with the obtained value for Xe^{+} in the experiment of (24.4 ± 1.7) fs. The precision of the measurement is comparable to the measurement of the instrument response function of the single-color fifth harmonic pump-probe experiment discussed in the previous chapter. The delay-dependent ion yield of the higher charged xenon species provide additional measurements of quantities directly related to the third harmonic pulse duration and thus might be used to increase the pulse duration measurement's accuracy even further.

But as discussed earlier, the dependence between the pulse duration and the FWHM of the delay-dependent ion yield is not trivial, when a higher field strength is applied and a reliable model is needed for the extraction of the pulse duration. Figure 4.11 b shows that the agreement between simulation and experiment for the FWHM is poor for all species except Xe^{5+}. Saturation effects appear, when the ionization probability approaches unity, leading to bleaching for small delays. This causes a flattening and broadening of the delay-dependent feature, visible for example for Xe^{3+} in Fig. 4.11 a. At the maximal intensity at $\tau = 0$ a significant part of the population is ionized further, and the maximum of the signal is suppressed. For Xe^{5+} no broadening is observed in the simulation, resulting in a better agreement with the experimental results.

The broadening is strongly influenced by small changes in the intensity. To analyze the experimental data sets with the goal to obtain a pulse duration, the intensity in the focus must be known with high accuracy, which was not the case here. Thus, the only valid measurement for the pulse duration is the Xe^{+} measurement and a pulse duration of (20.0 ± 1.5) fs was extracted, utilizing Eqn. 4.8.

4.2.2 HIGH-INTENSITY IONIZATION OF KRYPTON

Similar measurements have been carried out with the noble gas krypton as a target. Its ionization energy of 14.0 eV is slightly above thrice the UV photon energy (13.86 eV) and thus Kr is ionized

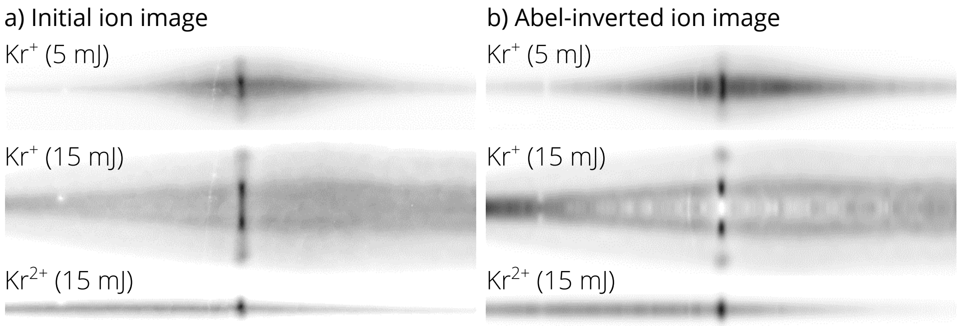

FIGURE 4.12– Ion microscope images retrieved at different fundamental pulse energies for Kr^+ and Kr^{2+} ions. a) Initial ion images. b) Abel-inverted images after mirroring the initial images along their symmetry axis.

dominantly by four photon ionization. In these measurements, the intensity has not been varied by inserting apertures into the beam, but instead the fundamental infrared laser pulse energy has been reduced to manipulate the UV intensity (see Fig. 3.2 for comparison). At an infrared pulse energy of 5 mJ the corresponding UV pulse energy is ca. 6.1 µJ. At the full infrared power of 15 mJ a pulse energy of more than 20 µJ is reached. This results in intensities per individual pulse in the focus of $1.6 \times 10^{14}\,\mathrm{W\,cm^{-2}}$ and $6.6 \times 10^{14}\,\mathrm{W\,cm^{-2}}$, respectively.

The retrieved ion images have been processed by the same Abel-inversion method introduced in the previous section and the results are presented in Figure 4.12. For Kr^+ at low intensity and Kr^{2+} at high intensity no additional structure is revealed in the Abel-inverted images, indicating that ionization to higher charge states is not dominant. At high intensities the spatial Kr^+ distribution exhibits rich sub structures: A bleaching similar to the one observed in xenon is observed near the propagation axis of the beams. With increasing radius, the ion yield first increases, then drops rapidly. For higher delays an outer less intense area is observed, where the ion yield is slowly decreasing with increasing radius before it decreases fast to zero. At $\tau = 0$ an additional delay-dependent feature is observed for the outer radii, which is less intense and broader than the intense peak near the propagation axis. Furthermore, at all intensities a slightly decreased ion yield for Kr^+ is observed before the yield reaches its maximum at $\tau = 0$.

First, the delay-dependent ion yield for Kr^+ (5 mJ IR) and Kr^{2+} (15 mJ IR) will be discussed in detail. Figure 4.13 presents the delay-dependent ion yield obtained by averaging along the radial dimension. The Kr^+ data set has been fitted by two Gaussian near zero-delay: One component for the delay-dependent peak, the second for the negative feature describing the diminishing of the ionization yield near $\tau = 0$. The deconvolution factor for a fourth-order auto correlation, when two photons are absorbed from each pulse is 1, calculated with Eqn. 4.8. The FWHM of (19.5 ± 1.5) fs, as extracted from the ion yield, is equal to the pulse duration of the UV pulse.

The intense signal in the delay-dependent ion yield of Kr^{2+} is broadened in comparison to the singly-charged species. This is inconsistent with the multiphoton picture, where a narrowing of the signal is expected, because double ionization of krypton is a nine photon process at 4.62-eV photon energy. As discussed extensively for xenon, strong-field effects need to be included in the discussion. An adiabaticity parameter of 0.95 is calculated for krypton from Eqn 2.28.

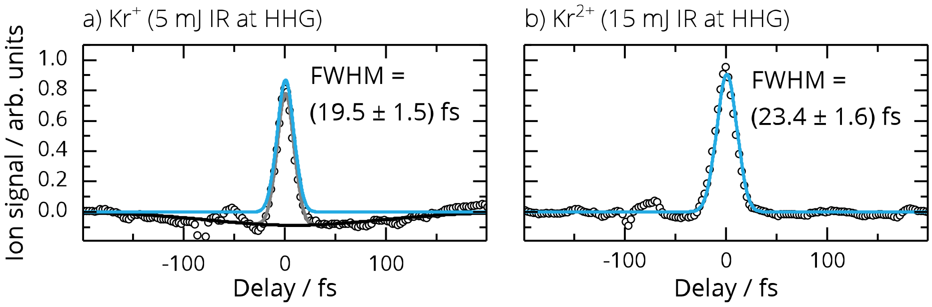

FIGURE 4.13– Delay-dependent ion yield for (a) Kr^+ (5 mJ IR) and (b) Kr^{2+} (15 mJ IR) extracted from the Abel-inverted images by averaging along the radial dimension.

Again, extracting a pulse duration from the higher charged species is only possible with a more sophisticated simulation and detailed knowledge of the intensity of the individual beams in the focus.

However, a detailed analysis of the Kr^+ ion yield at higher intensities may lead to an additional measurement of the temporal properties of the UV pulse. In the beginning of the subsection it was stated, that the energy of three photon is slightly below the ionization energy of krypton. Near the ionization limit, Rydberg states are closely spaced, since they are converging to the spin-orbit split ionic ground states. An overview of atomic states accessible by three photon absorption is shown in Figure 4.14 a, with the selection rules for the total angular momentum $\Delta J = (\pm1, \pm3)$ and the parity $\pi_f \neq \pi_i$.

The resonances shown here must be included in an accurate description of the delay-dependence of the krypton ion yield. The life times of Rydberg states are on the order of at least a few picoseconds, exceeding the delay times accessible in the experiment and thus reducing the peak-to-background ratio in an auto correlation experiment, because excited states prepared earlier by

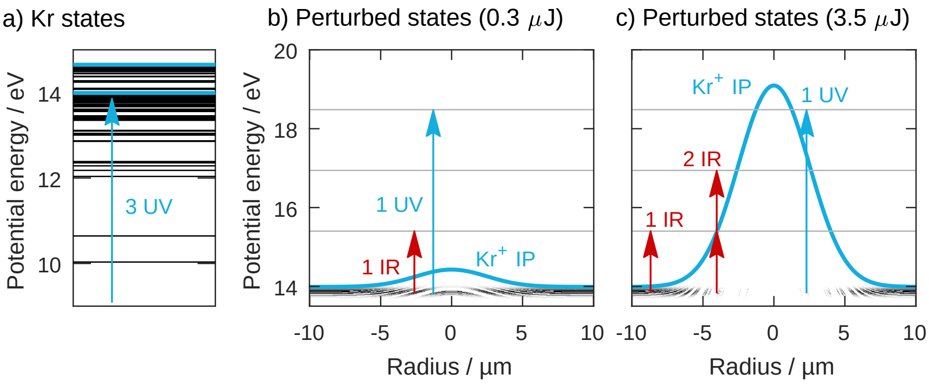

FIGURE 4.14– Electronic states of krypton accessible by three photon absorption. (a) Unperturbed states and ionization limits. Electronic states in the UV three-photon bandwidth in perturbed by AC stark shift at (a) $6.5 \times 10^{13}\,\mathrm{W\,cm^{-2}}$ and (b) $7.6 \times 10^{14}\,\mathrm{W\,cm^{-2}}$ as a function of the beam radius. The perturbed ionization potential and resonant ionization probe schemes are indicated.

three-photon absorption can be accessed by a single-photon probe pulse. Furthermore, the high intensities realized in the UV focus perturb the potential energy of the Rydberg states by AC stark shifts [29]. The non-resonant AC-stark shift can be approximated by the ponderomotive energy added to the potential energy of the state (Eqn. 2.30) for highly excited states, where the energy shift of the ionic core can be neglected [120]. These effects have already been used at moderate intensities by other groups to coherently excite shifted Rydberg states and study the fate of the prepared wave packet in the time-domain [120].

The effect is shown in detail in Figure 4.14 b. At moderate intensities realized by 0.3-µJ UV pulses (6.5×10^{13} W cm^{-2}) the maximal AC stark shift is ≈ 0.6 eV. Rydberg states initially in the bandwidth of the UV pulse (Fig. 4.14 a) are shifted with increasing intensity to higher energies for $|R| < 7$ µm, as shown in Fig. 4.14 b. Instead, lower lying Rydberg states are now excited by three-photon absorption. Due to the moderate shift, the increased ionization energy does not alter the available ionization probe schemes: Ionization by a fourth UV photon or a single IR photon is possible for all intensities. The single-photon ionization via residual infrared radiation must not be neglected here as in the non-resonant ionization of xenon. In the ideal case of perfectly perpendicular polarization the IR transmission of the optical setup is less than .001 for the central wavelength of 800 nm. Small differences in the polarization angle, as well as the 30-nm broad spectrum may allow a few microjoules of the total infrared pulse energy of 15 mJ to be transmitted by the optical setup. In a non-resonant process, where the non-linearity of infrared ionization is very high, this does not contribute to the signal. As a single-photon ionization probe this is not necessarily the case and might be responsible for the additional delay-dependent peak observed for Kr$^+$ at 15 mJ infrared pulse energy (Fig. 4.12).

For higher intensities (7.6×10^{14} W cm^{-2}) this effect is more drastic. The maximum AC stark shift is > 4.5 eV, completely shifting all Rydberg states out of resonance and increasing the binding energy of the valence electrons and thus the ionization potential enough to render four photon ionization impossible (Fig. 4.14 c). For radii $|R| < 4$ µm Rydberg states, which may lead to single IR photon ionization are shifted out of the UV pulse three photon bandwidth, and resonant photoionization is only possible by double IR ionization or UV ionization. At lower radii also these resonant pathways are closed and only non-resonant ionization is possible. Consequently it is of interest, how this complex intensity- and radius-dependent ionization scheme does affect the ion images retrieved in the experiment.

To address this question the simulation applied to the sequential ionization of xenon has been extended to also encompass resonant excitation to the Rydberg states, which are shifted transiently into the three-UV-photon bandwidth. According to the best knowledge of the author, three-photon absorption cross sections for the involved Rydberg states, as well as the ionization cross section for probing these states by UV and IR ionization are not available in the literature to this date. The values provided in Table 4.2 are the result of iterative optimization during the simulation. Consequently, the simulation results only provide a qualitative interpretation of the delay- and intensity-dependent absorption and ionization processes involved.

The absorption rate of the Rydberg states has been calculated similar to the multi-photon ionization rate (Eqn. 2.31), using the spectral intensity at the excitation wavelength of the Rydberg state:

TABLE 4.2– Simulation parameters for the UV and IR pulses, and estimated cross sections for three-photon Rydberg excitation σ_{Ryd} and non-resonant four-photon UV ionization $\sigma_{\text{i-nr}}$.

λ (nm)	E$_{\text{P}}$ (µJ)	w_0 (µm)	τ_{P} (fs)	σ_{Ryd} (cm^6/s^2)	$\sigma_{\text{i-nr}}$ (cm^8/s^3)
268	6.0	5.0	22	8×10^{-86}	5×10^{-118}
804	20.0	10.0	37		

$$\omega_{\text{Ryd}}(I,\lambda) = \sigma_{\text{Ryd}}\Phi^n(I,\lambda) = \sigma_{\text{Ryd}}\left[\frac{I(\omega)}{\hbar\omega}\right]^n . \tag{4.9}$$

The parameters used for the individual pulses are stated in Table 4.2. The high divergence of the IR pulse leads to a mismatch between the position of the IR pulse focal plane and the UV pulse focal plane, which is included in the simulation by choosing a ω_0 of 10 µm. The same estimated three-photon absorption cross section is used for all Rydberg states. Non-resonant four-photon ionization by the UV pulses is also considered. The involved rate equation allows for non-resonant ionization, as well as resonant ionization by a single UV photon and one or two IR photons after three-photon excitation of AC-stark shifted Rydberg states. Prepared Rydberg excitations have an infinite life time in the simulation delay range of ±150 fs.

The single-UV-photon ionization, as well as single- and two-IR-photon ionization cross section is proportional to $n^{-3}{\omega_0}^{-10/3}$, where n is the principal quantum number of the respective state and ω_0 the central angular frequency of the laser pulse [120]. A proportionality factor of 4.5×10^{36} has been used for the single-photon ionization and 4×10^2 for the two-photon IR ionization. For all states infrared ionization is preferred. Sequential ionization to Kr^{2+} has been included by employing ADK theory with a pre-factor for the ADK-rate of 2% to accommodate for the over-estimated Kr^{2+} yield, which was not in accordance with the experimental results presented in Fig. 4.12.

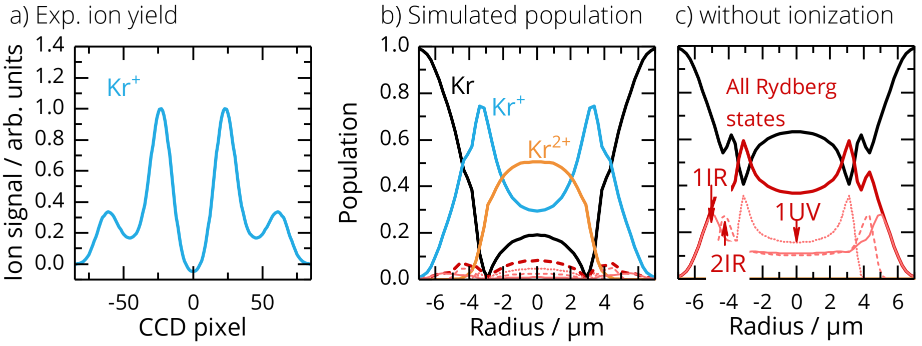

FIGURE 4.15– Experimental ion yield at $\tau = 0$ fs and simulated radius-dependent species distribution for krypton in the atomic ground state, excited Rydberg states, as well as singly and doubly ionized krypton. (a) Experimental ion yield. (b) Simulated final species distribution. (c) Same simulation, when ionization is not allowed.

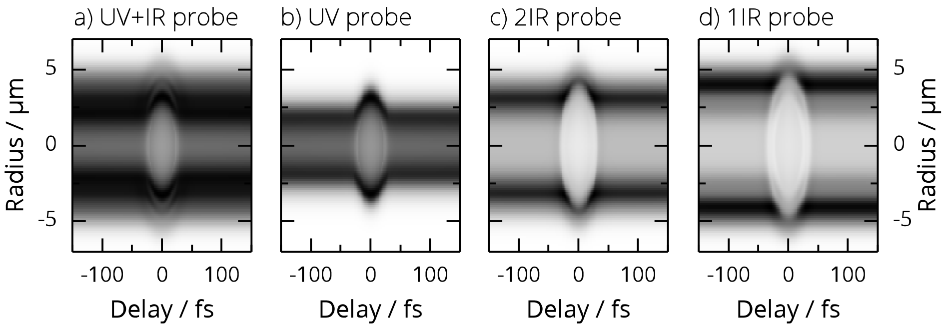

FIGURE 4.16– Simulated delay- and radius-dependent Kr^+ ion yield. (a) Allowing UV and IR ionization. (b) Only (non-)resonant UV ionization. (c) Only two-photon IR ionization after Rydberg excitation. (d) Only single-photon IR ionization.

Figure 4.15 shows the experimentally retrieved Abel-inverted ion yield as a function of the position given by the CCD camera pixels and the results of the simulation for the delay $\tau = 0$ fs as a function of the radius. The experimental results (Fig. 4.15 a) show clearly separated peaks. The final species distribution after all four pulses have passed is shown in Figure 4.15 b as a function of the radius for ground-state Kr atoms, as well as Kr^+ and Kr^{2+} ions. The Rydberg state population has been simulated for all three-photon allowed 93 Rydberg transitions and the resulting final population has been grouped into states, which may be interrogated by a single IR photon (86 states), only two IR photons (5 states), or exclusively by UV photon ionization (2 states).

The UV pulse intensity shows a Gaussian dependence on the radius, and ionization is more probable for lower radii. The shell-like structure, also visible earlier in the xenon data sets, is reproduced by the simulation, as well as the sequential ionization to Kr^{2+} near the beam propagation axis. In contrast to the xenon results, the two maxima of the Kr^+ ion yield are modulated due to the 3UV+X resonant ionization schemes, which is in accordance with the observation in the ion images (Fig. 4.12). In the final species distribution the Rydberg states are nearly fully depleted by the probe pulses. While the simulation qualitatively supports the validity of the proposed ionization schemes, the distance between the peaks observed in Fig. 4.15 a is not well reproduced in this simulation, which is based on iteratively optimized multi-photon ionization cross sections and ion optics abberations.

To emphasize the role these Rydberg states play in creating the delay- and radius-dependent ion image a second simulation with the same parameters has been performed, where the ionization cross sections have been reduced to zero (Fig. 4.15 c). Because all rate equations are coupled, this does obviously not yield a quantitative picture of the Rydberg population. As expected from the AC-stark shift (Fig 4.14 c) population of Rydberg states, which lie well below the UV three-photon bandwidth becomes more dominant for smaller radii and higher intensities. For small radii only the rising edge of the pulse populates the high-lying Rydberg states.

While the radial-dependence of the Kr^+ yield does not provide a perfect match of the experimentally obtained distribution, the radius-dependent variation of the ionization scheme is confirmed qualitatively in the calculation.

The full simulation has been carried out on a 2D grid with a delay range of 0–150 fs and 2 fs time

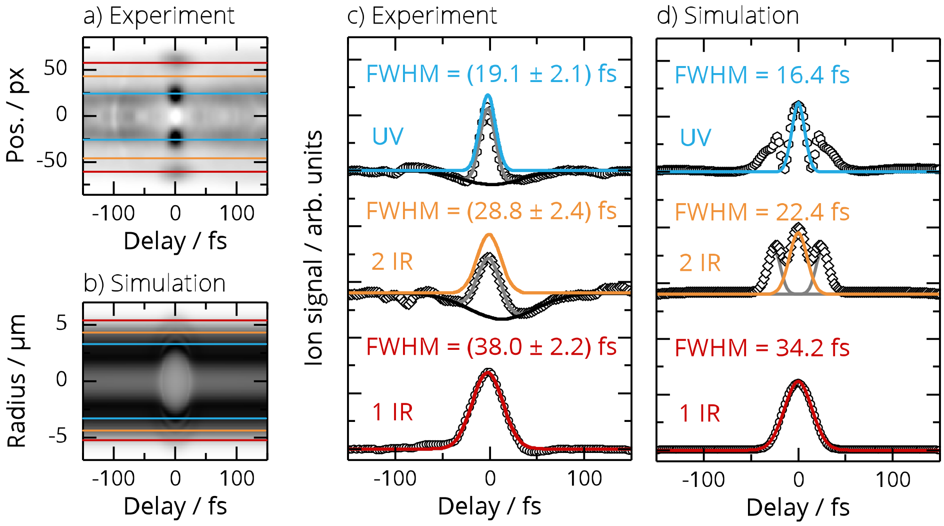

FIGURE 4.17– Comparison between the Abel-inverted ion image (a) and the simulated delay- and radius-dependent Kr^+ ion population (b). Delay-dependent traces have been extracted at the lines indicated, which are attributed to different probe schemes: UV ionization (blue), two-photon IR ionization (orange) and single-photon IR ionization (red) for the experiment (c) and simulation (d), respectively

steps and radii in the range of 0-7 μm (30 steps). The results are shown in Figure 4.16. The first panel a shows the final Kr^+ ion yield, allowing all ionization pathways. Similar to the non-resonant xenon ionization bleaching is observed near the beam propagation axis, which is more pronounced at small delays. The most important difference is the fine-structure observed in the center of the image. The variation with increasing radius is due to the intensity-dependent change in the contribution strength of the different probe schemes.

To visualize this Figure 4.16 b–d shows the individual contribution of the (non-)resonant UV ionization (b), the two-photon IR ionization from the Rydberg states (c), as well as the single-photon IR ionization (d). It is obvious, that with a decreasing AC-stark shift, the probe schemes with a lower total photon energy become dominant. These then lead to the structure observed in the Abel-inverted ion image (Fig. 4.12). Again, as for Xe, the ionization rates for longer delays are overestimated in the simulation, leading to a strongly reduced contrast in the simulation compared to the experimental results. Due to the estimated excitation and ionization cross section a quantitative agreement was not expected, but the indication of the mechanism leading to the emergence of a complex pattern in the spatial ion distribution could be elucidated.

A direct comparison between the experimental and calculated data sets is shown in Figure 4.17 a–b. The deviation between both data sets shows again, that the contrast between the data at short delays and higher delays, is not well resolved in the simulation. But more importantly, similarities for the delay-dependence of the outer peaks is visible, e. g. for the IR-probe pathway.

The Kr^+ ionization yield is analyzed as the result of overlapping multi-photon excitation pathways, and thus provides a single measurement with multiple observables, which can be traced back to the pulse duration of the UV and IR pulses. Only the bleaching near the propagation access is modeled as a strong-field effect and a broadening similar to the observation in the Xe^+

or Kr^{2+} ion yield might interfere with discerning a pulse duration from the measurement. To achieve this goal, lineouts at different radii indicated in Figure 4.17 a and b, have been extracted, which show the delay-dependence of the 1UV-probe (blue), 2IR-probe (orange) and 1IR-probe (red) pathway, respectively.

For the Abel-inverted ion image a clear Gaussian delay-dependence, superimposed on a negative component due to the reduced resonant ionization cross section at higher intensities, is observed (Fig. 4.17 c). The FWHM of each trace can be attributed to a scheme, involving four UV photons (blue), three UV and two IR photons (yellow), or three UV and a single IR photon. For the UV auto correlation a FWHM of (19.1 ± 2.1) fs is observed, the 2IR-probe yields a FWHM of (28.8 ± 2.4) fs and the single-photon IR probe a FWHM of (38.0 ± 2.2) fs (red). When a relationship of $\sigma_{\mathrm{IR}} = \sqrt{3}\sigma_{\mathrm{UV}}$, as expected from perturbation theory, is presumed, the individual observables are related to the UV pulse duration by Eqn. 4.8. These result in a pulse duration of (19.1 ± 2.1) fs (4UV, deconvolution factor 1), (21.3 ± 1.8) fs (3UV+2IR, deconvolution factor 1.354), (20.8 ± 1.2) fs (3UV+1IR, deconvolution factor 1.826), respectively.

The resulting mean pulse duration is (20.6 ± 1.2) fs, which is in agreement with the previous measurements with Xe^{+} of (20.0 ± 1.5) fs and Kr^{+} at low intensities of (19.5 ± 1.5) fs. By utilizing three observables in a single measurement the precision of the pulse duration measurement was increased by 25%. Furthermore, it was shown that the colliding pulse pump-probe technique gives access not only to delay-dependent information in a single shot, but also to intensity-dependent quantities without performing an intensity scan.

The AC stark shift is typically either neglected in the evaluation of pump-probe experiments or considered as a perturbation to another experimental observable, which is in the scope of the experiment. Here, this effect was exploited to widen the potential of a pulse metrology measurement. The increased precision of the pulse duration determination is important, but the possibilities in the grasp of this technique to study complex phenomena are even more interesting. Combined with a precise energy measurement of the individual beams, the ion microscope can be used acquire delay- and intensity-dependent data sets in a single shot at the repetition rate of the laser system, where typically long and challenging measurement campaigns involving scanning both delay and intensity are necessary, which have high demands on the long-term stability over many hours to achieve a meaningful result.

4.3 UV–VUV CROSS CORRELATION

Another advantage of the colliding pulse pump probe technique is, that both beam paths a separated and each beam can be manipulated independently. This renders multi-color pump-probe experiments possible, without invasive changes toward the experimental design. For an experiment utilizing both the UV and VUV radiation provided by the harmonic source, an exchange of mirrors in one branch of the experimental setup is sufficient to realize a two-color experiment (Fig. 4.18). Other combinations of pump and probe wavelength may be realized by insertion of thin-film metallic filters, such as In or Sn, selecting the 9th–15th harmonic.

Of course also these experiments rely on a robust measurement of the instrument response function for each pump-probe scheme. It was shown in the previous section, that an in-situ measurement of the third harmonic pulse duration was possible in an auto correlation scheme,

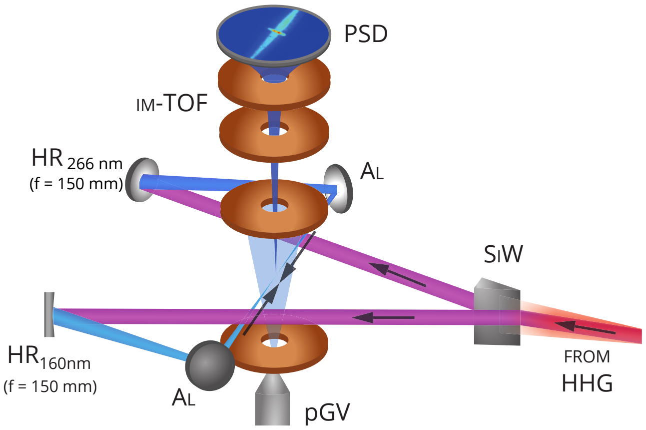

FIGURE 4.18– Schematic of the experimental setup for UV–VUV pump probe experiments.

even when higher intensities are involved. In two-color experiments, the intensity provided by the UV pulse will be reduced to match the VUV intensity, which is lower due to the fifth harmonic's pulse energy of $< 1\mu J$. Although this relaxes the need for a complex analysis of the delay-dependent signal, the richer spectrum achieved by superimposing third and fifth harmonic may lead to other complications, because resonant excitation of intermediate states is more likely.

4.3.1 UV–VUV PHOTOIONIZATION OF NOBLE GASES

Earlier, the instrument response function for an experimental scheme has been determined utilizing the non-resonant multi-photon ionization of the noble gases xenon and krypton. Multi-photon ionization is of course also possible by a combination of third and fifth harmonic radiation. Both, Kr and Xe exhibit a rich spectrum of Rydberg excitations, which might be accessed by a combination of third and fifth harmonic. Figure 4.19 gives an overview of states, which can be resonantly excited by one, two or three photon absorption. As in the previous section absorption

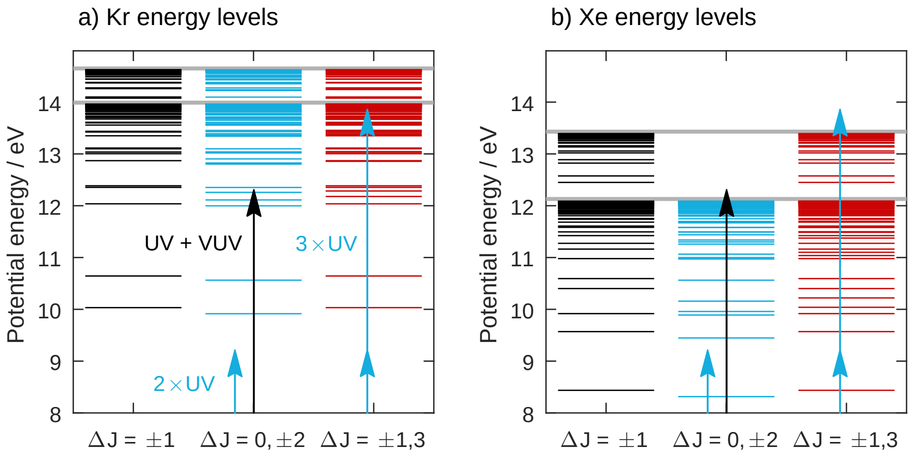

FIGURE 4.19– Electronic states of krypton (a) and xenon (b) grouped by selection rules. Excitation schemes with combinations of UV and VUV are indicated.

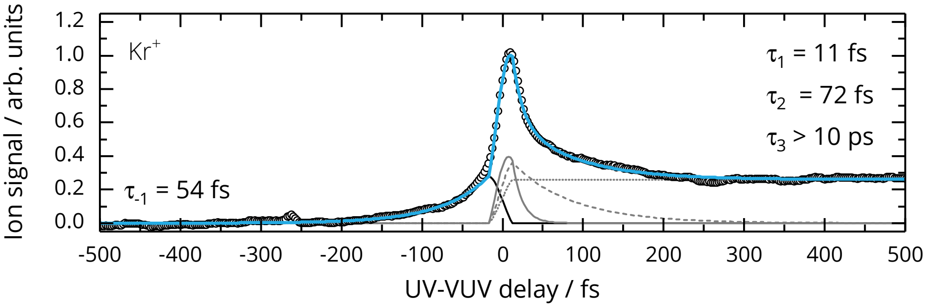

FIGURE 4.20– Delay-dependent ion yield for Kr^{+} in a UV–VUV pump-probe scheme.

of three UV photons in Kr (Fig. 4.19 a) excites Rydberg states close to the first ionization potential. Also a combination of both pulses might excite states by two photon absorption.

Rydberg excitation typically exhibits life times, which are on the order of picoseconds. In a two-color scheme, where pump and probe are not equivalent, one pulse, for example the third harmonic, may prepare a Rydberg excitation, which can be interrogated by single-photon ionization utilizing photons from the fifth harmonic pulse. Due to the long life time, this leads to a slowly decreasing delay-dependent ionization yield and an asymmetry, since interchanging third and fifth harmonic at negative delays does not prepare the same states.

This is exactly the case in a UV–VUV pump-probe experiment with krypton. Figure 4.20 shows the delay-dependent ion yield for Kr^{+}. In all presented UV–VUV pump-probe data sets the convention is, that for positive delays the UV pulse arrives first and thus is termed the pump pulse, while the VUV pulse probes the system. At negative delays this is vice-versa: The VUV pulse arrives early and pumps the system, which is then interrogated by a UV probe pulse.

Compared to the previously presented experiments, the delay-dependent ion yield is more complex and cannot be modeled by a Gaussian function or the convolution between instrument response function and a single exponential decay function. To analyze the data a fit procedure has been implemented in the MATLAB programming environment, to optimize a model of the type

$$S(t) = \Gamma_{\mathrm{IRF}}(t) \otimes \left[\underbrace{\sum_{i}^{n} A_i \exp\left(-\frac{t}{\tau_i}\right)}_{\text{for } t \geq 0} + \underbrace{\sum_{j}^{m} A_j \exp\left(\frac{t}{\tau_j}\right)}_{\text{for } t \leq 0} \right]. \tag{4.10}$$

$\Gamma_{\mathrm{IRF}}(t)$ is the instrument response function, expressed as a Gaussian function, which is convoluted with a sum of exponential decay function with a weight $A_{i,j}$ and a decay constant of $\tau_{i,j}$ either for a UV–VUV pump-probe scheme ($t \geq 0$) or the VUV–UV pump-probe scheme ($t \leq 0$). Here t defines the delay between UV and VUV pulse to avoid confusion with the decay constant τ. The FWHM of $\Gamma_{\mathrm{IRF}}(t)$ is calculated from Eqn. 4.8, using a pulse duration of 21 fs for the third harmonic and 16 fs for the fifth harmonic in a 2UV + 1VUV photon scheme.

The dominant contribution to the delay-dependent ion yield is a slowly decaying exponential function $\tau_3 > 10$ ps, which appears, when the UV pulse arrives early and can be attributed the

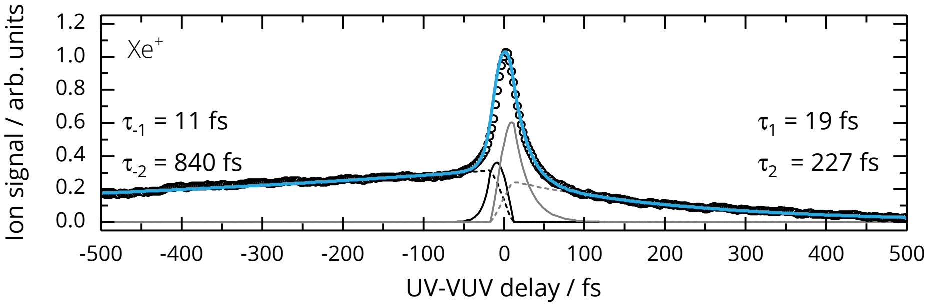

FIGURE 4.21– Delay-dependent ion yield for Xe^+ in a UV–VUV pump-probe scheme.

population of high-lying Rydberg states by three photon absorption (Fig 4.19 a). Furthermore, faster decay components are observed: $\tau_1 = 11$ fs is likely to due residual IR radiation probing the Rydberg excitation prepared by the UV pulse. Although the transmission of IR is below 0.1%, ionization from these Rydberg state is more likely for longer wavelengths. The origin of $\tau_2 = 72$ fs and $\tau_{-1} = 54$ fs is still an open question that exceeds the scope of this measurement. For example, the relevance of auto-ionization states or other short-lived state should be investigated in the future. The original goal, an experimental determination of the instrument response function, could not be fulfilled with this measurement, since the observed delay-dependent signal is a convolution of the instrument response and its intrinsic dynamics.

The same is true for a measurement, where xenon is used as a target (Fig. 4.21). Again multiple delay components are observed, both for negative and positive delays.

Although no direct resonances are accesible in Xe (see Fig. 4.19 b), an AC stark shift of less than 0.2 eV is sufficient to resonantly excite high lying Rydberg states by simultaneous absorption of a UV and VUV photon. Futhermore, this shift increases the binding energy of the electron and might close the UV+VUV two-photon ionization pathway.

Again, small time constants (τ_1 = 19 s and $\tau_{-1} = 11$ fs) are observed, which indicate an influence of residual IR radiation. The slowly decaying component $\tau_{-2} = 840$ fs is attributed to population of AC-stark shifted Rydberg state by simultaneous absorption of a UV and VUV photon. Since this is happening also at longer delays, a fraction of UV radiation must be contained in the fifth harmonic pulse. When the UV pulse arrives early another time constant $\tau_2 = 227$ fs is observed. This time constant is short for a Rydberg state life time, but might be due to population of auto-ionization states located above the first ionization potential, stemming from spin-orbit splitting (see Fig. 4.19).

Additional measurements have been performed in argon, which are shown in the appendix A.2. For the same reasons as in krypton and xenon a long-lived exponential component is observed in the delay-dependent ion yield. Consequently, it can be concluded that multi-photon ionization of noble gases with a combination of 268-nm and 161-nm radiation is not an ideal non-linear process to retrieve the cross correlation of these pulses. Excitation of Rydberg and auto-ionization states induces delay-dependent features, which hinder the retrieval of the instrument response function.

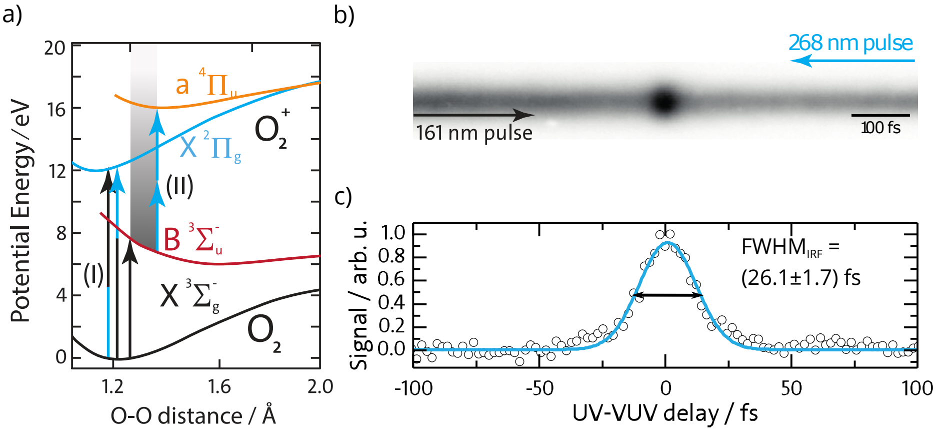

Figure 4.22– Excitation scheme and delay-dependent ion yield of O_2. (a) Excitation pathway I UV + VUV photon, Excitation path II VUV + 2 UV photons. (b) O_2^+ spatial distribution in the common UV + VUV focal region. (c) Delay-dependent O_2^+ yield with subtracted offset.

4.3.2 UV–VUV Photoionization of Molecular Oxygen

A counter-intuitive solution to this problem is to resort to a measurement of the instrument response function in a molecule, which is known to show dynamics induced by the absorption of a 161-nm photon: Molecular oxygen. In a previous study lead by Oliver Schepp it was shown that 161-nm radiation excites the B $^3\Sigma_u^-$ state of the molecule, which then undergoes rapid dissociation [60]. In a VUV-pump – VUV-probe scheme this process is observable in an ionization window of (5.6 ± 1.6) fs.

In a two-color experiment the observation window for the dynamics is even shorter. Figure 4.22 a shows the two dominant excitation schemes. At the equilibrium geometry non-resonant two-photon (1 UV + 1 VUV) absorption leads to the formation of stable oxygen cations in the electronic ground state (scheme I) and is corresponding to the UV-VUV cross correlation. Although, molecular cations can also be produced by the sequential three-photon ionization scheme II with considerably lower probability.

If 2-UV photon ionization from the $^3\Sigma_u^-$ state is considered as a contribution to the cross correlation signal, the temporal deviation from the instrument response function would be negligible. This is due to the fact that the ionization window, that is the internuclear distance interval where it is possible to ionize the molecule with two UV photons from the $^3\Sigma_u^-$ state, is closing in less than 3 fs (O-O bond elongation of 0.1 Å). This would result, if at all, in a negligible broadening of the experimental signal, taking into account that the non-resonant 1 VUV + 2 UV photon transition has a much lower probability than the dominant 1 VUV + 1 UV photon.

These prerequisites are ideal to measure an instrument response function, where $\sigma_{\mathrm{IRF}} \gg \tau$ and τ is the duration of the ionization window. In Figure 4.22 b–c the retrieved ion image, as well as the delay-dependent O_2^+ yield is presented. As expected only small deviations from a Gaussian delay-dependence are observed. The retrieved FWHM of the instrument response function is (26.1 ± 1.7) fs, which is in excellent agreement with the expected FWHM of the UV + VUV cross correlation for a UV pulse with a duration of 22 fs and a VUV pulse with a duration of 16 fs.

4.4 (V)UV PHOTODISSOCIATION OF IODOMETHANE

Iodomethane is an ideal candidate to apply the UV + VUV two-color methodology laid out in the previous chapter. On the one hand it is a widely used benchmark molecule used to validate novel time-resolved techniques addressing UV dissociation reactions, due to its well-studied 100-fs dissociation dynamics in its first excited state. On the other hand, iodomethane exhibits a variety of highly excited Rydberg states, which may be excited in the VUV spectral range. Their dynamics are with few exceptions widely unexplored. The contents of this section have been published previously in *Journal of Physical Chemistry A* [121].

These ultrafast photoinduced reaction dynamics are often governed by the interplay between multiple electronic states connected by non-adiabatic crossings, allowing the rapid transfer of population from an initially excited state to enabling intermediate states leading to the desired reaction products [10–12]. The multitude of Rydberg excitations accessible with photon energies in the vacuum ultraviolet spectral range may act not only as mere spectators, but as gateway states facilitating ultrafast reaction dynamics. Very often they enable new reaction pathways [122, 123] or efficient photodeactivation mechanisms of fundamental importance to nucleobases and proteins [13, 124].

Here, the photodissociation dynamics of iodomethane, initiated by UV-excitation in the first absorption band and by single VUV-photon excitation of the 6p ($^2E_{3/2}$) Rydberg state are investigated in a single experiment. Excitation of the A-band (220-350 nm) has received significant attention as it constitutes a prototypical system to study sub-100-fs dissociation dynamics, which are influenced by a non-adiabatic crossing. Many experiments [3, 125–136] with a variety of excitation and detection schemes, as well as theoretical studies [130, 137–139] have been conducted to elucidate the importance of different reaction channels mediated by initial population of different vibrational and electronic states. However, with exception of the low-lying Rydberg states in the B-band [140–142], Rydberg state reaction dynamics have so far only been studied experimentally by multi-photon excitation [123, 131, 143, 144] and their potential to enable yet undiscovered dynamics is widely unexplored.

In contrast to two-photon induced dynamics, reactions initiated by single-photon absorption can not only be realized in ultrafast laser laboratories and provide information about photochemical mechanisms that may occur at the upper layers of Earth's atmosphere. Iodomethane is not only a prototypical system to study femtosecond dissociation dynamics, but its decomposition is relevant in environmental chemistry [145]. The presented study is tailored to investigate molecular decomposition mediated by Rydberg state excitation in a largely unexplored spectral domain.

For these means, a combination of intense 16-fs, 161-nm (7.7-eV) [25] and 21-fs, 268-nm (4.6-eV) pulses is utilized to perform a single-shot VUV/UV pump-probe experiment [28]. The ν_1 vibrational state of the 6p ($^2E_{3/2}$) Rydberg state is excited by single VUV-photon absorption [146] and acts as a gateway state to initiate dissociation along the H_3C-I bond, which is then probed by one or two UV-photons. Simultaneously, the A-band dissociation dynamics are accessed, when pump and probe pulses are interchanged and the UV pulse arrives first.

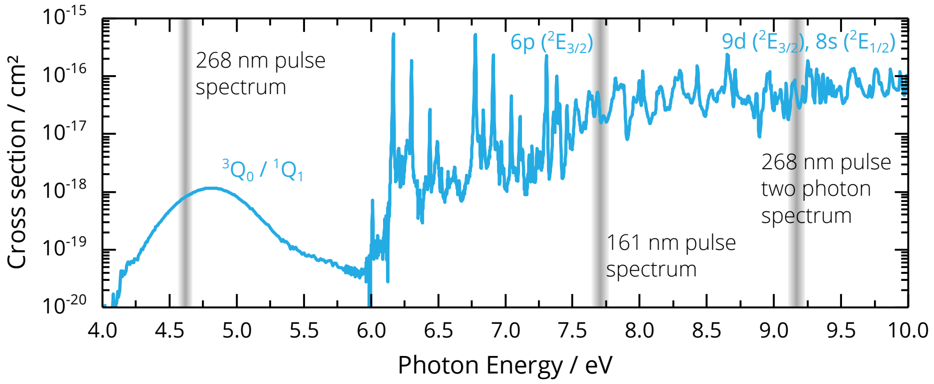

FIGURE 4.23– Photo-absorption cross sections of iodomethane in the UV and VUV spectral range. Data is taken from Ref. [146].

4.4.1 BACKGROUND

The photo-absorption spectrum (Fig. 4.23) of iodomethane is constituted by a broad absorption feature between 4.0 and 6.0 eV, which stems from transitions to several repulsive states and is called the A-band. Additionally, several sharp absorption features are found at 6.2 eV, 6.8 eV and 7.4 eV, which are the band heads of the B-, C- and D-band, respectively. [146] In the bandwidth of the 268-nm UV pulse, the dominant transition leads to population of the $^1Q_1$ and $^3Q_0$ states, due to a $n \rightarrow \sigma^*$ electron excitation [147]. At 268 nm the transition to the $^3Q_0$ state is preferred, due to a higher absorption cross section. These repulsive states correlate with the respective spin-orbit split ground states: $^1Q_1 \rightarrow X^1E_{3/2}$ and $^3Q_0 \rightarrow X^1E_{1/2}$. Furthermore, both states are coupled by a conical intersection allowing a rapid partial population transfer from the $^3Q_0$ state to the $^1Q_1$ state. This results in a product branching ratio of 0.70–0.81 between spin-orbit excited iodine fragments ($\mathrm{I}^2P_{1/2}$) and ground state iodine atoms ($\mathrm{I}^2P_{3/2}$), respectively [138]:

$$\begin{tikzcd}
 & \mathrm{CH_3I^*}\ (^3Q_0) \arrow[r] \arrow[dd, "\mathrm{CI}"] & \mathrm{CH_3} + \mathrm{I^*}\ (^2P_{1/2}) \\
\mathrm{CH_3I}\ (\tilde{X}\ ^1A_1) \arrow[ur, "\hbar\omega", "268\ \mathrm{nm}"'] \arrow[dr, dashed, "\hbar\omega", "268\ \mathrm{nm}"'] & & \\
 & \mathrm{CH_3I^*}\ (^1Q_1) \arrow[r] & \mathrm{CH_3} + \mathrm{I}\ (^2P_{3/2})
\end{tikzcd}$$

This dissociation dynamics has been the subject of many time-resolved studies: starting from the pioneering work of Khundkar & Zewail [126] and has been revisited utilizing the velocity map imaging technique [134, 139]. Consequently, the dissociation time constant for both channels are well known and may be used to validate the experimental results retrieved with the two-color single-shot pump-probe technique. Dissociation through the $^3Q_0$ state is complete in (94 ± 6) fs, while dissociation evolving through the conical intersection to the $^1Q_1$ state exhibits an reaction time constant of (84 ± 13) fs [134].

Studies of dissociation dynamics after transitions to the higher excited states have so far been scarce. Alekseyev *et al.* [148] and Marggi Poullain *et al.* [142] have shown that the lowest absorption bands (B and C) are predissociated by coupling to other repulsive states, such as the Q states or higher lying repulsive states, stemming from $\sigma \rightarrow \sigma^*$ electron excitation. Utilizing absorption of the VUV pulses or two-photon UV absorption even higher Rydberg states may be populated in this experiment. In Figure 4.23 the Rydberg states inside the bandwidth of the single-photon VUV and two-photon VUV pump pulses are shown. For the 161-nm VUV pulse, D-band excitation of the 6p ($^2E_{3/2}$) in the ν_1 vibrationally excited state state is dominant, while two-photon UV absorption may populate for example the 9d ($^2E_{3/2}$) or 8s ($^2E_{1/2}$) state.

The predissociative nature of other Rydberg states, such as the 6s ($^2E_{1/2}$), 6p ($^2E_{1/2}$) and 7s ($^2E_{3/2}$) has been studied previously both experimentally, as well as theoretically [123, 148]. These studies provide evidence for sub-picosecond dynamics, leading to a decomposition of the molecule. The analysis of reaction dynamics after Rydberg excitations below 170 nm will rely mostly on spectroscopic information [146, 149]. To the best of the authors knowledge, no theoretical studies about the potential energy surfaces relevant to the highly excited molecular states accessed by the 161-nm pump pulse have been published at the time this experimental study has been conducted. The absence of the relevant theoretical data complicates a thorough analysis of the excited wave packet dynamics. However, there are indications, that the 6p ($^2E_{3/2}$) Rydberg state, excited with the 161-nm pump pulse, is pre-dissociated by crossing the 2 $^1A_1$ state [148].

4.4.2 EXPERIMENT

The experimental setup used is the same as in Section 4.3 and depicted in Fig. 4.18. The energy provided by 268-nm and 161-nm radiation was reduced to less than 500 nJ to eliminate contributions to the parent ion signal from multi-photon ionization by each individual pulse. Iodomethane was supplied from the vapor of the pure liquid (Sigma Aldrich, 99 %).

The finite Gaussian instrument response function (IRF) given by the cross correlation of UV and VUV pulses of (26.1 ± 1.7) fs was measured experimentally in the same experimental run. The measurement methodology utilizing molecular oxygen as a medium for single-UV + single-VUV photon cross correlation has been presented in Section 4.3.

The sub-21-fs harmonic pulses grant the required temporal resolution to study dynamics in the sub-10-fs range and follow the processes steering the reaction dynamics directly after the excitation [60, 61]. Furthermore, the utilized excitation scheme does not rely on resonance-enhanced multiphoton ionization (REMPI) to probe the reaction dynamics and can thus be applied readily to a wide range of molecules. The weak-field VUV-probe avoids light-induced effects on the molecular potential energy landscape [103, 150] commonly present when a multi-photon IR probe transition is used. This influence is most pronounced in the vicinity of the delay time origin and within the probe pulse duration, as the molecular system is effectively dressed by the strong IR probe field.

4.4.3 RESULTS & DISCUSSION

This section will first focus on the UV photodissociation via the A absorption band, and the potential energy surfaces (PES) enabling these reaction dynamics, before addressing the VUV-induced dissociation pathway, which is involves highly-excited Rydberg states of the molecule.

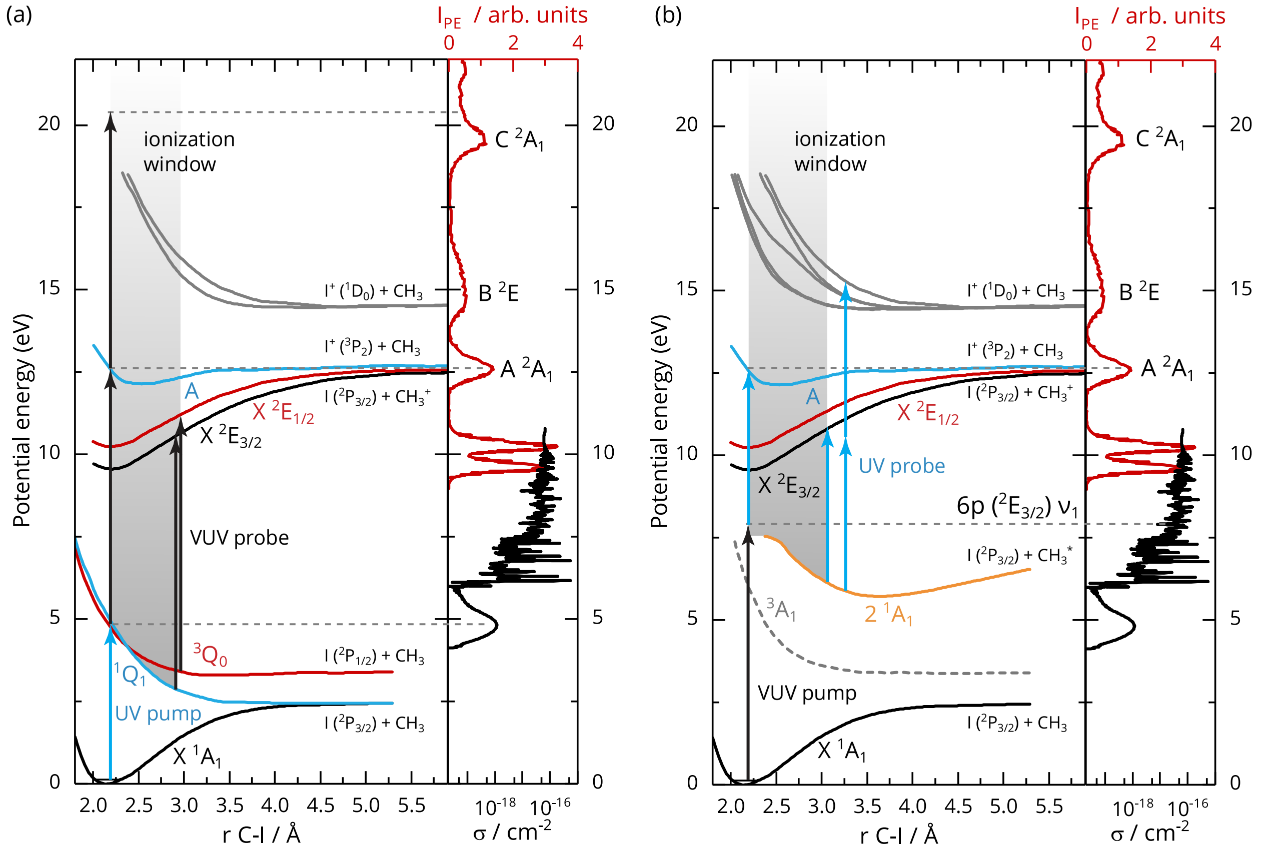

FIGURE 4.24– Excitation schemes and relevant electronic states for the (V)UV photodissociation of CH_3I. (a) A-band dissociation: UV-pump–VUV-probe scheme. (b) D-band dissociation: VUV-pump–UV-probe scheme. Potential energy curves reproduced from Ref. [148] (CH_3I) and Ref. [151, 152] (CH_3I^+). (V)UV absorption cross sections (logarithmic scale, black) from Ref. [146], and photoelectron spectra (red) from Ref. [149].

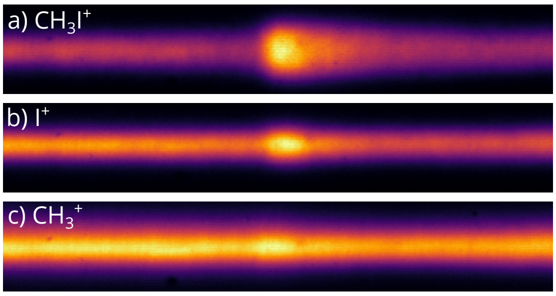

FIGURE 4.25– Averaged ion microscope images for iodomethane (a) and its fragments: atomic iodine (b) and methyl (c). Positive delay: UV pulse early and VUV late. Negative delay: vice versa.

UV-INDUCED DISSOCIATION

Figure 4.24 shows a 1D cut along the H_3C-I bond coordinate, which in this case corresponds to the main reaction coordinate, through the relevant PES for CH_3I [148] and for CH_3I^+ [151, 152]. As lined out previously, at a wavelength of 268 nm the $^3Q_0$ state is excited nearly exclusively [137, 153] and a minor amount of the population is transferred to the $^1Q_1$ state via a non-adiabatic crossing, leading to a rapid cleavage of the H_3C-I bond on both PES [154]. Dissociation in the $^3Q_0$ state results in excited iodine fragments in the $I^*(^2P_{1/2})$, while the $^1Q_1$ state correlates to ground state $I(^2P_{3/2})$ atoms.

In the presented excitation scheme, single VUV probe photon ionization forming stable parent ions is possible in a broad ionization window from both states to the respective spin-orbit split ground states: $^1Q_1 \rightarrow X^1E_{3/2}$ and $^3Q_0 \rightarrow X^1E_{1/2}$. The ionization windows are depicted in Fig. 4.24 a. For bond lengths exceeding this window, the photon energy is not sufficient to ionize the molecule with a single photon. The major $I(^2P_{1/2})$ reaction channel can be followed in this scheme up until the asymptotic region is reached, thus providing a complementary measurement to existing REMPI studies [134, 139] for the reaction time of this channel. Although, the $I(^2P_{3/2})$ channel is only visible up to a H_3C-I bond length of 2.9 Å, corresponding to a lower limit of an ionization window duration of >22 fs, retrieved from a classical trajectory calculation, it is included in the analysis.

The delay-dependent ion yield is retrieved from the spatial ion distribution (Fig. 4.25) acquired with the mass/charge-selective imaging ion spectrometer. The vertical coordinate in the image is averaged and the respective delay between the counter-propagating UV and VUV pulses is mapped along their common propagation axis on the horizontal coordinate. The delay convention used in the discussion of the presented results is the same as in the previous section: Positive delays refer to the UV pulse arriving early and the VUV pulse acting as the probe pulse and vice-versa for negative delay times. In this detection scheme the delay-dependent ion yield for parent and fragment ions is retrieved for all delay times on a single-shot basis and the average over 3000 complete delay data sets is presented in Figure 4.25. To differentiate between the static ion yield created by the individual pulses and the transient yield attributed to the dynamics, background measurements have been performed, where the signal created by each optical branch of the apparatus was measured independently. In the transient ion yields shown in Figure 4.26 these signals have been subtracted.

The delay-dependence of the CH_3I^+ parent ion yield (Fig. 4.26 a) is modeled by the convolution of the IRF with a bi-exponential decay (Eqn. 4.10), with the time constants $\tau(^3Q_0) = (98.2 \pm 1.9)$ fs and $\tau(^1Q_1) = (28.5 \pm 2.8)$ fs, corresponding to the population decay times of the respective states.

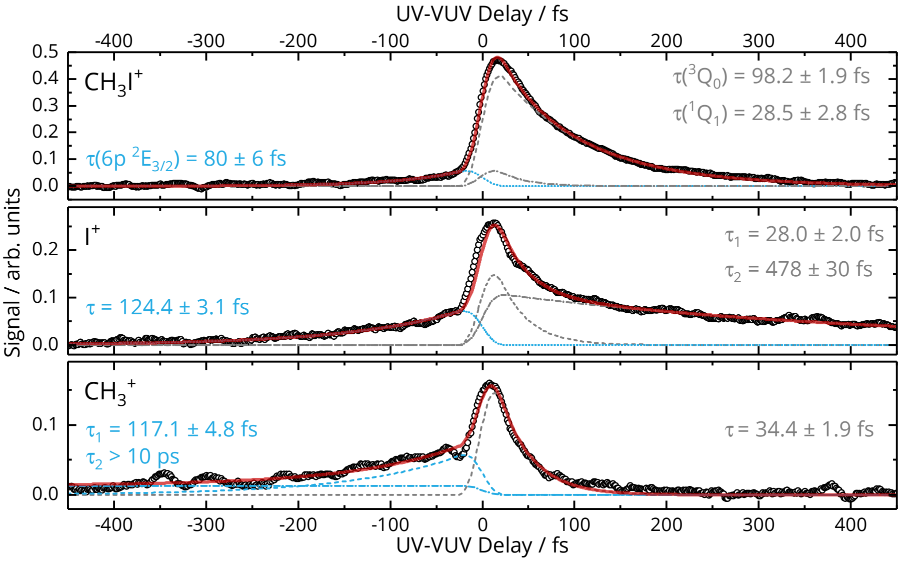

FIGURE 4.26– Pump-probe data sets for the CH_3I^+ parent ion and its photodissociation fragments. (a) CH_3I^+ parent ion yield. (b) I^+ fragment yield. (c) CH_3^+ fragment yield.

The finding for $\tau(^3Q_0)$ is in excellent agreement with previously published time-resolved studies for the $^3Q_0$ channel, which state a reaction time of (94 ± 6) fs [134]. $\tau(^1Q_1)$ is interpreted as the duration of the $^1Q_1 \to X^1E_{3/2}$ ionization window in very good agreement with classical trajectory calculations taking into account the ionization window restrictions in the case of the utilized probe wavelength. For these calculations the $^1Q_1$ state is approximated as a repulsive exponential potential and Newton's classical equations of motion are solved for an initial C-I bond length of 2.2 Å. The $\tau(^3Q_0)$ time constant directly relates to the molecular dissociation time along the $CH_3{-}I$ reaction coordinate followed to the asymptotic PES region.

For the discussion of the delay-dependent I^+ and CH_3^+ fragment yields different mechanisms need to be considered [132]. After preparation of the excited state (CH_3I^*) in the pump step charged fragments are primarily detected as a result of the following processes.

(1) Probe photon ionization of uncharged fragments, created via the initial dissociation in the A band:

$$\begin{tikzcd}
 & \mathrm{CH_3^+} & & \mathrm{I^+} \\
\mathrm{CH_3I^*} \arrow[r] & \mathrm{CH_3} \arrow[u, "\text{probe}"] & + & \mathrm{I} \arrow[u, "\text{probe}"]
\end{tikzcd} \tag{4.11}$$

(2) Absorption of an additional pump photon, transferring population to another excited state ($CH_3I^\dagger$), where subsequent dynamics are taking place. The product fragments of the latter process are then detected by probe photon ionization.

$$\begin{tikzcd}
 & & \mathrm{CH_3^+} & & \mathrm{I^+} \\
\mathrm{CH_3I^*} \arrow[r, "\text{pump}"] & \mathrm{CH_3I^\dagger} \arrow[r] & \mathrm{CH_3} \arrow[u, "\text{probe}"] & + & \mathrm{I} \arrow[u, "\text{probe}"]
\end{tikzcd} \tag{4.12}$$

(3) Dissociative few-photon ionization, where the pump pulse resonantly excites unbound ionic states while the C-I bond is still intact:

$$\begin{tikzcd}
 & \mathrm{CH_3^+} \;+\; \mathrm{I} \\
\mathrm{CH_3I^+} \arrow[ur] \arrow[dr] & \\
 & \mathrm{CH_3} \;+\; \mathrm{I^+} \\
\mathrm{CH_3I^*} \arrow[uu, "\text{probe}"] &
\end{tikzcd} \tag{4.13}$$

The first two processes are accompanied by a shift of the maximum fragment yield towards increased delays, resulting from the molecular dissociation time and have been observed in time-resolved experiments using REMPI detection schemes [130, 139, 155] or non-resonant few-photon IR ionization [132].

Here, the delay-dependent I^+ yield (Fig. 4.26 b) reaches its maximum near the delay-time origin. Thus, the observed delay-dependence is interpreted considering a dissociative ionization scheme (3), dominant for small delay-times, and the excitation of high-lying Rydberg states by two UV-photon absorption in the pump step, which may be ionized at a later point in time, corresponding to signal at increased delay time. Both components are included in a data evaluation model consisting of a fast and slow decay component, with respective decay constants of (28.0 ± 2.0) fs for the dissociative ionization scheme and (478 ± 30) fs for the two UV-photon absorption-induced dynamics.

The dissociative ionization yield depends strongly on the few-photon excitation cross section of the dissociative CH_3I^+ ion state, which evolves in time with the geometrical distortion of the molecular bond along the reaction coordinate. The excitation from either the $^1Q_1$ and $^3Q_0$ states to the molecular ion's excited A state is resonant as long as the wave packet propagates within the Franck-Condon region. The potential energy difference between the Q states and the dissociative ionic states converging to the I^+ $(^1D_0)$ + CH_3 asymptote is increasing for elongated $H_3C{-}I$ bond lengths, as depicted in Fig. 4.24. Thus, the fast population decay component in the signal is attributed to a rapidly decreasing dissociative ionization cross section. The slower component is exceeding the molecular dissociation reaction time by more than 300 fs. This finding suggests the involvement of long-lived excited states, which yield I^+ upon interrogation.

This slowly decaying component is not observed in the delay-dependent CH_3^+ yield (Fig. 4.26 c), which can be fitted by a single exponential decay component with a time constant of (34.4 ± 1.9) fs. The time scale is similar to the fast decay of the I^+ ion yield, where the CH_3^+ A state acts as an intermediate resonance in dissociative ionization. Internal conversion from the A state to the ionic ground state is a well-known dissociation pathway, where dynamics are taking place on a picosecond to nanosecond time scale [151, 156], but do not involve absorption of another probe photon, and thus may proceed en-route to the detector. Since this is a single-photon probe pathway, it is expected to be the dominant contribution and is only accessible near the Franck-Condon region, as described above.

Fast decay components, attributed to the dissociative ionization near the Franck-Condon region, are observed for both fragment ions with time constants less than 35 fs. This shows, that the wave packet created by the UV pulse in the A absorption band of CH_3I, leaves the Franck-Condon region in this time frame. Since the presented scheme relies on a weak few-photon probe to avoid strong fields influencing the intrinsic reaction dynamics near the delay-time origin,sufficient temporal resolution is achieved to investigate these early stage reaction dynamics.

VUV-INDUCED DISSOCIATION

While the UV-induced dissociation dynamics are initiated by direct excitation of the dissociative Q states, reaction dynamics after VUV photon absorption are enabled by the presence of closely spaced Rydberg states [123]. While previous studies [123, 143, 144] have focused on dynamics initiated via two UV photon absorption in these highly excited molecular states, the excitation scheme used in this study is tailored to access the ν_1 vibrationally-excited 6p $(^2E_{3/2})$ Rydberg state by single VUV photon excitation at 161 nm [146].

Depending on the fate of the prepared vibrationally-hot wave packet, different probe schemes are relevant to the interpretation of the experiment, as presented in Fig. 4.24 b. When the coupling between the 6p $(^2E_{3/2})$ state and dissociative states is neglected, a deexcitation is only possible by radiative processes evolving on the ps–ns timescale. Rydberg state population can be transferred to the first excited state of CH_3I^+ by single UV-photon ionization. Such a process is observed as non-decaying contribution to the CH_3^+ signal, within the delay-time detection range of the single-shot technique. When a coupling between the 6p $(^2E_{3/2})$ state and the 2 $^1A_1$ state, as indicated in Fig. 4.24 b, is considered, dissociation dynamics can proceed on the 10–100 femtosecond time scale. These may be interrogated by single UV-photon absorption to form stable molecular ions, in the molecular ionization window. Additionally, dissociative two-photon ionization may result in a delay-dependent CH_3^+ and I^+ fragment yield.

The CH_3I^+ yield shown in Fig. 4.26 a indicates a delay dependence in the negative time-delay range, where the VUV pulse arrives early (left side). The exponential decay component with a time constant of (80 ± 6) fs does not contribute strongly to the overall signal, indicating a lower excitation probability compared to the Q state dissociation. Figure 4.24 b highlights the single UV-photon ionization window for a dissociation in the 2 $^1A_1$ state, which is attributed to the observed delay-dependent parent ion signal. The $^3A_1$ state is indicated for comparison, as it is a known dissociation pathway for the lower Rydberg states [148]. In this case dissociation through this pathway, would lead to a much shorter observation window for the parent compared to the 2 $^1A_1$ state, due to the rapidly increasing ionization energy.

The conclusion, that the 2 $^1A_1$ state is responsible for predissociation of the 6p $(^2E_{3/2})$ Rydberg state, is substantiated by the delay-dependent signals observed for the I^+ and CH_3^+ fragments (Fig. 4.26 a,b). Both yields exhibit exponential decays with a time constant of $\tau(\mathrm{I}^+) = (124.4 \pm 3.1)$ fs and $\tau(\mathrm{CH}_3^+) = (17.1 \pm 4.8)$ fs. The origin of these time constants is ascribed to dissociative ionization initiated by absorption of two probe photons. Relevant ionic states, as well as a window indicated by the blue double arrows, are shown in Fig. 4.24 b. Similar as in the time-resolved study published by Schepp *et al.* [60] of the VUV-induced dissociation dynamics of O_2 this pathway extends the parent species' ionization window, which is in accordance with dissociation through the $2\,^1A_1$ state.

An additional long-lived contribution to the CH_3^+ yield, does not decay in the delay-time window of ±500 fs accessible by the single-shot technique. Similar to the UV-pump VUV-probe scheme, a single-photon ionization from the 6p ($^2E_{3/2}$) Rydberg state to the first excited ion state may create CH_3^+ fragments by internal conversion. The long decay constant of this contribution is an indication, that a fraction of the initial Rydberg state population is either transferred to other not predissociated Rydberg states or to the vibrational ground state of the 6p ($^2E_{3/2}$) state and can be interrogated at longer delays. The molecular dynamics evolving in 80–120 fs is attributed to a partial population transfer from the Rydberg state to the dissociating $2\,^1A_1$ state, where the major part of the population is transferred.

In summary, single-shot UV/VUV pump probe spectroscopy was utilized to reexamine the A band dissociation dynamics of iodomethane with a sub 10-fs temporal resolution and simultaneously study the dynamics of the highly excited 6p ($^2E_{3/2}$) Rydberg state. By avoiding strong multi-photon ionization probe fields, sub-30 fs wave-packet dissociation dynamics within the Franck-Condon region were discerned with the 268-nm pump pulse. Additionally, with a 161-nm pump pulse a partial population transfer from the initially excited Rydberg state was observed, which leads to dissociation via the $2\,^1A_1$ state, while part of the population can be excited in the complete delay time window accessible.

5

OUTLOOK & CONCLUSION

The colliding-pulse single-shot pump-probe technique, implemented by Dimitrios Rompotis throughout his PhD project [28, 57], was extended and applied to study ultrafast reaction dynamics of small atmospherically important molecules under perturbative conditions, as well as ionization of noble gasses under strong field conditions. The single-shot technique is at it's heart a time-and-intensity-resolved ion spectrometry method with few-femtosecond delay time resolution, when it is combined with sub-22-fs 161-nm and 268-nm pulses from a low-order harmonic source. Experiments have been conducted, addressing the essential performance indicators of a femtosecond spectroscopy method: the limits of its temporal resolution and its flexibility in terms of operation conditions, in this case the feasible wavelength range for pump and probe radiation and intensity conditions.

The ultrafast VUV-induced dissociation dynamics of H_2O and its deuterated isotopologues in the first excited state ($\tilde{A}^1B_1$) have been studied utilizing a VUV-pump VUV-probe scheme at 7.7-eV photon energy. The experiments were accompanied by ab initio calculations, which allowed the identification of the relevant probe transition scheme. From two possible transitions, the excitation to the ionic ground state is the relevant probe transition. The expected duration of the 1+1 photon ionization window was predicted by calculating the time-dependent vertical excitation energies for an evolving wave packet in the $\tilde{A}^1B_1$ state by Sophia Bazzi from the group of Oriol Vendrell and Robin Santra. The experimentally deduced time of 6.7 fs the H_2O molecule takes to leave the single-photon ionization window while dissociating, as well the influence of hydrogen substitution (7.5 fs for HDO and 9.4 fs for D_2O), are consistent with the trajectory calculations using the ground-state ionization window. In contrast to multi-photon IR-probe schemes, perturbation of the system could be excluded by using weak fields to interrogate the system, accessing the intrinsic dynamics in the ionization window. Furthermore, these results demonstrate the single-shot pump-probe approach's capability to resolve sub-10-fs dynamics by combining robust in-situ determination of the instrument response function with the increased statistical accuracy achieved in a reduced acquisition time compared to delay stage based approaches.

The capabilities of the ion microscope to perform not only delay-dependent measurements with single-shot acquisition rate, but also intensity-dependent measurement have been evaluated by studying the photoionization of the noble gasses Krypton and Xenon with 268-nm radiation at peak intensities between 1×10^{13} W cm^{-2} and 1×10^{15} W cm^{-2}. For these means, Abel-inversion of the microscope images has been performed to reconstruct the cylindrical symmetry of the Gaussian focus of the superimposed UV beams. Simulations for the position-dependent (and thus intensity- and delay-dependent) ion yield in the paraxial approximation for the focus have been performed considering both multi-photon ionization and strong-field effects, such as the AC stark shift on the ionization potential and intermediate states and tunneling ionization in the ADK theory. The sequential ionization of xenon yielding charge states up to Xe^{5+} has been studied, showing bleaching of lower charge states near the central propagation axis of the beam, which is intensified near the temporal overlap, where both pulse replicas meet in time and space. Due to the strong intensity dependence of the auto correlation signal's FWHM a pulse duration of (20.0 ± 1.5) fs for the 268-nm pulse could only be extracted in the Xe^{+} signal at low intensities.

This problem is overcome in high-intensity measurements in krypton. Here, the AC stark shift on intermediate Rydberg states, which are resonantly excited in a 3-UV+X photoionization scheme, could be utilized. Due to the radius-dependent up-shift of intermediate resonances and the ionization potential, residual infrared radiation was able to ionize the transient Rydberg state population at the edge of the beam, while UV ionization is preferred near the center of the beam. This results in a combination of fourth-order UV auto correlation with three UV photon + single and double IR-photon cross correlation measurements, where a UV pulse duration of (20.6 ± 1.2) fs could be retrieved under strong-field conditions. This measurement was enabled by using the ion microscope's imaging capabilities to its fullest, by retrieving the delay- and intensity-dependent ion yield with each single shot.

Furthermore, the design of the single-shot apparatus allows the experimentalist to choose different spectral components of the harmonic pulse train delivered by the low-order harmonic source, which range from the ultraviolet to the extreme ultraviolett regime. By selecting the 3rd (268 nm) and 5th harmonic (161 nm) respectively in the individual branches of the colliding pulse setup, a two-color pump-probe experiment has been performed with iodomethane. Single-shot UV/VUV pump-probe spectroscopy was utilized to reexamine the A-band dissociation dynamics of iodomethane with a sub 10-fs temporal resolution and simultaneously study the dynamics of the highly excited 6p ($^2E_{3/2}$) Rydberg state. By avoiding strong multi-photon ionization probe fields, sub-30 fs wave-packet dissociation dynamics within the Franck-Condon region were discerned after excitation of the $^3Q_0$ and $^1Q_1$ states with the 268-nm pump pulse. The reaction time constant of the $^3Q_0$ dissociation yielding spin-orbit excited atomic iodine fragments is (98.2 ± 1.9) fs, which is in perfect agreement with complementary measurements utilizing the resonance-enhanced multiphoton ionization technique ((94 ± 6) fs) [134, 139], increasing the statistical accuracy of the measurement significantly. Additionally, with a 161-nm pump pulse a partial population transfer from the initially excited 6p ($^2E_{3/2}$) Rydberg state was observed, which leads to dissociation via the 2 $^1A_1$ state, while part of the population can be excited in the complete delay time window accessible. This highlights the importance of Rydberg states as gateway states facilitating ultrafast reaction dynamics, in this case as fast as 80–120 fs, which have been studied for the first time utilizing a single-photon excitation scheme.

In summary, the colliding-pulse single-shot pump-probe apparatus' abilities where evaluated by studying ultrafast dissociation reactions of small molecules, as well as the ionization of noble gas atoms under different intensity conditions. The improved statistical accuracy and reduced measurement time of the single-shot technique compared to a delay stage measurement have proven indispensable in the elucidation of sub-10-fs dynamics of the water molecule. The optical setup is flexible and enables two-color studies from the visible to the extreme ultraviolet spectral range, and was applied to study valence state and Rydberg state dissociation dynamics of iodomethane in a combined experiment. Finally, the imaging capabilities where used to the fullest in retrieving intensity- and delay-dependent strong-field Kr and Xe ion yields.

For the study of molecular reaction dynamics the ion microscope is boon and bane at the same time: While the benefits could clearly be demonstrated throughout this thesis, ion detection methods can provide only limited information about the potential energy surfaces involved in a photoreaction compared to more advanced techniques, such as velocity map imaging or electron-ion coincidence techniques. In the present scheme, where the ion microscope is vital, these techniques may not be implemented.

To overcome this limitation, a delay-stage-based Mach-Zehnder-type reflective split-and-delay unit was designed by the author and implemented by Dominic Laumer in his Master's thesis. While this sacrifices the single-shot capabilities of the colliding-pulse scheme, the wavelength-flexibility is preserved. The split-and-delay unit is designed to enable experiments combining the 3rd (268 nm) and 5th harmonic as pump pulses with higher harmonic probe radiation. Here, the ion microscope may be replaced readily by other detectors, such as a photoelectron spectrometer or a velocity map imaging detector, where the XUV radiation is used as a pertubative weak-field probe to study photoreaction dynamics.

Another approach for the future is a combination of the colliding-pulse scheme, with a tuneable VUV source. In the time-resolved study of the photodissociation dynamics of H_2O a 6-fs ionization window was limiting the observation time wave packet dynamics. By tuning the probe radiation, the duration of this window can be tuned precisely. By these means, the duration of the ionization window is measured as a function of the probe wavelength, which is directly related to the energy difference between the excited state potential energy surface and the ionic ground state potential energy surface. Consequently, this measurement technique will be able to resolve energy difference between electronic states of the molecule far away from the equilibrium geometry and may prove as a tool to aid theoretical calculation of these states. The full delay-range must be scanned for each probe wavelength, which makes fast acquisition time granted by the single-shot technique vital for these measurements. Since the temporal, spectral and intensity stability of such an experiment are crucial, a delay-stage bases approach is ill-advised, while the colliding-pulse single-shot pump-probe technique is feasible.

By these means, the advantages of the presented single-shot technique, which is able to discern sub-10-fs dynamics with high statistical fidelity, may also be combined with specifically tailored interrogation schemes similar to the REMPI technique. These schemes will enable to select the initially excited state and to precisely adjust the interrogation scheme to the experiment, completely avoiding perturbations of the system under study, potentially imposed by the high intensities present in multi-photon ionization techniques.

A

APPENDIX

A.1 SUPPLEMENTAL INFORMATION: H_2O DISSOCIATION DYNAMICS

A.1.1 STATISTICAL EVALUATION OF PUMP-PROBE DATA

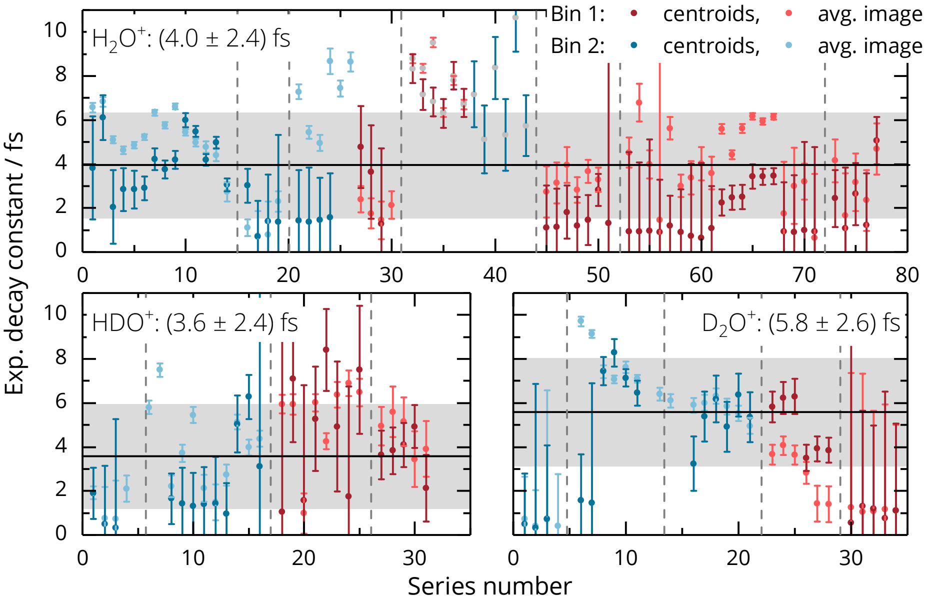

FIGURE A.1– Statistical evaluation of all data sets retrieved for H_2O and its isotopologues. Classified by CCD camera binning (color) and data evaluation method (saturation). Vertical dashed lines indicate individual measurement runs. Gray data points are disregarded. The weighted mean and its rms uncertainty are indicated by the horizontal line and gray box, respectively.

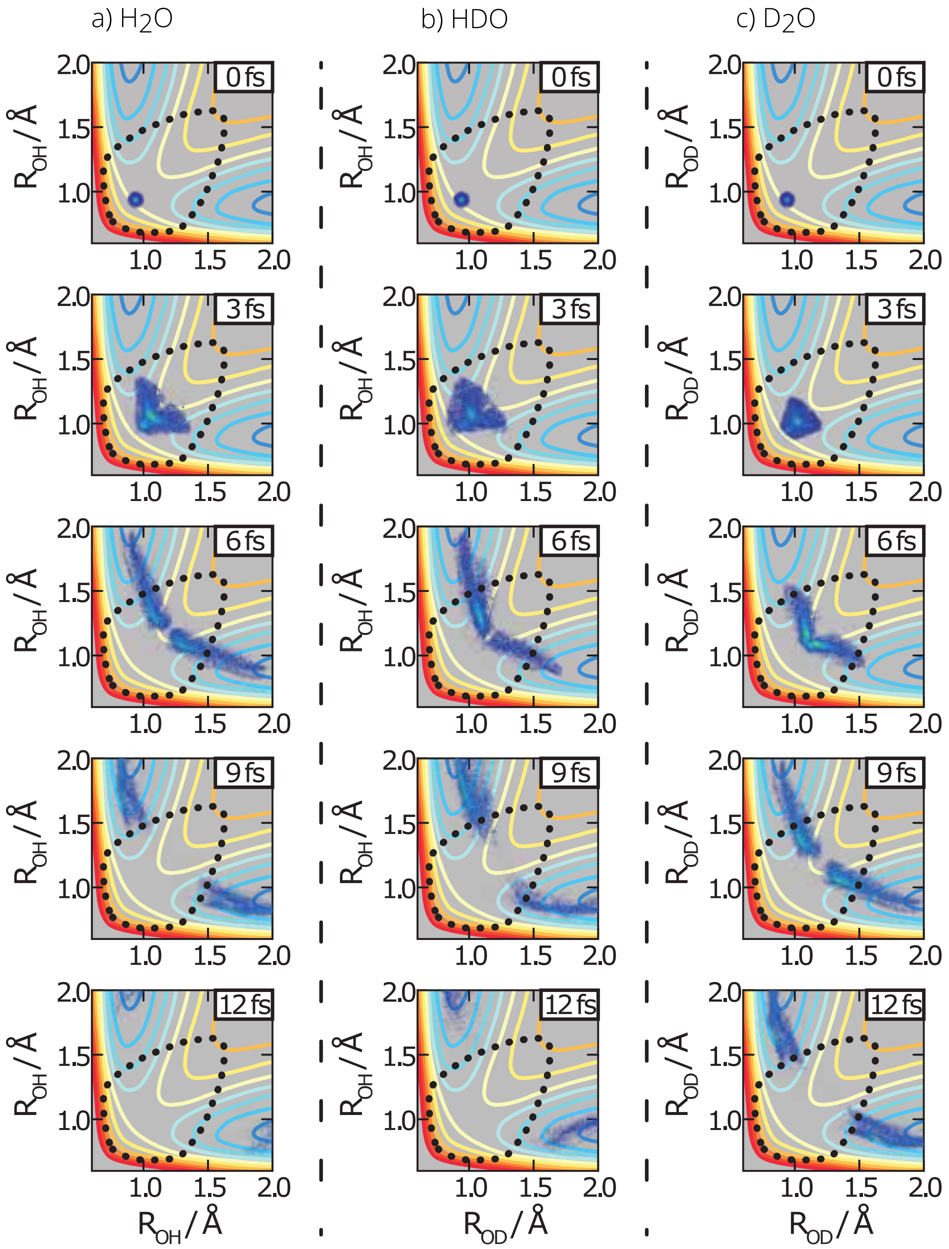

FIGURE A.2– Classical trajectory simulations for H_2O and its deuterated isotopologues performed on the two-dimensional potential by Staemmler & Palma [84].

A.1.2 CLASSICAL TRAJECTORY SIMULATIONS

Classical trajectories on the potential energy surface by Staemmler & Palma [84] have been calculated for the water isotopologues using a Leap-Frog-Algorithm in conjunction with a Monte-Carlo simulation. The HOH angle was fixed to the equilibrium angle and the initial $OH_{(1)}$ and

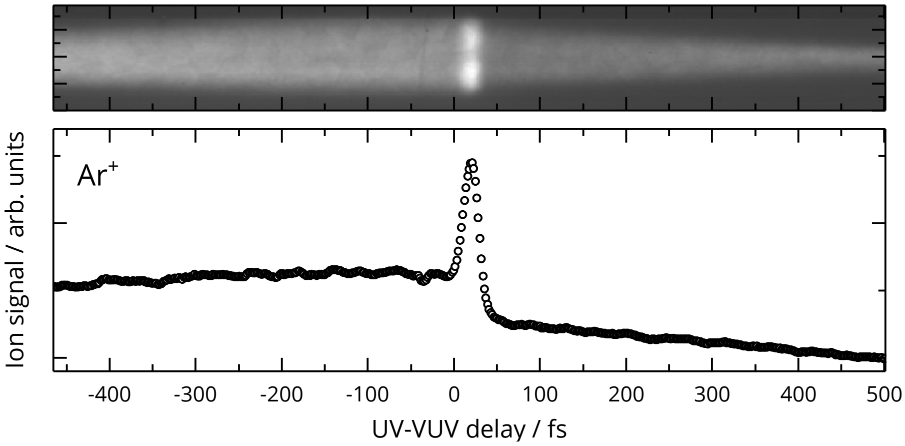

FIGURE A.3– Ion image and delay-dependent ion yield for Ar$^+$ in a UV–VUV pump probe scheme.

$OH_{(2)}$ bond length was drawn from a Gaussian distribution with a standard deviation of ±0.02 Å. The direction of the initial velocity vector along both O-H bond coordiantes was randomized. The total initial velocity was randomized between 0 and the maximal kinetic energy given by the zero-point energy of the H_2O ground state. 10000 trajectories with a time step of 100 as were calculated for each isotopologue. Figure A.2 shows the simulation results in three femtosecond intervals. The ionization window is indicated by the dotted line and durations of 6.8 fs for H_2O, 7.2 fs for HDO and 9.6 fs for D_2O have been extracted in reasonable agreement with the high level calculations performed by Sophia Bazzi.

A.2 UV–VUV PUMP-PROBE MEASUREMENT IN ARGON

The presented argon pump-probe trace has not been further analyzed, because it was unusable to retrieve the cross correlation between the 268-nm and 161-nm pulses. The imbalance between the UV-early and VUV-early part of the transient, indicates the population of long-lived states by the respective pulses. The intensity of neither pulse has been determined, and thus it is impossible to derive an instrument response function, because it is unknown how many photon of each pulse contribute to the signal.

B

BIBLIOGRAPHY

1. Hertel, I. V. & Radloff, W. "Ultrafast Dynamics in Isolated Molecules and Molecular Clusters". *Reports Prog. Phys.* **69**, 1897–2003 (2006).
2. Zewail, A. H. "Femtochemistry. Past, Present, and Future". *Pure Appl. Chem.* **72**, 2219–2231 (2000).
3. Dantus, M., Janssen, M. H. M. & Zewail, A. H. "Femtosecond Probing of Molecular-Dynamics by Mass-Spectrometry in a Molecular-Beam". *Chem. Phys. Lett.* **181**, 281–287 (1991).
4. Zewail, A. H. "Femtosecond Transition-state Dynamics". *Faraday Discuss. Chem. Soc.* **91**, 207–237 (1991).
5. Brito Cruz, C., Fork, R., Knox, W. & Shank, C. "Spectral Hole Burning in Large Molecules Probed with 10 fs Optical Pulses". *Chem. Phys. Lett.* **132**, 341–344 (1986).
6. Wiley, W. C. & McLaren, I. H. "Time-of-Flight Mass Spectrometer with Improved Resolution". *Rev. Sci. Instrum.* **26**, 1150–1157 (1955).
7. Nordling, C., Sokolowski, E. & Siegbahn, K. "Precision Method for Obtaining Absolute Values of Atomic Binding Energies". *Phys. Rev.* **105**, 1676–1677 (1957).
8. Turner, D. W. & Jobory, M. I. A. "Determination of Ionization Potentials by Photoelectron Energy Measurement". *J. Chem. Phys.* **37**, 3007–3008 (1962).
9. Eppink, A. T. J. B. & Parker, D. H. "Velocity Map Imaging of Ions and Electrons Using Electrostatic Lenses: Application in Photoelectron and Photofragment Ion Imaging of Molecular Oxygen". *Rev. Sci. Instrum.* **68**, 3477 (1998).
10. Bernardi, F., Olivucci, M. & Robb, M. A. "Potential Energy Surface Crossings in Organic Photochemistry". *Chem. Soc. Rev.* **25**, 321 (1996).
11. Yarkony, D. R. "Conical Intersections: The New Conventional Wisdom". *J. Phys. Chem. A* **105**, 6277–6293 (2001).
12. Levine, B. G. & Martínez, T. J. "Isomerization through conical intersections." *Annu. Rev. Phys. Chem.* **58**, 613–34 (2007).

13. Polli, D. *et al.* “Conical Intersection Dynamics of the Primary Photoisomerization Event in Vision”. *Nature* **467,** 440–443 (2010).

14. Tango, W. J., Link, J. K. & Zare, R. N. “Spectroscopy of K_2 Using Laser-Induced Fluorescence”. *J. Chem. Phys.* **49,** 4264–4268 (1968).

15. Kinsey, J. L. “Laser-Induced Fluorescence”. *Annu. Rev. Phys. Chem.* **28,** 349–372 (1977).

16. Zare, R. N. “My Life with LIF: A Personal Account of Developing Laser-Induced Fluorescence”. *Annu. Rev. Anal. Chem.* **5,** 1–14 (2012).

17. Ullrich, J. *et al.* “Recoil-ion and Electron Momentum Spectroscopy: Reaction-microscopes”. *Reports Prog. Phys.* **66,** 1463–1545 (2003).

18. Dörner, R. *et al.* “Cold Target Recoil Ion Momentum Spectroscopy: A ’Momentum Microscope’ to View Atomic Collision Dynamics”. *Phys. Rep.* **330,** 95–192 (2000).

19. Garraway, B. M. & Suominen, K.-A. “Adiabatic Passage by Light-Induced Potentials in Molecules”. *Phys. Rev. Lett.* **80,** 932–935 (1998).

20. Sussman, B. J., Townsend, D., Ivanov, M. Y. & Stolow, A. “Dynamic Stark Control of Photochemical Processes”. *Science (80-.).* **314,** 278–281 (2006).

21. Yao, H. & Zheng, Y. “Quantum Control of a Molecular System in an Intense Field Via the Selective Population of Dressed States”. *Phys. Chem. Chem. Phys.* **13,** 8900 (2011).

22. Ferray, M. *et al.* “Multiple-harmonic Conversion of 1064 nm Radiation in Rare Gases”. *J. Phys. B At. Mol. Opt. Phys.* **21,** L31–L35 (1988).

23. Takahashi, E., Nabekawa, Y. & Midorikawa, K. “Generation of 10-μJ Coherent Extreme-ultraviolet Light by Use of High-order Harmonics”. *Opt. Lett.* **27,** 1920 (2002).

24. Takahashi, E., Nabekawa, Y., Nurhuda, M. & Midorikawa, K. “Generation of High-energy High-order Harmonics by Use of a Long Interaction Medium”. *J. Opt. Soc. Am. B* **20,** 158 (2003).

25. Rompotis, D., Gebert, T., Wieland, M., Karimi, F. & Drescher, M. “Efficient Generation of Below-threshold Harmonics for High-fidelity Multi-photon Physics in the VUV Spectral Range”. *Opt. Lett.* **40,** 1675 (2015).

26. Schultze, M., Bergues, B., Schröder, H., Krausz, F. & Kompa, K. L. “Spatially Resolved Measurement of Ionization Yields in the Focus of an Intense Laser Pulse”. *New J. Phys.* **13,** 1–9 (2011).

27. Tzallas, P. *et al.* “Time Gated Ion Microscopy of Light-atom Interactions”. *J. Opt.* **20,** 024018 (2018).

28. Rompotis, D. *et al.* “Single-shot Nonlinear Spectroscopy in the Vacuum-ultraviolet”. *Optica* **4,** 871 (2017).

29. Diels, J.-C. & Rudolph, W. *Ultrashort Laser Pulse Phenomena: Fundamentals, Techniques, and Applications on a Femtosecond Time Scale* Second Edi, 652 (Academic Press, Burlington, 2006).

30. Monmayrant, A., Weber, S. & Chatel, B. “A Newcomer’s Guide to Ultrashort Pulse Shaping and Characterization”. *J. Phys. B At. Mol. Opt. Phys.* **43,** 103001 (2010).

31. Weiner, A. M. *Ultrafast Optics* (John Wiley & Sons, Inc., Hoboken, NJ, USA, 2009).

32. Jaanimagi, P. A. *Breaking the 100-fs barrier with a streak camera.* in *Proc. SPIE 5194, Fourth-Generation X-Ray Sources Ultrafast X-Ray Detect.* (eds Tatchyn, R. O., Chang, Z., Kieffer, J.-C. & Hastings, J. B.) (2004), 171.

33. Feng, J. *et al.* "A Grazing Incidence X-ray Streak Camera for Ultrafast, Single-shot Measurements". *Appl. Phys. Lett.* **96,** 134102 (2010).

34. Trebino, R. *et al.* "Measuring Ultrashort Laser Pulses in the Time-frequency Domain Using Frequency-resolved Optical Gating". *Rev. Sci. Instrum.* **68,** 3277–3295 (1997).

35. Iaconis, C. & Walmsley, I. "Spectral Phase Interferometry for Direct Electric-field Reconstruction of Ultrashort Optical Pulses". *Opt. Lett.* **23,** 792 (1998).

36. Gebert, T. *et al.* "Michelson-type All-reflective Interferometric Autocorrelation in the VUV Regime". en. *New J. Phys.* **16,** 073047 (2014).

37. McPherson, A. *et al.* "Studies of Multiphoton Production of Vacuum-ultraviolet Radiation in the Rare Gases". *J. Opt. Soc. Am. B* **4,** 595 (1987).

38. Hertel, I. V. & Schulz, C.-P. *Atome, Moleküle und optische Physik 1* 1. Edition (Springer-Verlag, Berlin, Heidelberg, 2008).

39. Hertel, I. V. & Schulz, C.-P. *Atome, Moleküle und optische Physik 2* 1. Edition (Springer-Verlag, Berlin, 2010).

40. Haken, H. & Wolg, H. C. *Molekülphysik und Quantenchemie* (Springer-Verlag, Berlin, Heidelberg, 2006).

41. Reinhold, J. *Quantentheorie der Moleküle* (Springer Fachmedien, Wiesbaden, 2015).

42. Wunderlich, C., Kobler, E., Figger, H. & Hänsch, T. W. "Light-Induced Molecular Potentials". *Phys. Rev. Lett.* **78,** 2333–2336 (1997).

43. Shapiro, M. & Brumer, P. *Coherent Control of Atomic, Molecular, and Electronic Processes*, 287–345 (Academic Press, 2000).

44. Gordon, R. J. & Rice, S. A. "Active Control of the Dynamics of Atoms and Molecules". *Annu. Rev. Phys. Chem.* **48,** 601–641 (1997).

45. Keldysh, L. V. "Ionization In The Field of a Strong Electromagnetic Wave". *Sov. Phys. JETP* **20,** 1307–1314 (1965).

46. Ammosov, M. V., Delone, N. B. & Krainov, V. P. "Tunnel Ionization of Complex Atoms and of Atomic Ions in an Alternating Electromagnetic Field". *Sov. Phys. JETP* **64,** 1191–1194 (1986).

47. Tong, X. M. & Lin, C. D. "Empirical Formula for Static Field Ionization Rates of Atoms and Molecules by Lasers in the Barrier-suppression Regime". *J. Phys. B* **38,** 2593–2600 (2005).

48. Spielmann, C. *et al.* "Near-keV Coherent X-ray Generation with Sub-10-fs Lasers". *IEEE J. Sel. Top. Quantum Electron.* **4,** 249–265 (1998).

49. Corkum, P. B. "Plasma Perspective on Strong Field Multiphoton Ionization". *Phys. Rev. Lett.* **71,** 1994–1997 (1993).

50. Lewenstein, M., Balcou, P., Ivanov, M. Y., L'Huillier, A. & Corkum, P. B. "Theory of High-harmonic Generation by Low-frequency Laser Fields". *Phys. Rev. A* **49,** 2117–2132 (1994).

51. Gaumnitz, T. *et al.* "Streaking of 43-attosecond Soft-X-ray Pulses Generated by a Passively CEP-stable Mid-infrared Driver". *Opt. Express* **25,** 27506 (2017).

52. Velotta, R., Hay, N., Mason, M. B., Castillejo, M. & Marangos, J. P. "High-Order Harmonic Generation in Aligned Molecules". *Phys. Rev. Lett.* **87,** 183901 (2001).

53. Lein, M., Hay, N., Velotta, R., Marangos, J. P. & Knight, P. L. "Interference Effects in High-order Harmonic Generation With Molecules". *Phys. Rev. A* **66,** 023805 (2002).

54. Vozzi, C. *et al.* "Controlling Two-Center Interference in Molecular High Harmonic Generation". *Phys. Rev. Lett.* **95,** 153902 (2005).

55. Suárez, N. *et al.* "High-order-armonic Generation in Atomic and Molecular Systems". *Phys. Rev. A* **95,** 033415 (2017).

56. Balcou, P., Salieres, P., L'Huillier, A. & Lewenstein, M. "Generalized Phase-matching Conditions for High Harmonics: The Role of Field-gradient Forces". *Phys. Rev. A* **55,** 3204–3210 (1997).

57. Rompotis, D. *A Single-shot Nonlinear Autocorrelation Approach for Time-Resolved Physics in the Vacuum Ultraviolet Spectral Range.* PhD thesis (Universität Hamburg, 2015).

58. Gebert, T. *Messung ultrakurzer molekularer Zeitkonstanten mit nichtlinearer interferometrischer Autokorrelation bei 160 nm Wellenlänge.* PhD thesis (Universität Hamburg, 2014).

59. Brannath, R. *Zeitliche Verteilung von Auger-Elektronen-Wellenpaketen aus der Photoionisation von Atomen.* PhD Thesis (Universität Hamburg, 2016).

60. Schepp, O. *et al.* "Tracing Few-femtosecond Photodissociation Dynamics on Molecular Oxygen with a Single-color Pump-probe Scheme in the VUV". *Phys. Rev. A* **94,** 033411 (2016).

61. Baumann, A. *et al.* "Weak-field Few-femtosecond VUV Photodissociation Dynamics of Water Isotopologues". *Phys. Rev. A* **96,** 013428 (2017).

62. Hund, F. "Zur Deutung der Molekelspektren. I". *Zeitschrift für Phys.* **40,** 742–764 (1927).

63. Khundkar, L. R. & Zewail, A. H. "Ultrafast Molecular Reaction Dynamics in Real-Time: Progress Over a Decade". *Annu. Rev. Phys. Chem.* **41,** 15–60 (1990).

64. Kanai, T. *et al.* "Generation of Vacuum-ultraviolet Light below 160 nm in a KBBF Crystal by the Fifth harmonic of a Single-mode Ti:sapphire laser". *J. Opt. Soc. Am. B* **21,** 370 (2004).

65. Trabs, P., Noack, F., Aleksandrovsky, A. S., Zaitsev, A. I. & Petrov, V. "Generation of Coherent Radiation in the Vacuum Ultraviolet Using Randomly Quasi-phase-matched Strontium Tetraborate". *Opt. Lett.* **41,** 618 (2016).

66. Kosma, K. *UV-pump IR-probe Spectroscopy of Molecules with Time-Resolution Reaching the 10-fs Range.* PhD thesis (Ludwig-Maximilians-Universität Munich, 2008).

67. Le Blanc, S. P., Qi, Z. & Sauerbrey, R. "Generation of Femtosecond Vacuum-ultraviolet Pulses". *Appl. Phys. B Lasers Opt.* **61,** 439–449 (1995).

68. Ghotbi, M., Beutler, M. & Noack, F. "Generation of 25 μJ Vacuum Ultraviolet Pulses with Sub-50 fs Duration by Noncollinear Four-wave mixing in Argon". *Opt. Lett.* **35,** 3492 (2010).

69. Beutler, M., Ghotbi, M. & Noack, F. "Generation of intense sub-20-fs vacuum ultraviolet pulses compressed by material dispersion". *Opt. Lett.* **36,** 3726 (2011).

70. Adachi, S., Horio, T. & Suzuki, T. "Generation of intense single-order harmonic pulse in the vacuum ultraviolet region using a deep ultraviolet driving laser". *Opt. Lett.* **37,** 2118–2120 (2012).

71. Ghotbi, M., Trabs, P., Beutler, M. & Noack, F. "Generation of Tunable Sub-45 Femtosecond Pulses by Noncollinear Four-wave mixing". *Opt. Lett.* **38,** 486 (2013).

72. Horio, T., Spesyvtsev, R. & Suzuki, T. "Simultaneous Generation of Sub-20 fs Deep and Vacuum Ulraviolet Pulses in a Single Filamentation Cell and Application to Time-resolved Photoelectron Imaging". *Opt Express* **21,** 22423–22428 (2013).

73. Horio, T., Spesyvtsev, R. & Suzuki, T. "Generation of Sub-17 fs Vacuum Ultraviolet Pulses at 133 nm Using Cascaded Four-wave Mixing Through Filamentation in Ne". *Opt. Lett.* **39,** 6021–6024 (2014).

74. Femtolasers Produktions GmbH. *User's Manual for Mirror-dispersion-controlled Ti:Sapphire Oscillator FEMTOSOURCE Rainbow.* 2007.

75. Cheriaux, G. *et al.* "Aberration-free Stretcher Design For Ultrashort-pulse Amplification". *Opt. Lett.* **21,** 414 (1996).

76. Constant, E. *et al.* "Optimizing High Harmonic Generation in Absorbing Gases: Model and Experiment". *Phys. Rev. Lett.* **82,** 1668–1671 (1999).

77. Opto Diode. *AXUV100G Specifications.* 2013. <http://optodiode.com/pdf/AXUV100G.pdf> (visited on 10/10/2017).

78. Kane, D. J. & Trebino, R. "Characterization of Arbitrary Femtosecond Pulses Using Frequency-Resolved Optical Gating". *IEEE J. Quantum Electron.* **29,** 571–579 (1993).

79. Dahl, D. A. "SIMION for the Personal Computer in Reflection". *Int. J. Mass Spectrom.* **200,** 3–25 (2000).

80. Oberheide, J., Wilhelms, P. & Zimmer, M. "New Results on the Absolute Ion Detection Efficiencies of a Microchannel Plate". *Meas. Sci. Technol.* **8,** 351–354 (1997).

81. Moszynski, M., Ludziejewski, T., Wolski, D., Klamra, W. & Norlin, L. O. "Properties of the YAG:Ce Scintillator". *Nucl. Inst. Methods Phys. Res. A* **345,** 461–467 (1994).

82. Photek Ltd. *GM-MCP Gate Module.* 2001. <http://www.photek.com/pdf/datasheets/electronics/GM-MCP.pdf> (visited on 10/10/2017).

83. Mathworks Inc. *Image Processing with MATLAB.* 2014.

84. Staemmler, V. & Palma, A. "CEPA Calculations of Potential Energy Surfaces for Open-shell Systems". *Chem. Phys.* **93,** 63–69 (1985).

85. Engel, V., Schinke, R. & Staemmler, V. "Photodissociation Dynamics of H_2O and D_2O in the First Absorption band: A Complete Ab Initio Treatment". *J. Chem. Phys.* **88,** 129 (1988).

86. Dobbyn, A. J. & Knowles, P. J. "A Comparative Study of Methods For Describing Non-adiabatic Coupling: Diabatic Representation of the $^1\Sigma +^1 \Pi$ HOH and HHO Conical Intersections". *Mol. Phys.* **91,** 1107–1124 (1997).

87. Van Harrevelt, R. & van Hemert, M. C. "Photodissociation of Water. I. Electronic Structure Calculations for the Excited States". *J. Chem. Phys.* **112,** 5777 (2000).

88. Van Harrevelt, R. & van Hemert, M. C. "Photodissociation of Water in the A Band Revisited with New Potential Energy Surfaces". *J. Chem. Phys.* **114,** 9453–9462 (2001).

89. Engel, V. & Schinke, R. "Isotope Effects In The Fragmentation of Water: The Photodissociation of HOD in the First Absorption Band". *J. Chem. Phys.* **88,** 6831 (1988).

90. Henriksen, N. E., Zhang, J. & Imre, D. G. "The First Absorption Band for H_2O: Interpretation of the Absorption Spectrum Using Time Dependent Pictures". *J. Chem. Phys.* **89,** 5607–5613 (1988).

91. Imre, D. G. & Zhang, J. "Dynamics and Selective Bond Breaking in Photodissociation". *Chem. Phys.* **139,** 89–121 (1989).

92. Xu, F., Wang, L., Martens, C. C. & Zheng, Y. "H_2O Photodissociation in the First Absorption Band: Entangled Trajectory Molecular Dynamics Method". *J. Chem. Phys.* **138,** 024103 (2013).

93. Zhou, L., Xie, D., Sun, Z. & Guo, H. "Product Fine-structure Resolved Photodissociation Dynamics: The A band of H_2O". *J. Chem. Phys.* **140,** 024310 (2014).

94. Mota, R. *et al.* "Water VUV Electronic State Spectroscopy by Synchrotron Radiation". *Chem. Phys. Lett.* **416,** 152–159 (2005).

95. Yang, X. F., Hwang, D. W., Lin, J. J. & Ying, X. "Dissociation Dynamics of the Water Molecule on the A $^1B_1$ Electronic Surface". *J. Chem. Phys.* **113,** 10597–10604 (2000).

96. Lu, I.-C., Wang, F., Yuan, K., Cheng, Y. & Yang, X. "Nonstatistical Spin Dynamics in Photodissociation of H_2O at 157 nm". *J. Chem. Phys.* **128,** 066101 (2008).

97. Zhang, J. Z., Abramson, E. H. & Imre, D. G. "C-A Emission in H_2O Following Two-photon Excitation: Dissociation Dynamics in the A State for Different Initial States". *J. Chem. Phys.* **95,** 6536–6543 (1991).

98. Shafer, N., Satyapal, S. & Bersohn, R. "Isotope Effect in the Photodissociation of HDO at 157.5 nm". *J. Chem. Phys.* **90,** 6807 (1989).

99. Vander Wal, R. L. & Crim, F. F. "Controlling the Pathways in Molecular Decomposition: The Vibrationally Mediated Photodissociation of Water". *J. Phys. Chem.* **93,** 5331–5333 (1989).

100. Vander Wal, R. L., Scott, J. L., Crim, F. F., Weide, K. & Schinke, R. "An Experimental and Theoretical Study of the Bond Selected Photodissociation of HOD". *J. Chem. Phys.* **94,** 3548 (1991).

101. Zhang, J., Imre, D. G. & Frederick, J. H. "HOD Spectroscopy and Photodissociation Dynamics: Selectivity in OH/OD Bond Breaking". *J. Phys. Chem.* **93,** 1840–1851 (1989).

102. Engholm Henriksen, N. & Amstrup, B. "Coherent Control of HOD Photodissociation Dynamics in the First Absorption Band". *Chem. Phys. Lett.* **213,** 65–70 (1993).

103. Posthumus, J. H. "The Dynamics of Small Molecules in Intense Laser Fields". *Reports Prog. Phys.* **67,** 623–665 (2004).

104. Wang, H.-T., Felps, W. S. & McGlynn, S. P. "Molecular Rydberg States. VII. Water". *J. Chem. Phys.* **67,** 2614 (1977).

105. Farmanara, P. *et al.* "Ultrafast Internal Conversion and Photodissociation of Molecules Excited by Femtosecond 155 nm Laser Pulses". *J. Chem. Phys.* **111,** 6264 (1999).

106. Wittmann, M. *et al.* "Generation of Femtosecond VUV Pulses and Their Application to Time Resolved Spectroscopy in the Gas Phase". *Opt. Commun.* **173,** 323–331 (2000).

107. Trushin, S. A., Schmid, W. E. & Fuß, W. "A Time Constant of 1.8 fs in the Dissociation of Water Excited at 162 nm". *Chem. Phys. Lett.* **468,** 9–13 (2009).

108. Wigner, E. "On the Quantum Correction For Thermodynamic Equilibrium". *Phys. Rev.* **40,** 749–759 (1932).

109. Swope, W. C., Andersen, H. C., Berens, P. H. & Wilson, K. R. "A Computer Simulation Method for the Calculation of Equilibrium Constants for the Formation of Physical Clusters of Molecules: Application to Small Water Clusters". *J. Chem. Phys.* **76,** 637–649 (1982).

110. Woon, D. E. & Dunning, T. H. "Gaussian Basis Sets for Use in Correlated Molecular Calculations. III. The Atoms Aluminum through Argon". *J. Chem. Phys.* **98,** 1358–1371 (1993).

111. Kendall, R. A., Dunning, T. H. & Harrison, R. J. "Electron Affinities of the First-row Atoms Revisited. Systematic Basis Sets and Wave Functions". *J. Chem. Phys.* **96,** 6796–6806 (1992).

112. Aquilante, F. *et al.* "MOLCAS 7: The Next Generation". *J. Comput. Chem.* **31,** 224–247 (2010).

113. Rabalais, J. W., Debies, T. P., Berkosky, J. L., Huang, J. J. & Ellison, F. O. "Calculated Angular Distributions of Photoelectrons Using the Orthogonalized Plane-wave Approximation". *J. Chem. Phys.* **61,** 529–533 (1974).

114. Peralta Conde, a. *et al.* "Realization of Time-resolved Two-vacuum-ultraviolet-photon Ionization". *Phys. Rev. A - At. Mol. Opt. Phys.* **79,** 1–4 (2009).

115. Kramida, A., Ralchenko, Y. & Reader, J. *NIST Atomic Spectra Database (ver. 5.5.1).* Gaithersburg, MD, 2017. <https://physics.nist.gov/asd>.

116. Abel, N. "Untersuchung der Functionen zweier unabhängig veränderlichen Größen x und y, wie f(x, y), welche die Eigenschaft haben, daß f(z, f (x,y)) eine symmetrische Function von z, x und y ist." *J. für die reine und Angew. Math.* **1826,** 11–15 (1826).

117. Pretzler, G. "A New Method for Numerical Abel-Inversion". *Zeitschrift für Naturforsch. A* **46,** 639–641 (1991).

118. Wessels, P. *et al.* "Suppression of Strong-field Effects in Photoionization of the Single Active Electron of Alkali Atoms". *arXiv Prepr.* arXiv: 1711.01875 (2017).

119. Schechter, I., Schröder, H. & Kompa, K. L. "A Simplified Method for Absolute MPI Cross-section Measurements. Application to Three-photon Non-resonant Ionization of Xe at 266 nm". *Chem. Phys. Lett.* **194,** 128–134 (1992).

120. Gilb, S. *et al.* "Kr (n=5-10, s, d, g) Electronic Wave Packets: Electron Time-of-flight Resolution and the AC-Stark Shift During Wave-packet Preparation". *Phys. Rev. A* **71,** 1–8 (2005).

121. Baumann, A., Rompotis, D., Schepp, O., Wieland, M. & Drescher, M. "Time-Resolved Dissociation Dynamics of Iodomethane Resulting from Rydberg and Valence Excitation". *The Journal of Physical Chemistry A* **122,** 4779 (2018).

122. Mori, T., Glover, W. J., Schuurman, M. S. & Martinez, T. J. "Role of Rydberg States in the Photochemical Dynamics of Ethylene". *J. Phys. Chem. A* **116,** 2808–2818 (2012).

123. Janssen, M., Dantus, M., Guo, H. & Zewail, A. "Femtosecond Reaction Dynamics of Rydberg states. Methyl Iodide". *Chem. Phys. Lett.* **214,** 281–289 (1993).

124. Gustavsson, T., Improta, R. & Markovitsi, D. "DNA/RNA: Building Blocks of Life Under UV Irradiation". *J. Phys. Chem. Lett.* **1,** 2025–2030 (2010).

125. Eland, J., Frey, R., Kuestler, A., Schulte, H. & Brehm, B. "Unimolecular Dissociations and Internal Conversions of Methyl Halide Ions". *Int. J. Mass Spectrom. Ion Phys.* **22,** 155–170 (1976).

126. Khundkar, L. R. & Zewail, A. H. "Picosecond MPI Mass Spectrometry of CH_3I in the Process of Dissociation". *Chem. Phys. Lett.* **142,** 426–432 (1987).

127. Chandler, D. W., W. Thoman Jr., J., Janssen, M. H. M. & Parker, D. H. "Photofragment Imaging: The 266 nm Photodissociation of CH_3I". *Chem. Phys. Lett.* **156,** 151–158 (1989).

128. Eppink, A. & Parker, D. H. "Methyl Iodide A -band Decomposition Study by Photofragment Velocity Imaging". *Chem. Phys.* **109,** 4758 (1998).

129. Eppink, A. T. J. B. & Parker, D. H. "Energy Partitioning Following Photodissociation of Methyl Iodide in the A band: A Velocity Mapping Study". *J. Chem. Phys.* **110,** 832–844 (1999).

130. De Nalda, R. *et al.* "A Detailed Experimental and Theoretical Study of the Femtosecond A-band Photodissociation of CH_3I". *J. Chem. Phys.* **128,** 244309 (2008).

131. Durá, J. *et al.* "Femtosecond Transition-state Imaging of the A-Band CH_3I Photodissociation". *ChemPhysChem* **9,** 1245–1249 (2008).

132. Durá, J., de Nalda, R., Amaral, G. A. & Bañares, L. "Imaging Transient Species in the Femtosecond A-band Photodissociation of CH_3I". *J. Chem. Phys.* **131,** 134311 (2009).

133. García-Vela, A. & Bañares, L. "Wave Packet Study of the Methyl Iodide Photodissociation Dynamics in the 266-333 nm Wavelength Range". *Eur. Phys. J. D* **67,** 1–10 (2013).

134. Corrales, M. E. *et al.* "Structural Dynamics Effects on the Ultrafast Chemical Bond Cleavage of a Photodissociation Reaction". *Phys. Chem. Chem. Phys.* **16,** 8812 (2014).

135. Attar, A. R., Bhattacherjee, A. & Leone, S. R. "Direct Observation of the Transition-State Region in the Photodissociation of CH_3I by Femtosecond Extreme Ultraviolet Transient Absorption Spectroscopy". *J. Phys. Chem. Lett.* **6,** 5072–5077 (2015).

136. Drescher, L. *et al.* "Communication: XUV Transient Absorption Spectroscopy of Iodomethane and Iodobenzene Photodissociation". *J. Chem. Phys.* **145,** 1–6 (2016).

137. Amatatsu, Y., Yabushita, S. & Morokuma, K. "Full Nine-dimensional Ab Initio Potential Energy Surfaces and Trajectory Studies of A-band Photodissociation Dynamics: $CH_3I^* \rightarrow CH_3 + I$, $CH_3 + I^*$, and $CD_3I^* \rightarrow CD_3 + I$, $CD_3 + I^*$". *J. Chem. Phys.* **104,** 9783–9794 (1996).

138. Alekseyev, A. B., Liebermann, H.-P., Buenker, R. J. & Yurchenko, S. N. "An Ab Initio Study of the CH_3I Photodissociation. I. Potential Energy Surfaces". *J. Chem. Phys.* **126,** 234102 (2007).

139. García-Vela, A., De Nalda, R., Durá, J., González-Vázquez, J. & Bañares, L. "A 4D Wave Packet Study of the CH_3I Photodissociation in the A-Band. Comparison with Femtosecond Velocity Map Imaging Experiments". *J. Chem. Phys.* **135,** 154306 (2011).

140. Xu, H. & Pratt, S. T. "A New Look at the Photodissociation of Methyl Iodide at 193 nm". *J. Chem. Phys.* **139,** 214310 (2013).

141. Xu, H. & Pratt, S. T. "Photodissociation of Methyl Iodide via Selected Vibrational Levels of the B ($^2E_{3/2}$) 6s Rydberg State". *J. Phys. Chem. A* **119,** 7548–7558 (2015).

142. Marggi Poullain, S. *et al.* "New Insights into the Photodissociation of Methyl Iodide at 193 nm: Stereodynamics and Product Branching Ratios". *Phys. Chem. Chem. Phys.* **17,** 29958–29968 (2015).

143. Parker, D., Pandolfi, R., Stannard, P. & El-Sayed, M. "Two-photon MPI Spectroscopy of Alkyl Iodides". *Chem. Phys.* **45,** 27–37 (1980).

144. Gedanken, A., Robin, M. B. & Yafet, Y. "The Methyl Iodide Multiphoton Ionization Spectrum with Intermediate Resonance in the A-Band Region". *J. Chem. Phys.* **76,** 4798–4808 (1982).

145. Smythe-Wright, D. *et al.* "Methyl Iodide Production in the Ocean: Implications for Climate Change". *Global Biogeochem. Cycles* **20,** GB3003 (2006).

146. Eden, S., Limão-Vieira, P., Hoffmann, S. & Mason, N. "VUV Spectroscopy of CH_3Cl and CH_3I". *Chem. Phys.* **331,** 232–244 (2007).

147. Mulliken, R. S. & Teller, E. "Interpretation of the Methyl Iodide Absorption Bands Near λ2000". *Phys. Rev.* **61,** 283–296 (1942).

148. Alekseyev, A. B., Liebermann, H.-p. & Buenker, R. J. "Ab Initio Configuration Interaction Study of the B- and C-band Photodissociation of Methyl Iodide". *J. Chem. Phys.* **134,** 044303 (2011).

149. Holland, D., Powis, I., Öhrwall, G., Karlsson, L. & von Niessen, W. "A Study of the Photoionisation Dynamics of Chloromethane and Iodomethane". *Chem. Phys.* **326,** 535–550 (2006).

150. Bucksbaum, P. H., Zavriyev, A., Muller, H. G. & Schumacher, D. W. "Softening of the H2+ Molecular Bond in Intense Laser Fields". *Phys. Rev. Lett.* **64,** 1883–1886 (1990).

151. Bodi, A., Shuman, N. S. & Baer, T. "On the Ionization and Dissociative Photoionization of Iodomethane: A Definitive Experimental Enthalpy of Formation of CH_3I". *Phys. Chem. Chem. Phys.* **11,** 11013–11021 (2009).

152. Marggi Poullain, S., Chicharro, D. V., González-Vázquez, J., Rubio-Lago, L. & Banares, L. "A Velocity Map Imaging Study of the Photodissociation of the Methyl Iodide Cation". *Phys. Chem. Chem. Phys.* **19,** 7886–7896 (2017).

153. Gedanken, A. & Rowe, M. D. “Magnetic Circular Dichroism Spectra of the Methyl Halides. Resolution of the n → σ^* Continuum”. *Chem. Phys. Lett.* **34,** 39–43 (1975).

154. Yabushita, S. & Morokuma, K. “Potential Energy Surfaces for Rotational Excitation of CH_3 Product in Photodissociation of CH_3I”. *Chem. Phys. Lett.* **153,** 517–521 (1988).

155. Corrales, M. E. *et al.* “Femtosecond Time-Resolved Photofragment Rotational Angular Momentum Alignment in Electronic Predissociation Dynamics”. *J. Phys. Chem. Lett.* **7,** 4458–4463 (2016).

156. Walter, K., Weinkauf, R., Boesl, U. & Schlag, E. W. “Molecular Ion Spectroscopy: Mass Selected, Resonant Two-photon Dissociation Spectra of CH_3I^+ and CD_3I^+”. *J. Chem. Phys.* **89,** 1914 (1988).

C

COMMENDATION

Zuerst möchte ich mich bei Prof. Dr. Markus Drescher bedanken, der mir nicht nur die Möglichkeit gegeben hat, in diesem spannenden Bereich meine Dissertation anzufertigen, sondern mir den Freiraum gegeben hat, viele eigene Projekte anzustoßen und zu verwirklichen. Darüber hinaus durfte ich mir in der Dynamix-Gruppe Wissen in vielen Bereich aneignen, vom Aufbau von Instrumentierung, über Softwareentwicklung bis zum Anfertigen von technischen Zeichnungen und zur analogen Elektronik.

Außerdem danke ich JProf. Dr. Ulrike Frühling und Prof. Dr. Robin Santra für die Co-Begutachtung und Co-Betreuung meiner Dissertation.

Dank geht auch an Sophia Bazzi, Daria Gorelova, Oriol Vendrell und abermals Robin Santra für die angenehme Kollaboration bei der Analyse und Veröffentlichung der Ergebnisse zur Wasser-Dissoziationsdynamik. Es ist schön, aus jedem gemeinsamen Treffen neues Wissen und Ideen mitnehmen zu können.

Ich danke allen jetzigen und ehemaligen Mitgliedern der Dynamix-Gruppe. Allen voran Dr. Marek Wieland. Genauso natürlich Dr. Dimitrios Rompotis, der nicht nur den Weg für meine Experimente bereitet hat, sondern auch stets als heimlicher Co-Betreuer mit Rat und Tat zur Seite stand. Vielen Dank an Oliver Schepp, Roman Brannath, Katharina Wenig, Yannic Ristau und Markus Pfau für die wunderbare Zusammenarbeit im Labor und den Spaß, den wir zusammen bei der Arbeit hatten.

Großen Dank an das Team in der mechanischen und elektronischen Werkstatt und Oliver Becker. Ohne den entspannten technischen Support, würden wir vermutlich nicht mal die Hälfte unser Projekte verwirklichen.

Zu guter Letzt, gilt natürlich meiner Familie und meiner Frau Michéle der größte Dank dafür, dass Sie immer für mich da sind, auch wenn ich mich mal wieder Hals über Kopf in zu viele Projekte, Ziele und Dinge gleichzeitig gestürzt habe.

D

DECLARATION ON OATH

EIDESSTATTLICHE VERSICHERUNG

Hiermit versichere ich an Eides statt, die vorliegende Dissertationsschrift selbst verfasst und keine anderen als die angegebenen Hilfsmittel und Quellen benutzt zu haben.

Die eingereichte schriftliche Fassung entspricht der auf dem elektronischen Speichermedium.

Die Dissertation wurde in der vorgelegten oder einer ähnlichen Form nicht schon einmal in einem früheren Promotionsverfahren angenommen oder als ungenügend beurteilt.

Hamburg, den 19.04.2018 Unterschrift der Doktorandin / des Doktoranden